

# The role of trace elements on formation of quenched-in vacancies and precipitation hardening in Al-alloys

Dissertation

Zur Erlangung des Doktorgrades der Naturwissenschaften

*(Dr. rer. nat.)*

Der

Naturwissenschaftlichen Fakultät II  
Chemie, Physik und Mathematik

der Martin-Luther-Universität  
Halle-Wittenberg

Vorgelegt von

Herrn Alaaeldin Mahmoud Hussien Ibrahim  
Geb.am 01.01.1986 in Assuan, Ägypten

---

## **Gutachter:**

Erstgutachter: Prof. Dr. Reinhard Krause-Rehberg

Zweitgutachter: PD Dr. Hartmut S. Leipner

Drittgutachter: Prof. Dr. John Banhart

Tag der öffentlichen Verteidigung: 11. Dezember 2019



## Acknowledgments

First, my utmost thanks go to **Allah** for giving me the strength, patience and great support for conducting this work.

I would like to express my deepest gratitude and sincere thanks to my advisor **Prof. Dr. Reinhard Krause-Rehberg** for his continuous help, his patience, his motivation, and for the provided opportunity to carry on this research project under his supervision.

Besides my advisor, my sincere thanks go to **Dr. Mohamed Elsayed**, for his participating in suggestion the research program of this thesis; he was working hand in hand with me. This work would not have been possible without his endless supply of enthusiasm and knowledge.

I would like to thank also **Dr. Torsten Staab** (Würzburg University) for his fruitful discussion, his wonderful cooperation, and for providing the DSC measurements.

Also, I wish to express my sincere gratitude to **Prof. Dr. Kieback** and **Dr. Muehle**, (TU Dresden) for providing the samples and doing TEM measurements. Special thanks to **Uwe Gutsche**, **Dr. Birgit Vetter** and **Tamara Friedrich** (TU Dresden) for the annealing treatment and the hardness tests.

To all my colleagues in the workgroup of positron annihilation at the Martin Luther University (Halle-Wittenberg); **Dr. Ahmed Elsherif**, **Dr. Marco John**, **M.Sc. Chris Bluhm**, cordial thanks for all the intellectual discussions we had. **M.Sc. Eric Hirschmann** is highly acknowledged for his software of DPALS. The team of mechanical and electronic workshops is deeply appreciated.

**Prof. Dr. Jacob Čížek**, Charles University Prague, Czech Republic is highly acknowledged for his software of digital CDBS.

I would like to take this opportunity to thank my master thesis supervisor **Prof. Dr. Emad Badawi** (Minia University, Egypt), with the help of whom I managed to take my first step in research.

I am indebted for the continuous support from my **mother** and **father** and without them, I could not have accomplished this degree. Special thank goes to my **siblings** for all their help and motivation. I am grateful to my wife **Alaa** and my lovely daughters **Roqaya** and **Ruba** for their patience and great support in many ways during my Ph.D. study.

Deutscher Akademischer Austausch Dienst (DAAD), financial support from the Egyptian Higher Education Ministry, Aswan University and the Physics Institute of Martin-Luther-University for conducting this study in Germany is gratefully acknowledged.

## **Declaration**

I hereby, declare that this thesis is an original report of my research, has been written by myself without any external help. The experimental work is almost entirely my own work; the collaborative contributions, such as sample preparation, have been indicated clearly and acknowledged. References have been provided correctly on all supporting literature and resources.

I declare that this work has not been submitted for any other degree or professional qualification either in Martin-Luther-University, Halle-Wittenberg or in any other University.

---

Place and date

---

Ibrahim, Alaaeldin Mahmoud Hussien



## Publications

- 1- *Positron annihilation lifetime spectroscopy at a superconducting electron accelerator*, A. Wagner, W. Anwand, A. G. Attallah, G. Dornberg, M. Elsayed, D. Enke, **A. E. Hussein**, R. Krause-Rehberg, M.O.Liedke, K.Potzger, and T.T.Trinh, IOP Conf. Series: Journal of Physics: Conf. Series, 79 (2017) 012004.
- 2- *Comparative techniques to investigate plastically deformed 5754 Al-alloy*. Abdel-Rahman, M., Salah, M., **Ibrahim, A. M.**, & Badawi, Modern Physics Letters B, 31(28) E. A. (2017), 1750255.
- 3- *Improving depth resolutions in positron beam spectroscopy by concurrent ion-beam sputtering*. John, M., Dalla, A., **Ibrahim, A. M.**, Anwand, W., Wagner, A., Böttger, R., & Krause-Rehberg, Nuclear Instruments and Methods in Physics Research Section B: Beam Interactions with Materials and Atoms, 423, R. (2018). 62-66.
- 4- *Precipitation Behavior in High - Purity Aluminium Alloys with Trace Elements -The Role of Quenched - in Vacancies*. Lotter, F., Muehle, U., Elsayed, M., **Ibrahim, A. M.**, Schubert, T., Krause - Rehberg, R., ... & Staab, T. E. physica status solidi (a), 215(24) (2018), 1800375.

## Curriculum vitae

**Family name:** Ibrahim  
**Given name:** Alaaeldin Mahmoud Hussien  
**Date of birth:** 01.01.1986  
**Place of birth:** Aswan, Egypt  
**Marital status:** Married  
**1991-1996:** Primary school  
**1996-1999:** Prep. school  
**1999-2002:** High school  
**2002-2006:** Bachelor of Physics, Aswan University, Egypt  
**2008-2013:** Master in Physics, Aswan University, Egypt  
**April 2016-Present:** PhD student, Positron Annihilation laboratory, Martin-Luther University (Halle-Wittenberg)

---

Place and date

---

Ibrahim, Alaaeldin Mahmoud Hussien

## Abstract

The main challenge in modern metallurgy and material physics is the improvement of materials properties that match the applications. The success of means of transportation such as aircraft and automobiles depends on weight reduction by using lighter alloys with higher-strength and smaller cross-sections. Aluminum-based alloys are one of the most important alloys in our modern life. They have been used over a wide area in aerospace, automotive, and construction engineering. Due to the low strength of pure aluminum, most of the commercially used aluminum contains one or more alloying elements. The alloying elements improve remarkably the mechanical properties, since precipitate particles are produced within the metal matrix. Precipitations can obstacle the dislocations motion, which is the main reason of decreasing the materials strength. Typical precipitate hardenable aluminum alloy is Al-Cu. It is used in many industrial applications such as fuselage in aviation and automobile. The main hardening precipitates in binary Al-Cu are Guinier-Preston zones GP-II /  $\theta''$  ( $\text{Al}_3\text{Cu}$ ) and  $\theta'$  ( $\text{Al}_2\text{Cu}$ ). However, microalloying solutes (e.g. In and Sn) in small amounts of 100–500 ppm have a significant effect on the strength in Al-Cu alloys, since they help in the acceleration of the precipitations. Precipitations in aluminum alloys are mainly formed due to the diffusion boosted by vacancies during or immediately after quenching. The vacancies bind trace elements, which in turn have a crucial effect on the precipitation (age) hardening. A complete study is performed to examine the impact of some trace elements on the age-hardening in high purity Al-Cu-based alloys (5N5 aluminum).

Positron techniques with their capabilities were used to explain the precipitations processes in the alloys. They help in understanding the correlation between the microscopic and macroscopic properties. Positron annihilation spectroscopy (PAS) is a unique tool to probe the lattice defects due to the exceptional sensitivity of positrons to vacancy-like defects. Positron can be also trapped into precipitations, which is mainly due to different positron affinities for different chemical elements.

While positron lifetime annihilation spectroscopy (PALS) is very sensitive to vacancies, coincidence Doppler broadening spectroscopy (CDBS) is very useful in identifying the local atomic surrounding of vacancies. From the combination of both techniques, we can understand more about the functional mechanisms of the trace elements. Furthermore, additional information can be obtained by using other techniques such as differential scanning calorimetry (DSC) and transmission electron microscope (TEM). Thereby, the results of positron annihilation may be consummated, and a complete picture may be drawn.

Our presented work involved six chapters; positron annihilation spectroscopy and the interaction of positron with matter will be presented in details in chapter one. Chapter two will give useful information about various types of defects and different mechanisms of their diffusion. Phase transformation and the story of precipitation hardening in Al-Cu based alloys will be discussed in chapter three. The different techniques, which are used in this work, will be explained in chapter four. Our fruitful results are presented in chapter five; the effect of adding (Cu, In, Sn, Sb, Pb, and Bi) to the aluminum matrix will be discussed. Investigation of precipitates in aluminum binary alloys should help in getting insight into the processes, which take place during annealing of more complex Al ternary alloys. Finally, a short summary is given in chapter six.

## List of Abbreviations and symbols

### Abbreviations

Positron annihilation spectroscopy	PAS
Helmholtz-Zentrum Dresden - Rossendorf	HZDR
Picosecond	ps
Kiloelectronvolt	keV
Megaelectronvolt	MeV
Millielectronvolt	meV
Simple Trapping Model	STM
Error function	erf
Guinier–Preston zones	GP
Positron Annihilation Lifetime Spectroscopy	PALS
Doppler broadening spectroscopy	DBS
Angular Correlation Annihilation Radiation	ACAR
Photomultiplier tubes	PMT
Full-Width at Half-Maximum	FWHM
Constant-fraction discriminator	CFD
Single channel analyzer	SCA
Time-to-amplitude converter	TAC
Digital Positron Annihilation Lifetime Spectrometer	DPALS
Analog-to-Digital Converter	ADC
High pure germanium	HPGe
Coincidence Doppler broadening spectroscopy	CDBS
Positron system	POSSY
Room temperature	RT
Vickers Hardness Number	VHN
Electron Spin Resonance	ESR
High-Resolution Transmission Electron Microscopy	HRTEM
Deep Level Transient Spectroscopy	DLTS
Transmission Electron Microscopy	TEM
Atomic percent	at. %
Weight percent	wt. %

Face-centered cubic	Fcc
(charge, parity, time) theorem	CPT
Maximum Entropy for LifeTime analysis	MELT

### **Greek Symbols**

Magnetogyric ratio	$\Upsilon$
Gamma ray	$\gamma$
Bulk annihilation rate	$\lambda$
Positron lifetime	$\tau$
Positron trapping rate	$\kappa$
Positron trapping coefficient / chemical potential	$\mu$
Annihilation fraction	$\eta$
Detrapping rate	$\delta$
Transition rate	$\vartheta$
work function	$\varphi$
Surface dipole potential	$\Delta$
wave functions	$\psi_+$
Shear stress	$\tau_{sh}$

### **Roman symbols**

Positron	$e^+$
Electron	$e^-$
positron diffusion constant	$D_+$
Relaxation time	$t_r$
Boltzmann constant	$k_B$
Effective positron mass	$m^*$
positron diffusion lengths	$L_+$
Positron lifetime intensity	$I$
Positron affinity	$A_+$
Positron potentials	$V_+$
Burger's vector	$\vec{b}$
Diffusion coefficient	$D$
positron diffusion coefficient	$D_+$
Tungsten	W

## Table of Contents

<b>ACKNOWLEDGMENTS</b>	<b>I</b>
<b>DECLARATION</b>	<b>II</b>
<b>PUBLICATIONS</b>	<b>III</b>
<b>CURRICULUM VITAE</b>	<b>IV</b>
<b>ABSTRACT</b>	<b>V</b>
<b>LIST OF ABBREVIATIONS AND SYMBOLS</b>	<b>VII</b>
<b>TABLE OF CONTENTS</b>	<b>IX</b>
<b>LIST OF FIGURES</b>	<b>XIII</b>
<b>CHAPTER 1 : POSITRON ANNIHILATION SPECTROSCOPY .....</b>	<b>1</b>
1.1 INTRODUCTION .....	1
1.2 POSITRON SOURCES .....	3
1.2.1 Pair-production .....	3
1.2.2 Beta decay.....	4
1.3 INTERACTIONS OF POSITRON WITH MATTER .....	6
1.3.1 Backscattering .....	6
1.3.2 Thermalization and diffusion.....	7
1.3.3 Positron trapping in metals .....	10
1.3.3.1 Positron trapping model in metals .....	11
1.3.3.2 Positrons trapping by Shallow positron traps .....	13
1.3.3.3 Positrons trapping by Dislocations .....	15
1.3.3.4 Positrons trapping by vacancy clusters (voids) .....	16
1.3.3.5 Positrons trapping by vacancy-solute complexes.....	17
1.3.3.6 Positrons trapping by precipitates .....	17
1.4 ANNIHILATION OF POSITRONS AND ELECTRONS .....	19
1.4.1 Positron annihilation spectroscopy .....	20
1.4.1.1 Positron annihilation lifetime spectroscopy .....	21
1.4.2 Doppler broadening spectroscopy .....	22
1.4.2.1 Coincidence Doppler-broadening spectroscopy .....	26

---

1.4.3 Variable energy positron annihilation spectroscopy .....	27
1.4.3.1 Positron Implantation.....	28
1.4.4 Positron beam system at Halle (POSSY).....	30
1.5 OTHER DEFECTS ANALYTICAL TECHNIQUES .....	32
<b>CHAPTER 2 : DEFECTS IN CRYSTAL.....</b>	<b>33</b>
2.1 INTRODUCTION.....	33
2.1.1 Point defects.....	33
2.1.2 Linear defects (Dislocations) .....	36
2.1.2.1 Geometry of dislocations .....	38
2.1.2.2 Dislocation motion.....	40
2.1.3 Bulk (volume) defects.....	42
2.1.4 Planar (Interfacial) defects .....	42
2.2 DIFFUSION.....	43
2.2.1 Introduction.....	43
2.2.2 Fick's first law of diffusion.....	43
2.2.3 Fick's second law of diffusion .....	44
2.2.4 Atomic diffusion Mechanisms .....	45
2.2.4.1 Substitutional diffusion mechanism.....	45
2.2.4.2 Interstitial diffusion mechanism.....	46
2.2.4.3 Frank-Turnbull (dissociative) mechanism .....	47
2.2.4.4 Kick-out mechanism .....	47
<b>CHAPTER 3 : PHASE TRANSFORMATION AND PRECIPITATION HARDENING</b> <b>.....</b>	<b>48</b>
3.1 INTRODUCTION.....	48
3.2 PHASE DIAGRAM .....	48
3.2.1 Gibb's phase rule .....	49
3.2.2 Phase present in a system.....	49
3.3 DIFFUSIVE PHASE TRANSFORMATION .....	51
3.3.1 Nucleation.....	52
3.3.1.1 Homogeneous Nucleation .....	52
3.3.1.2 Heterogeneous Nucleation .....	54
3.3.1.3 Nucleation and growth rate .....	56
3.3.2 Spinodal decomposition.....	57



---

3.4 STRENGTHENING OF ALUMINUM .....	59
3.4.1 Precipitation (Age) hardening .....	59
3.4.1.1 History .....	59
3.4.1.2 Mechanism of age hardening.....	60
3.4.1 Mechanisms of obstacle dislocations .....	64
3.4.1.1 Precipitation cutting mechanism .....	64
3.4.1.2 Dislocation bowing mechanism.....	64
3.4.2 Hardness .....	65
3.4.3 Hardness vs Temperature .....	65
<b>CHAPTER 4 : EXPERIMENTAL TECHNIQUES .....</b>	<b>67</b>
4.1 SAMPLES.....	67
4.1.1 Sample Preparation.....	67
4.1.1.1 Solution Heat Treatment (SHT), Quenching, and Annealing .....	68
4.2 INSTRUMENTS AND DATA ANALYSIS .....	71
4.2.1 Digital Positron annihilation lifetime spectroscopy (DPALS).....	71
4.2.2 Digital Coincidence Doppler Broadening Spectrometer .....	73
4.2.3 Heat flux Differential Scanning Calorimetry (DSC).....	74
4.2.4 Electron microscopy .....	76
4.2.4.1 Transmission electron microscope .....	76
4.2.4.2 Scanning electron microscope .....	77
4.2.5 Vickers Hardness .....	78
<b>CHAPTER 5 : RESULTS AND DISCUSSION.....</b>	<b>80</b>
5.1 INTRODUCTION AND SURVEY .....	80
5.2 HARDNESS MEASUREMENT .....	82
5.3 POSITRON MEASUREMENTS.....	83
5.3.1 Al (5N5).....	83
5.3.1.1 Quenched-in vacancies in Al-5N5.....	85
5.3.2 Quenched-in vacancies in highly diluted binary Al- alloys .....	86
5.3.2.1 Al-0.025 at. % Sb, Pb, Bi and Cu at 520-550 °C in ice-water (~ 0 °C) .....	86
5.3.2.2 Quenching the binary alloys at low temperatures (~ -110 °C).....	90
5.3.2.3 Al-0.025 at. % In quenched at 520 °C to ice-water (~ 0 °C).....	93
5.3.2.4 Al-0.025 at. % Sn quenched at 520 °C to ice-water .....	99
5.3.3 Quenched-in vacancies in Al-1.7 at% Cu based alloys .....	102

---

5.3.3.1 Al-1.7 at% Cu binary alloy .....	102
5.3.3.2 Al-1.7 at% Cu ternary alloys.....	107
Al-1.7 at% Cu-0.01 at% Pb, Sb .....	107
Al-1.7 at% Cu-0.01 at% In, Sn .....	109
<b>CHAPTER 6 : SUMMARY .....</b>	<b>113</b>
<b>REFERENCES.....</b>	<b>116</b>

## List of Figures

### Chapter 1

<b>Figure 1.1:</b> First positron tracks observed by Anderson .....	1
<b>Figure 1.2:</b> Schematic illustration of positron and electron before and after the annihilation ....	2
<b>Figure 1.3:</b> Schematic illustration of $e^+ - e^-$ Pair production from high energy electrons .....	3
<b>Figure 1.4:</b> Proton decay via emission of a $W^+$ to a neutron resulting in a positron and a neutrino .....	5
<b>Figure 1.5:</b> Decay transitions for $^{22}\text{Na}$ .....	6
<b>Figure 1.6:</b> Right: Monte Carlo calculations of positron backscattering probability for Si, Ge, and Au at incident energies 1-30 keV. Left: Experimental positron backscattering probabilities as a function of the incident energy for graphite, Si, Ge and Au .....	7
<b>Figure 1.7:</b> Positron wave function at an interstitial space inside a perfect crystal after thermalization and diffusion. ....	9
<b>Figure 1.8:</b> Thermalization, diffusion, and trapping of the positron. The potential is increased for a point defect in the lattice. ....	9
<b>Figure 1.9:</b> Schematic representation of transition trapping (Left) and diffusion trapping (Right).....	10
<b>Figure 1.10:</b> Schematic diagram of single defect trapping model .....	11
<b>Figure 1.11:</b> The average positron lifetime for neutral, negatively charged vacancies ( $V^0$ and $V^-$ ), and shallow traps as a function of the temperature .....	14
<b>Figure 1.12:</b> Schematic diagram of two trapping stages of the negatively charged vacancies .	15
<b>Figure 1.13:</b> Schematic imagine of a dislocation line with a deep trap center. ....	15
<b>Figure 1.14:</b> Numerical data from Nieminen and Laakkonen of trapping coefficient vs the number of vacancies in the cluster in Al .....	16
<b>Figure 1.15:</b> Scheme of positron trapping by vacancy-solute complex .....	17
<b>Figure 1.16:</b> Positron potentials $V_+(x)$ and wave functions $\psi_+$ of different types of precipitates, (A) GP zones (Fully coherent precipitates $\Delta E_{x,\text{Al}}^+ < 0$ ), (B) GP zones (Fully coherent precipitates $\Delta E_{x,\text{Al}}^+ > 0$ ), (C) GP zones (Fully coherent precipitate containing a vacancy), (d) semi-coherent precipitates, (E) Incoherent precipitates, (F) Incoherent precipitates containing a vacancy .....	19
<b>Figure 1.17:</b> Positron annihilation experimental techniques .....	21

<b>Figure 1.18:</b> Momentum conservation during the $2\gamma$ -annihilation process, $P$ is the momentum of the electron-positron pair .....	24
<b>Figure 1.19:</b> Doppler broadening spectra of two samples: defect-free Si and Si with defects. Both spectra are normalized to the same area .....	25
<b>Figure 1.20:</b> Two Doppler broadening spectra normalized to the same area. One of them (black) is measured with a single Ge detector and the other (red) is measured by CDBS .....	27
<b>Figure 1.21:</b> Makhovian positron implantation profile in Aluminum. Equation 1.48 was used to calculate the profiles, with $A = 4 \mu\text{gcm}^{-2}\text{keV}^{-1}$ , $m = 2$ , and $r = 1.6$ .....	29
<b>Figure 1.22:</b> The positron emission of a $^{22}\text{Na}$ source with and without moderator .....	30
<b>Figure 1.23:</b> Schematic illustration of the positron moderation process by a (110) tungsten foil .....	30
<b>Figure 1.24:</b> Schematic diagram of the slow-positron-beam system at Martin Luther University Halle– Wittenberg (POSSY) .....	31
<b>Figure 1.25:</b> Comparison of positron annihilation spectroscopy to other techniques .....	32
<b><u>Chapter 2</u></b>	
<b>Figure 2.1:</b> Schematic two-dimensional lattice with vacancy, interstitial and substitutional defects.....	33
<b>Figure 2.2:</b> Schematic illustration of Schottky and Frenkel defects.....	36
<b>Figure 2.3:</b> Slip of crystal planes, $b$ the spacing between atoms in the direction of the shear stress, $a$ the spacing of the rows of atoms and $x$ is the displacement .....	37
<b>Figure 2.4:</b> Shear stress versus displacement curve .....	37
<b>Figure 2.5:</b> Schematic description of the edge dislocation (the atomic bonding is not drawn here).....	39
<b>Figure 2.6:</b> Schematic description of the left-handed screw dislocation.....	39
<b>Figure 2.7:</b> Dislocation movement during plastic deformation.....	40
<b>Figure 2.8:</b> Dislocation loop .....	41
<b>Figure 2.9:</b> Schematic illustration of a prismatic dislocation loop.....	41
<b>Figure 2.10:</b> Vacancy loop acts as a prismatic dislocation.....	42
<b>Figure 2.11:</b> Schematic presentation of the grain boundaries .....	42
<b>Figure 2.12:</b> Schematic presentation of twin boundaries and stacking fault.....	43
<b>Figure 2.13:</b> Schematic illustration of Fick's first law. The concentration $C_1 > C_2$ so mass flux will move from high to low concentration .....	44
<b>Figure 2.14:</b> Change of the concentration gradient with time .....	45
<b>Figure 2.15:</b> Single vacancy mechanism of diffusion .....	45

<b>Figure 2.16:</b> Schematic illustration of potential energy of an atom jumps into a vacancy .....	46
<b>Figure 2.17:</b> Divacancy mechanism of diffusion .....	46
<b>Figure 2.18:</b> Interstitial diffusion mechanism .....	46
<b>Figure 2.19:</b> Frank-Turnbull mechanism .....	47
<b>Figure 2.20:</b> Kick-out mechanism.....	47
<b><u>Chapter 3</u></b>	
<b>Figure 3.1:</b> Cu-Ni binary phase diagram, L for liquid, S for solid and $\alpha$ is the substitutional solid solution.....	48
<b>Figure 3.2:</b> Phase present in a system .....	50
<b>Figure 3.3:</b> Composition of phase present in a system .....	50
<b>Figure 3.4:</b> Relative amounts of phases present in a system.....	51
<b>Figure 3.5:</b> Driving force of phase transformation .....	51
<b>Figure 3.6:</b> Schematic illustration of nucleation, growth, and spinodal decomposition.....	52
<b>Figure 3.7:</b> Schematic description of .....	52
<b>Figure 3.8:</b> solid/liquid interface.....	52
<b>Figure 3.9:</b> Total free energy vs nucleus radius .....	53
<b>Figure 3.10:</b> The wetting angle $\theta$ .....	54
<b>Figure 3.11:</b> Schematic of heterogeneous nucleation mechanism; spherical cap of solid phase in liquid on a substrate .....	54
<b>Figure 3.12:</b> Total free energy for homogenous and heterogeneous nucleation.....	55
<b>Figure 3.13:</b> Strain energy as a function of precipitate shape .....	56
<b>Figure 3.14:</b> The overall transformation rate .....	56
<b>Figure 3.15:</b> Temperature dependence of the transformation rates .....	57
<b>Figure 3.16:</b> Nucleation (left) vs spinodal decomposition (right).....	58
<b>Figure 3.17:</b> Heat treatment and hardness of Al-4wt%Cu alloys according to Wilm .....	60
<b>Figure 3.18:</b> Al-Cu alloy Phase diagram (up); $\alpha$ is a cubic closed pack substitutional solid solution of Cu in Al, $\theta$ is an intermetallic compound $Al_2Cu$ (down) .....	61
<b>Figure 3.19:</b> Schematic illustration of GP zones in Al-4wt%Cu alloy .....	62
<b>Figure 3.20:</b> Schematic diagram of $\theta''$ precipitates in Al-4wt%Cu alloy.....	62
<b>Figure 3.21:</b> Schematic description of $\theta'$ precipitates in Al-4wt%Cu alloy.....	63
<b>Figure 3.22:</b> Schematic description of $\theta$ precipitates in Al-4wt%Cu alloy.....	64
<b>Figure 3.23:</b> schematic illustration of heat treatment and hardness mechanism of Al-4wt%Cu alloys.....	64
<b>Figure 3.24:</b> Schematic illustration of precipitate cutting by a dislocation .....	64

<b>Figure 3.25:</b> Schematic representation of dislocation bowing around precipitates (Orowan mechanism) .....	65
<b>Figure 3.26:</b> Hardness vs Temperature. Right: TTT diagram for the precipitation reaction $\alpha \rightarrow \alpha + Gp\ zones \rightarrow \alpha + \theta'' \rightarrow \alpha + \theta' \rightarrow \alpha + \theta$ .....	66
<b><u>Chapter 4</u></b>	
<b>Figure 4.1:</b> Schematic illustration of alloys preparation. ....	67
<b>Figure 4.2:</b> The concentration of equilibrium vacancies per cubic centimeter in pure Al. ....	68
<b>Figure 4.3:</b> Schematic diagram of the quenching setup. ....	70
<b>Figure 4.4:</b> Schematic diagram of digital Positron lifetime spectrometer. ....	71
<b>Figure 4.5:</b> Digital timing process with constant fraction .....	72
<b>Figure 4.6:</b> Schematic illustration of coincidence Doppler broadening Spectrometer .....	74
<b>Figure 4.7:</b> Schematic diagram of the heat flux DSC.....	75
<b>Figure 4.8:</b> Schematic description of the interaction of electrons with matter processes. ....	76
<b>Figure 4.9:</b> Schematic diagram of Different mode of imaging of TEM .....	77
<b>Figure 4. 10:</b> Schematic diagram of SEM. ....	78
<b>Figure 4.11:</b> Schematic diagram of Vickers hardness test indentation .....	79
<b><u>Chapter 5</u></b>	
<b>Figure 5.1:</b> Positron affinities for some elements in the periodic table according to Puska and Nieminen .....	81
<b>Figure 5.2:</b> Hardness curves as a function of natural ageing (bottom) and artificial ageing at 150 and 200 °C (top) for Al-1.7 at.% Cu binary alloy and the ternary alloys with 100 ppm trace elements (In, Sn and Pb).....	82
<b>Figure 5.3:</b> Calculated positron lifetime in FCC Al with and without vacancies .....	84
<b>Figure 5.4:</b> Thermal vacancies generation in Al (5N5) (inset the vacancy formation energy calculated from positron lifetimes).....	85
<b>Figure 5.5:</b> The measured positron lifetimes of pure aluminum (5N5) as a function of the annealing temperature. ....	86
<b>Figure 5.6:</b> Average positron lifetime for aluminum binary alloys with comparison to pure aluminum. The alloys were quenched from 520 or 550 °C to ice water. ....	87
<b>Figure 5.7:</b> Positron lifetimes vs isochronal annealing temperatures of Al-0.025 at.% Cu, Al-0.025 at.% Bi, Al-0.025 at.% Pb and Al-0.025 at.% Sb alloys quenched from 520 °C to ice water. ....	88
<b>Figure 5.8:</b> Positron lifetimes in Al-0.025 at.% Bi and Al-0.025 at.% Sb alloys as a function of isochronal annealing temperatures. The alloys were quenched from 620 °C to ice water.....	89

<b>Figure 5.9:</b> Positron lifetimes vs the isochronal annealing temperatures of the aluminum reference sample and Al-0.025 at.% Cu quenched from 620 °C to -110 °C, measuring temperature is 180K.....	90
<b>Figure 5.10:</b> Positron lifetimes in Al-0.025 at.% Sb, Pb and Bi alloys quenched from 620 °C to -110 °C. The positron lifetimes were measured as a function of isochronal annealing up to 200 °C. The schematic diagram illustrates the binding between solute atoms with vacancies. ....	92
<b>Figure 5.11:</b> Positron lifetimes vs isochronal annealing for Al-0.025at.%In binary alloy quenched at 520 °C to ice water .....	93
<b>Figure 5.12:</b> Schematic description of the solute-vacancy binding at solutionizing temperature, after quenching, and at artificial ageing. Blue: Al atoms; black:solute atoms; Dashed empty circles: vacancies .....	94
<b>Figure 5.13:</b> STEM and EDX-analysis of Al-0.025at%In alloy quenched at 520 °C to ice water and then aged at 150°C for 1 h .....	95
<b>Figure 5.14:</b> Coincidence Doppler broadening spectra of Al-0.025 at.% In. The signature of pure Indium is clear. ....	96
<b>Figure 5.15:</b> Positron lifetimes as a function of annealing temperatures for Al-0.025at.% In quenched from different temperatures. The quenched alloy is compared to the deformed one.	96
<b>Figure 5.16:</b> Vacancy concentration as a function of quenching temperature in Al-0.025 at.% In .....	97
<b>Figure 5.17:</b> Positron trapping rate as a function of annealing temperatures for Al-0.025at.% In quenched from different temperatures. ....	98
<b>Figure 5.18:</b> Comparison between measured and calculated positron reduced bulk lifetime (using simple trapping model) for different quenching temperatures. ....	99
<b>Figure 5.19:</b> Behavior of positron lifetimes as a function of isochronal annealing for in Al-0.025at.%Sn binary alloy quenched at 520 to ice water. ....	100
<b>Figure 5.20:</b> Coincidence Doppler broadening spectra of Al-0.025 at.% Sn in comparison to pure Al and pure Sn. The imprint of pure Sn in the alloy is clear. ....	102
<b>Figure 5.21:</b> (left) PALS measurement of quenched Al-1.7 at.% Cu at 520 °C to ice water. Sample has been isochronally annealed to 500 °C. (Right) PALS measurement of quenched Al-1.7 at.% Cu at 520 °C to ice water. Sample has been isothermally annealed at 50 and 75 °C.	103
<b>Figure 5.22:</b> Calculated positron lifetimes and Doppler spectra of some atomic configurations representing early stages of GP zones with/without vacancies in Al lattice .....	104
<b>Figure 5.23:</b> Doppler spectra of some atomic configurations representing $\theta'$ and $\theta$ with/without vacancies in Al lattice .....	105

---

<b>Figure 5.24:</b> Coincidence Doppler broadening of Al-1.7 at.% Cu in comparison to pure Al.	106
<b>Figure 5.25:</b> Left: High resolution TEM image of Al- 1.7 at% Cu naturally aged (> 1000 h at room temperature). Right: STEM image of aged alloy at 150 °C for 48 h.	107
<b>Figure 5.26:</b> Positron annihilation lifetime measurement of quenched Al-1.7 at.% Cu with 100 ppm Pb and Sb as a function of isochronal annealing up to 350 °C temperature.	108
<b>Figure 5.27:</b> DSC curves for as quenched Al-1.7 at.% Cu alloy with 100 ppm Sn, In, Pb measured directly after quenching to ice water from 520°C.	108
<b>Figure 5.28:</b> DSC curves for the aged Al-1.7 at.% Cu alloy without and with 100 ppm Pb. The two alloys have been quenched to ice water from 520°C.	109
<b>Figure 5.29:</b> Positron lifetimes of as quenched Al-1.7 at.% Cu with 100 ppm Sn and In as a function of isochronal annealing temperature up to 327 °C. The quenching temperature is 520 °C.	110
<b>Figure 5.30:</b> DSC curves for naturally aged Al-1.7at.%Cu-0.01at.%Sn (left) and Al-1.7at.%Cu-0.01at.%In (right).	110
<b>Figure 5.31:</b> DSC curves for aged Al-1.7at.%Cu-0.01at.%Sn (left) and Al-1.7at.%Cu-0.01at.%In (right) at 150°C. After 1 h, GP-I and GP-II zone dissolution are observed between 200 and 270°C. The formation of $\theta'$ precipitates is shifted to be at about 270°C , which is 100 degree more than in case of Al-Cu binary alloy.	111
<b>Figure 5. 32:</b> DSC curves for aged Al-1.7at.%Cu with 100 ppm Sn and In at 200°C. $\theta'$ phase is directly forming as the dominating phase.	112



## Chapter 1 : Positron Annihilation Spectroscopy

### 1.1 Introduction

Positron is the antiparticle of electron with the same mass and spin, but opposite charge [1]. The existence of the positron was firstly proposed in 1928 by *P.A.M. Dirac* [2, 3]. The Dirac wave equation for the permissible energy states of the electron provides quasi-excess negative energy states that had not been spotted. Equation (1.1) is the classical Dirac equation of a particle with rest mass  $m_0$ ;

$$E^2 = p^2c^2 + m_0c^4, \quad \text{with } E = \pm c\sqrt{p^2 + m_0c^2} \quad (1.1)$$

In 1931 *Dirac* assumed that the negative energy (negative energy states), which differ from the normal positive energy of the electron could be related to a new kind of particle with a positive charge [4]. The predicted particle was not proton since its mass was so small compared with that of the proton [4]. Soon after, this particle was discovered by *Anderson* in 1932 [5]; he observed a curvature tracks in a cloud chamber (identical to that for a particle with the mass-to-charge ratio of an electron but in the opposite direction) resulting from the passage of cosmic rays when subjected to a magnetic field [6] (see figure 1.1).

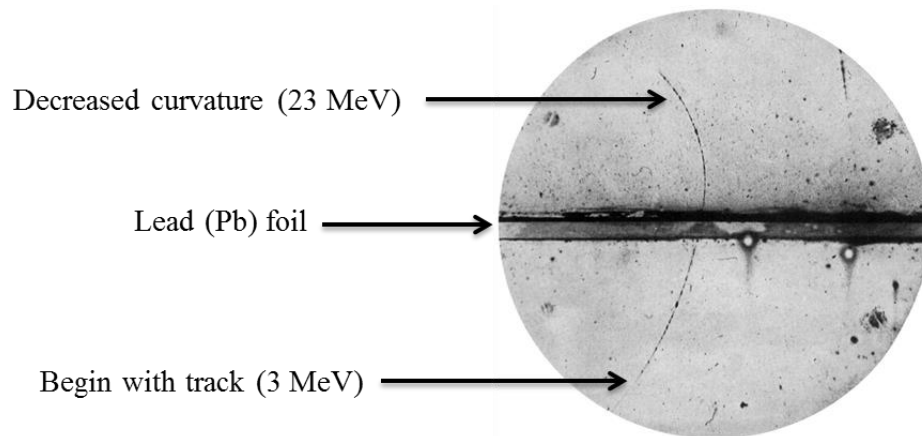


Figure 1.1: First positron tracks observed by Anderson [5].

The ratio of the magnetogyric (the ratio of magnetic moment to angular momentum,  $\gamma$ ) of the electron to that of the positron ( $\gamma(e^-)/\gamma(e^+)$ ) has been determined not to differ from unity by more than  $2 \times 10^{-12}$ , confirming the positron as a spin 1/2 particle [7]. Gyro-frequency [8] measurements (the frequency of a charged particle moving perpendicular to the direction of a uniform magnetic field  $B$ ) showed that the charge-to-mass ratio of this particle does not differ by more than  $4 \times 10^{-8} e$  [9]. Considerations of vacuum polarization in quantum field theory

led to a difference in charge magnitude of no more than  $1 \times 10^{-18} e$  [10]. In vacuum, the positron is a stable particle, like the electron [1]; it has been trapped in the laboratory for periods of the order of three months [7]. The empirical limit on the steadiness of the electron is higher than 1023 years [1]. By pointing out the CPT (charge, parity, time) theorem, we require that the physical laws governing the behavior of positrons are invariant under the combined action of charge conjugation (C), parity (P), and time reversal (T) [11]. This leads to a conclusion that the intrinsic lifetime, mass, charge magnitude, and gyromagnetic ratio of the positron must be similar to the electron [1]. Positron goes beyond being a hypothetical particle that was interpreted through quantum mechanics, but it is established as probe for studying the imperfections in materials, as the crystalline structure of a sample is almost never perfect. For example, in alloys, atomic defects strongly affect the precipitations and hence the hardness. Studying these point defects is essential in the development of materials strengthening. In defect physics, positron annihilation spectroscopy (PAS) is a method for the direct identification of vacancy defects [12]. Positron spectroscopy is a non-destructive technique, which is highly sensitive to vacancies and can provide information on defect depth profiles. It does have limitations in that it is only sensitive to negative and neutral vacancies [13]. It is based on monitoring the 511 keV annihilation radiation emitted when thermalized positrons annihilate in solids with electrons (figure 1.2).

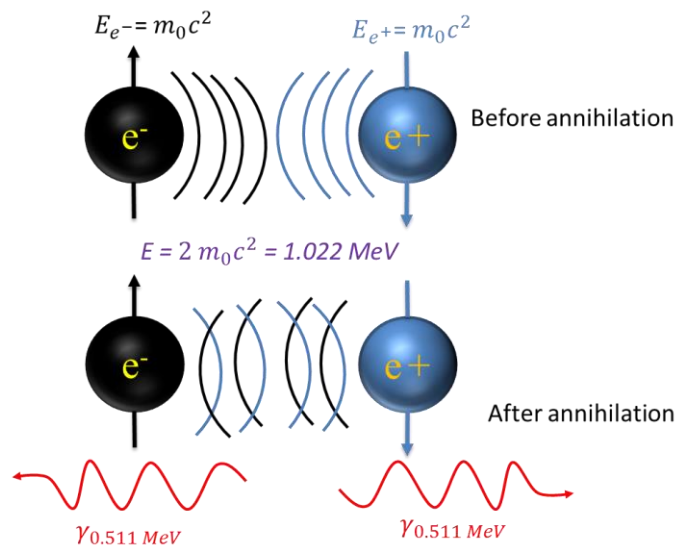


Figure 1.2: Schematic illustration of positron and electron before and after the annihilation [14].

Positrons get trapped at negative and neutral vacancies [15] due to the missing positive charge of the ion cores. At the vacant site, positron lifetime increases and positron-electron momentum distribution gets narrower owing to reduced electron density. The spectroscopy gives information on vacancies at concentrations about  $10^{15} - 10^{19} \text{ cm}^{-3}$ . Positron lifetime is a direct measure of the size of the open volume of a defect. The Doppler broadening of the 511 keV gives the momentum distribution of annihilating electrons. The core electron momentum distribution can be used to characterize impurities or elements nearby a vacancy. The positron lifetime and Doppler broadening are easily applied to bulk materials. Thin films can also be studied by Doppler broadening spectroscopy using a variable energy positron beam. Due to the limitation of conventional positron lifetime spectroscopy, which is essential for obtaining the open volume of a defect, few pulsed positron beam facilities can be used for such thin layers such in Munich and HZDR [16, 17].

## 1.2 Positron Sources

Radioactive decay and pair-production are two different mechanisms to generate positrons.

### 1.2.1 Pair-production

Gamma rays of sufficient energy equivalent to the rest mass of the resultant particles ( $\geq 1.022 \text{ MeV}$  in case of  $e^+$ ,  $e^-$  pair) interact with a nucleus of an atom and create positron-electron pairs. For example, when high energy electrons from a linear accelerator are hitting tungsten (W) or plutonium (Pu) target, gamma rays will be produced by bremsstrahlung. Some gamma rays with energy larger than  $1.022 \text{ MeV}$  can turn into a positron and an electron deep inside the sample. This reaction happens normally near a nucleus with a high atomic number (see figure 1.3).

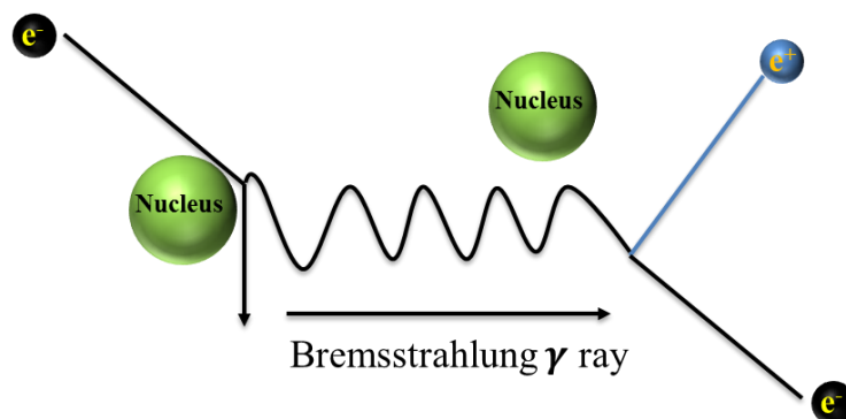


Figure 1.3: Schematic illustration of  $e^+$ -  $e^-$  Pair production from high energy electrons [18].

Nuclides with a proton excess provide an alternative source of positrons; an excess proton will decay into a neutron by the emission of a positron and a neutrino. For laboratory-based work the nuclear-decay process is more familiar, however, Nuclear-decay sources are weak when compared to pair production at synchrotron facilities. Table 1.1 lists some of the longer-lived positron-emitting radionuclides. For the positron annihilation lifetime experiment the positron source should have a high yield, a suitably long half-life sources to be used multiple times and positron emission should be accompanied by the near-simultaneous emission of a gamma photon, which provides a convenient timing signal announcing the ‘birth’ of the positron [15].  $^{22}\text{Na}$  source is most popular isotope used as positron source.

Tab 1.1: Some of the longer-lived Positron emitters [19-22]

Isotope	Half-life	$E_{\text{max}}$ [MeV]	Branching ratio ( $\beta^+$ )
$^{22}\text{Na}_{11} \rightarrow \text{Ne}_{10} + e^+ + \nu$	2.6 y	0.545	0.90
$^{65}\text{Zn}_{30} \rightarrow \text{Cu}_{29} + e^+ + \nu$	243.8 d	0.325	0.98
$^{58}\text{Co}_{27} \rightarrow \text{Fe}_{26} + e^+ + \nu$	70.88 d	0.470	0.15
$^{48}\text{Vn}_{23} \rightarrow \text{Ti}_{22} + e^+ + \nu$	15.98 d	0.698	0.50
$^{124}\text{I}_{53} \rightarrow \text{Te}_{52} + e^+ + \nu$	4.18 d	1.540	0.11
$^{64}\text{Cu}_{29} \rightarrow \text{Ni}_{28} + e^+ + \nu$	12.7 h	0.650	0.19
$^{11}\text{C}_6 \rightarrow \text{B}_5 + e^+ + \nu$	20.38 m	0.960	0.96

### 1.2.2 Beta decay

The proton and the anti-proton are the only stable particles in free space known [23]. The neutron is unstable and can decay to a proton, a beta particle, and an anti-neutrino, as in equation (1.2) [19, 24],

$$n \rightarrow p + \beta^- + \nu \quad (1.2)$$

A neutron will be stable in an atomic nucleus if the decay in equation (1.2) is energetically forbidden, or equivalently, requires an increase in the nuclear binding energy.

On contrary, the proton bound in a nucleus may decay to a neutron, a beta particle, and an anti-neutrino if this is energetically favored, or equivalently requires a decrease in nuclear binding energy.



And the Feynman diagram,

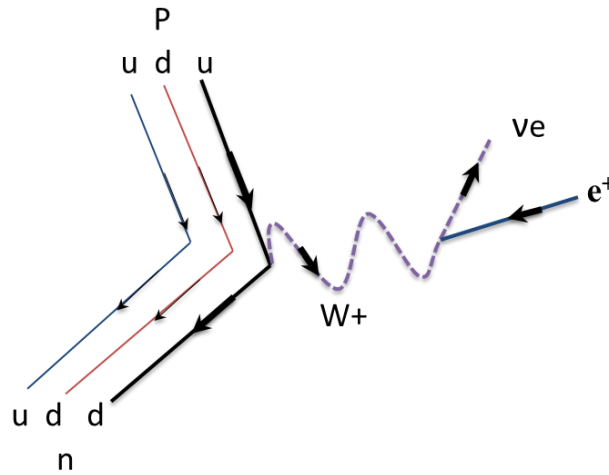
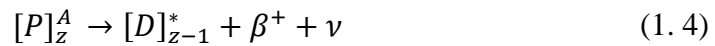
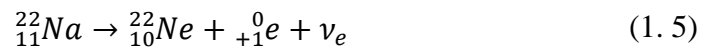


Figure 1.4: Proton decay via emission of a  $W^+$  to a neutron resulting in a positron and a neutrino [25].



$P$  and  $D^*$  represent the parent and excited daughter nuclei respectively.

$^{22}\text{Na}$  is a particularly suitable radionuclide; it has a positron yield of 90.4 % and a 2.602 years physical half-life with 11 days biological half-life [15, 26]. Moreover,  $^{22}\text{Na}$  is available in a dilute  $^{22}\text{NaCl}$  or  $^{22}\text{Na}_2\text{CO}_3$  solution, which is easy to handle. The  $\beta^+$  decay equation of  $^{22}\text{Na}$  is;



According to the decay scheme (figure 1.5),  $^{22}\text{Na}$  source is considered the best choice for studying bulk materials. It decays by the emission of positrons (yield of 90.326%) and electron capture (with 9.61%) to the first excited state of  $^{22}\text{Ne}^*$ , which has a very short lifetime (3.7 ps). Finally,  $^{22}\text{Ne}^*$  de-excites to the ground state with the emission of gamma-photon of 1.274 MeV energy, which is an indication of the birth of the positron. Positron, which injected into a material, will annihilate with an electron giving a 511 keV gamma photon (the rest mass energy of the positron  $m_0c^2$ ). The time difference between 1274 keV and 511 keV photons is the positron lifetime.

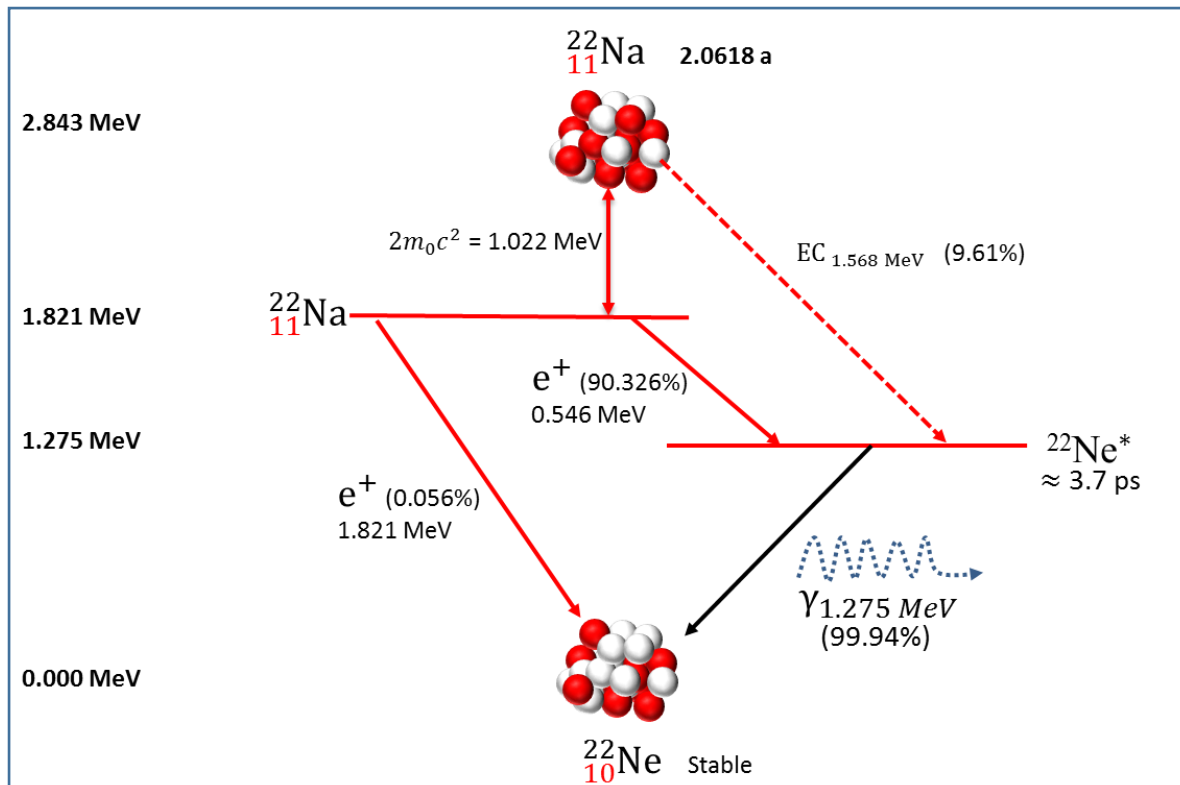


Figure 1.5: Decay transitions for  $^{22}\text{Na}$ , modified from [27].

### 1.3 Interactions of Positron with Matter

A positron reaches a solid surface may either backscatter or permeate into the material due to its high kinetic energy, which will be lost during the implantation via various interaction mechanisms. During the implantation process, the positron will lose its energy through interaction reaching the thermal energy, then it diffuse through the material until it annihilates with an electron. It may be trapped during diffusion in to a lattice defect, and then it annihilates there [15]. Understanding of positron collision processes in solids promotes the description of the comparable electron processes using monoenergetic electrons as probes of solid samples [28].

#### 1.3.1 Backscattering

There is a possibility of highly energetic positrons to backscatter from the material and that is contingent on the material and the energy of positrons. Positron scattering and energy loss in

the matter is important for different applications, such as studies of surfaces by the positron beam. The backscattering probability was treated theoretically by Monte-Carlo simulation and it was compared with experimental results [29]. *Mäkinen et al.* [29] measured positron backscattering from highly oriented pyrolytic graphite C, Si (100), Ge (surface orientation not known) and polycrystalline Au. The angle of incidence deviates from the normal direction by less than  $5^\circ$  when the incident energy is  $E > 2$  keV because of the transverse energy of the positron beams. Figure 1.6 shows that in low- $Z$  materials like graphite or Si, the variation of the positron energy with the backscattering probability is very small. At energies higher than 10 keV, the backscattering probability reaches the saturation and gradually starts to decrease. The increase of the backscattering ratio as a function of the incident energy becomes clear at atomic numbers  $Z > 20$ . In the high- $Z$  targets like Au, the backscattering probability saturates above 20 keV [29].

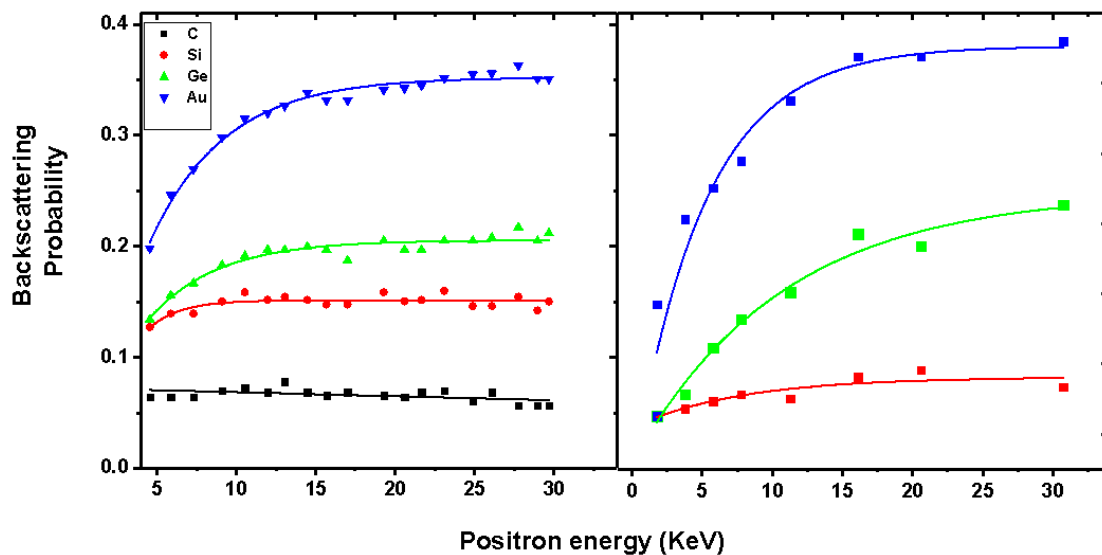


Figure 1.6: Right: Monte Carlo calculations of positron backscattering probability for Si, Ge, and Au at incident energies 1-30 keV. Left: Experimental positron backscattering probabilities as a function of the incident energy for graphite, Si, Ge, and Au [15, 29].

### 1.3.2 Thermalization and diffusion

Regardless of the positron sources, which will be used, the kinetic energy of positrons is several hundred times higher than the thermal energy of the positrons inside the solid. Positrons from a  $^{22}\text{Na}$  source have a most likely kinetic energy of approximately 200 keV [30]. The positrons penetrate into the solid, they will be thermalized within less than few picoseconds ( $\sim 3\text{ps}$ ) and thereafter they become in thermal equilibrium with the solid. Because there are not at the same time several positrons in the solid, the energy of the

positron can be described by a Maxwell- Boltzmann distribution. The kinetic energy of positrons is on average  $3/2 k_B T$ .

The energy of the positrons and the examined materials determine the mechanisms, which lead to the thermalization process [31]. Elastic or inelastic scattering with core and valence electrons cause the loss when positrons energies are greater than approximately 100 keV [15] [32] with timescales on the order of  $10^{-13}$  s [33]. For energies lower than a few tenths of eV, the energy loss mechanism depends on the material. From about 0.5 eV to a few 100 keV plasmonic excitations dominates the energy loss [31]. Positrons with energies from some meV to 1 eV lose their energies via phonon scattering process. After thermalization ( $\langle E_{th} \rangle = 3/2 k_B T \sim 40$  meV), positron diffuses through the lattice and behaves like a charged particle. Positrons are repelled by the positively charged nuclei and have the highest probability density in the interstitial regions (see figure 1.7). The diffusion of positrons can be described with the use of the diffusion annihilation equation [33];

$$\frac{\partial}{\partial t} n(\vec{r}, t) = D_+ \nabla^2 n(\vec{r}, t) - \lambda_b n(\vec{r}, t) \quad (1.6)$$

where  $n(\vec{r}, t)$  is the positron density at position  $\vec{r}$  and time  $t$ ,  $\lambda_b$  is the bulk annihilation rate and  $D_+$  is the positron diffusion constant, which can be calculated by the three-dimensional random walk theory [30],

$$D_+ = \frac{\langle v^2 \rangle t_r}{3} \quad , \quad \langle v^2 \rangle = \frac{3k_B T}{m^*} \quad (1.7)$$

where  $t_r$  is the relaxation time for scattering mechanism,  $k_B$  is the Boltzmann constant,  $T$  is the temperature and  $m^*$  is the effective positron mass which equals 1.3-1.7 of the rest mass of positron [34]. The positron diffusion length is defined from Equation (1.8) [15] as,

$$L_+ = \sqrt{\tau_b D_+} \quad (1.8)$$

The positron diffusion lengths value is in the range of 200-500 nm and is limited by the bulk positron lifetime  $\tau_b$  [35].



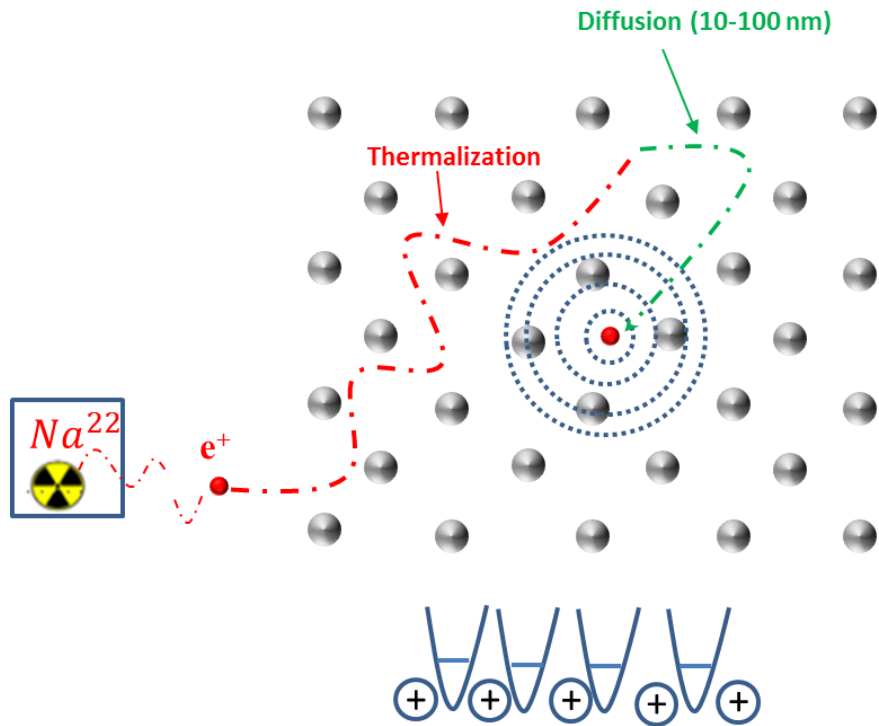


Figure 1.7: Positron wave function at an interstitial space inside a perfect crystal after thermalization and diffusion.

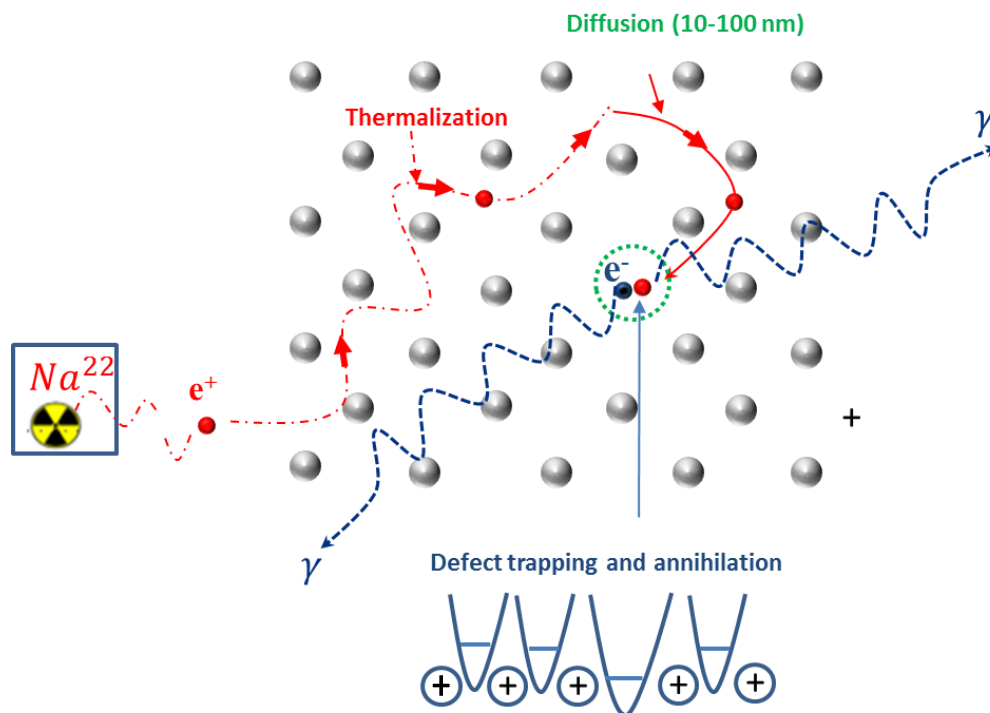


Figure 1.8: Thermalization, diffusion, and trapping of the positron. The potential is increased for a point defect in the lattice.

### 1.3.3 Positron trapping in metals

Positrons entered the material delocalized into a free Bloch state, nevertheless, if a suitable defect center (i.e. single vacancies, complex-vacancies or dislocations) present in the crystal lattice, a deep negative potential will be formed (since a nuclear charge is missing) and the positron can be localized at this site [36]. Positrons can annihilate with electrons from the ‘perfect’ lattice, or they can first trap into localized states at the defect sites (low electron density) and annihilate with electrons in the local environment (see figure 1.8). The binding energy of the positron inside the defect depends on the depth of the potential well. Positron captured into an open volume defect is normally controlled by one of two processes; transition-limited trapping (limited by the rate of making the transition from the delocalized state to deep localized state related to the defects), or diffusion-limited trapping (limited by the rate of diffusion of the positrons to the defects), see figure 1.9.

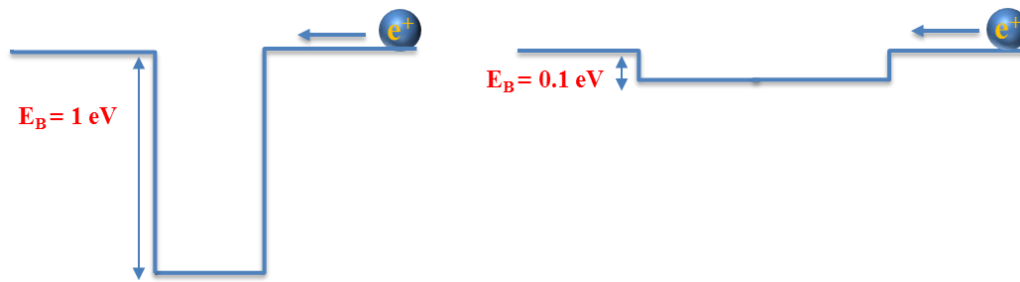


Figure 1.9: Schematic representation of transition (Left) and diffusion (Right) trapping [37, 38].

The trapping rate is given by the Fermi’s golden rule [15],

$$\kappa = \frac{2\pi}{\hbar} \sum P_i M_{i,f}^2 \delta(E_i - E_f) \quad (1.9)$$

Since,  $P_i$  is the occupation probability of the initial state  $i$ ,  $M_{if}$  the transition matrix element between initial and final states  $i$  and  $f$ ,  $E_i$  and  $E_f$  the respective energies. The trapping rates for diffusion and transitional trapping  $\kappa_{dl}$ ,  $\kappa_{tl}$  considering a spherical defect with radius  $r_d$  can be expressed by,

$$\kappa_{dl} = 4\pi r_d D_+ C \quad (1.10)$$

$$\kappa_{tl} = \mu C \quad (1.11)$$

$$\kappa = \frac{\kappa_{tl} \kappa_{dl}}{\kappa_{tl} + \kappa_{dl}} \quad (1.12)$$

Where  $\mu$  is the positron trapping coefficient and. In both types of trapping, the trapping rate  $\kappa$  is proportional to the defect concentration  $C$ .

### 1.3.3.1 Positron trapping model in metals

Positron capture in a single open-volume defect type is mostly described by the two-state simple trapping model (STM) which is used for calculation of defect concentration [39]. STM model assumed that there are no interactions among the positrons with each other, the positrons are not captured during thermalization, the defects distributed homogeneously and de-trapping of positrons trapped at defects can be neglected [15]. Figure 1.10 shows a schematic diagram of one defect trapping model; thermalized positrons may annihilate from the delocalized state in the defect-free bulk with annihilation rate  $\lambda_b$  ( $\frac{1}{\tau_b}$ ). Also, if the material contains high enough concentration of the defects, positrons will be trapped in the defect with a trapping rate  $\kappa_d$ , and will annihilate then with the emission of 511 keV  $\gamma$  quanta with annihilation rate  $\lambda_d$  ( $\frac{1}{\tau_d}$ ).

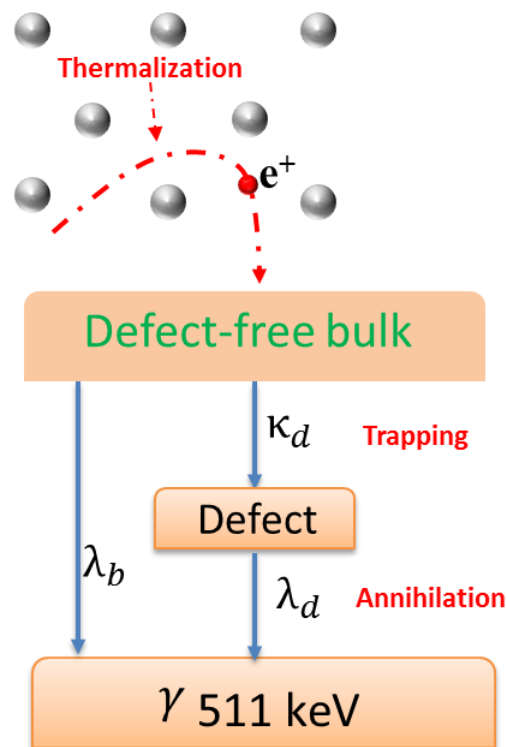


Figure 1.10: Schematic diagram of single defect trapping model [15].

STM can be described by a set of differential equations [15, 40];

$$\frac{dn_b(t)}{dt} = -\lambda_b n_b(t) - \kappa_d n_b(t) \quad \& \quad \frac{dn_d(t)}{dt} = -\lambda_d n_d(t) + \kappa_d n_b(t) \quad (1.13)$$

The functions  $n_b(t)$  and  $n_d(t)$  are probabilities of finding a positron in the bulk and in the trapped state at time  $t$ , respectively.

With the initial condition at  $t = 0$ ,  $n_b(0) = 1$  (100% of positrons at  $t = 0$ ) and  $n_d(0) = 0$ , the probability that positron is still alive at time  $t$ ;  $n(t)$  is the solution of Eq. (1.13);

$$\begin{aligned} n(t) &= n_b(t) + n_d(t) \\ &= \left(1 - \frac{\kappa_d}{\lambda_b + \kappa_d - \lambda_d}\right) \exp(-\lambda_b + \kappa_d)t \\ &\quad + \frac{\kappa_d}{\lambda_b + \kappa_d - \lambda_d} \exp(-\lambda_d t) \end{aligned} \quad (1.14)$$

The negative derivative of Eq. (1.14) is exactly the decay spectrum of positrons with two exponential components having the lifetimes  $\tau_1, \tau_2$  and their intensities  $I_1, I_2$ .

$$D(t) = -\frac{dn}{dt} = I_1 \exp\left(-\frac{t}{\tau_1}\right) + I_2 \exp\left(-\frac{t}{\tau_2}\right) \quad (1.15)$$

Where  $\tau_1 = \frac{1}{\lambda_1} = \frac{1}{\lambda_b + \kappa_d}$  is the reduced bulk lifetime, it includes positron annihilation from the Free State and disappearance of positrons from the free state by trapping into defects [40].  $\tau_2 = \frac{1}{\lambda_d}$  Which is the lifetime of positrons trapped at defects which; it is constant for a specific defect and changes only with any change in the size and the type of the defect. The relative intensities of  $\tau_1$  and  $\tau_2$  are;

$$I_2 = \frac{\kappa_d}{\lambda_b + \kappa_d - \lambda_d}, \quad I_1 = 1 - I_2 \quad (1.16)$$

The derivative of the decay spectrum  $D(t)$  is the lifetime spectrum  $N(t)$ ;

$$N(t) = \left| \frac{dD(t)}{dt} \right| = \frac{I_1}{\tau_1} \exp\left(-\frac{t}{\tau_1}\right) + \frac{I_2}{\tau_2} \exp\left(-\frac{t}{\tau_2}\right) \quad (1.17)$$

The positron trapping rate to defects  $\kappa_d$  is directly proportional to the concentration of defects  $C_d$  and the proportional constant is the specific positron trapping rate (or trapping coefficient)  $\mu$ ;

$$\kappa_d = \mu C_d = I_2 \left( \frac{1}{\tau_1} - \frac{1}{\tau_2} \right) = \frac{I_2}{I_1} \left( \frac{1}{\tau_b} - \frac{1}{\tau_d} \right) \quad (1.18)$$

$\tau_b$  is the bulk lifetime and  $\tau_d$  is the defect lifetime (identically  $\tau_2$ ). If the size of the open volume is larger than that of the single vacancy, the electron density will decrease and this reduces the probability of annihilation and consequently increases  $\tau_d$ . Thus,  $\tau_2$  reflects the size of the open volume defect. Positroners are widely using the average positron lifetime, which can be calculated as;

$$\tau_{av} = \bar{\tau} = \sum_{i=1}^{k+1} I_i \tau_i \quad , k \text{ is the number of defects} \quad (1.19)$$

The trapping rate  $\kappa_d$  can be from  $\bar{\tau}$  determined [15];

$$\kappa_d = \frac{1}{\tau_b} \frac{\tau_{av} - \tau_b}{\tau_d - \tau_{av}} = \frac{\eta}{\tau_b(1-\eta)} \quad (1.20)$$

Where  $\eta$  is the annihilation fraction and given by;

$$\eta = \int_0^{\infty} n_t(t) dt = \frac{\kappa_d}{\lambda_b + \kappa_d} \quad (1.21)$$

When the spacing between defects is much smaller than the positron diffusion length in the bulk (the defect concentration is very high), a saturation trapping will occur since all positrons are trapped; thus  $\bar{\tau} = \tau_d$  with 100%  $I_2$ .

### **1.3.3.2 Positrons trapping by Shallow positron traps**

In addition to vacancies, positrons can be trapped at trapping sites with very a low binding energy  $\sim 40$  meV at low temperatures. *Saarinen et al.* [41] found that below 200 K positrons are trapped in un-doped GaAs and the simple positron-trapping model with one type of vacancy defect was not sufficient to explain the trapping process. Positron localized in the Rydberg states around a negative center, which is an impurity or native defect in n-type GaAs. In Al-alloys, principally, coherent precipitations could act as shallow positron traps [42]. The open volume defects and the undisturbed dislocations which have a very small binding energy

of the positrons ( $\sim 80\text{meV}$ ) can act also as shallow traps [43]. It was found that the positron lifetime is very close to the bulk value (figure 1.11) [15]. In normal cases, the strong repulsive Potential of the nucleus to the positrons keep them as far as possible from the nucleus but in case of the presence of negatively charged defects overlapping of repulsive and attractive Coulomb potentials will occur resulting in the shallow Rydberg states.

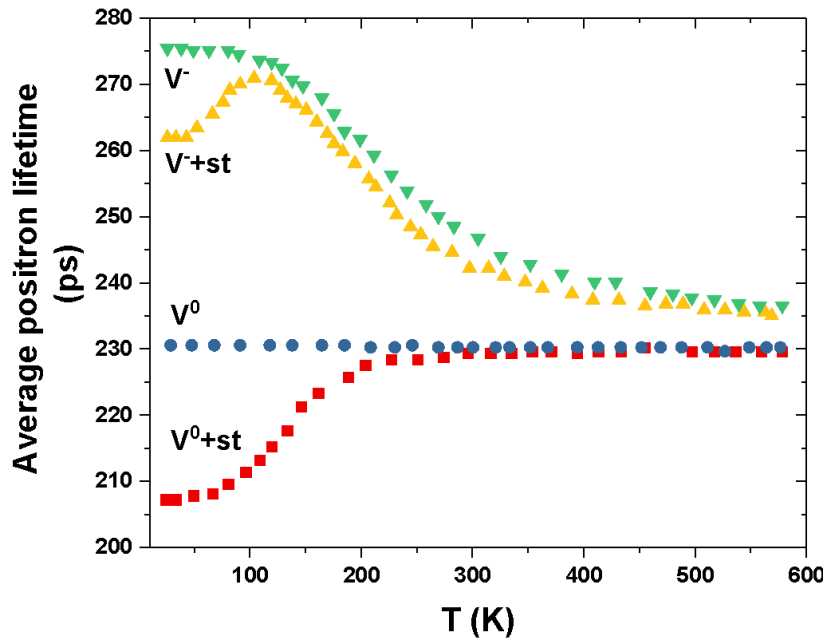


Figure 1.11: The average positron lifetime for neutral, negatively charged vacancies ( $V^0$  and  $V^-$ ) and shallow traps as a function of the temperature [15].

The small binding energy of the positrons in the Rydberg states leads to a temperature dependence of positron trapping by thermally induced detrapping [37]. The detrapping positron can be described in terms [44];

$$\delta = \frac{\kappa_{st}}{\rho_{st}} \left( \frac{m^* K_B T}{2\pi\hbar^2} \right)^{\frac{3}{2}} \exp\left(-\frac{E_{st}}{K_B T}\right) \quad (1.22)$$

Where  $\kappa_{st}$ ,  $\rho_{st}$ ,  $E_{st}$  are the trapping rate, concentration and positron binding energy to shallow traps. Figure 1.12 illustrates the two trapping stages of the negatively charged vacancies. There are two trapping possibilities; they can be trapped either to the Rydberg states (shallow traps) with a trapping rate  $\kappa_R$  ( $\kappa_{st}$ ) or to the deep state of the vacancy with a trapping rate  $\kappa_d$ . In contrast to the ground state of the vacancy, the positron can be thermally detrapped from the Rydberg state (shallow trap) with detrapping rate  $\delta_R$  ( $\delta_{st}$ ). Positrons trapped to shallow states can either be transported to the deep state with a transition rate  $\mathfrak{G}_R$  or annihilate with an annihilation rate  $\lambda_b$ .

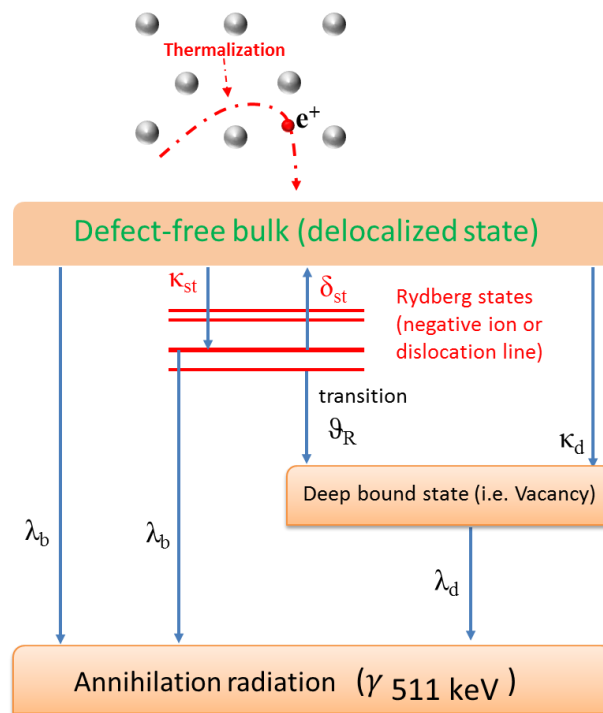


Figure 1.12: Schematic diagram of two trapping stages of the negatively charged vacancies [15].

### 1.3.3.3 Positrons trapping by Dislocations

In plastically deformed metals positrons are trapped at dislocation lines and annihilate with a lifetime slightly shorter than that of positrons trapped at mono-vacancies [45, 46]. *Smedskjaer et al.* [47] calculations showed that the undisturbed dislocation lines act as shallow positron traps (binding energy  $\approx 0.1$  eV). If the lines have large open volumes (i.e. Jogs), Positron is firstly weakly localized at shallow traps in the dislocation core, then it diffuses along the dislocation line and finally they reach the deep trapping centers (see figure 1.13) [46]; thus the trapping model is very similar to the two trapping stages of the negatively charged vacancies mentioned above (figure 1.12).

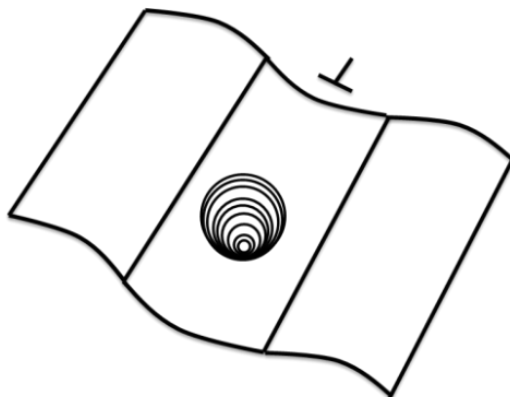


Figure 1.13: Schematic image of a dislocation line with a deep trap center.

The dislocation density can be determined by Positron lifetime spectroscopy; hence the ratio of detrapping and trapping rate for a dislocation line with shallow traps can be described as [44];

$$\frac{\delta}{\kappa} = \frac{m^* K_B T}{2 \rho_{dis} \hbar^2} \operatorname{erf}^{-1} \left( \sqrt{\frac{E_{dis}}{K_B T}} \right) \exp \left( -\frac{E_{dis}}{K_B T} \right) \quad (1.23)$$

$E_{dis}$  is the positron binding energy to the dislocation line; this equation differs from equation 1.22 due to the different geometry of the shallow state.

### 1.3.3.4 Positrons trapping by vacancy clusters (voids)

The agglomeration of vacancies forming vacancy clusters (i.e. small voids) can increase the trapping coefficient [48]. When the number of vacancies in the cluster is less than 10 vacancies ( $N_V < 10$ ), the trapping coefficient of vacancy clusters  $\mu_{N_V}$  is directly proportional to the number of vacancies in the cluster  $N_V$ , i.e.  $\mu_{N_V} = N_V \mu$ , where  $\mu$  is the trapping coefficient of a monovacancy [15, 40]. However, the trapping coefficient saturates for the high number of vacancies ( $N_V > 10$ ) (see figure 1.14). Čížek *et al.* [49] calculated the positron lifetime in the vacancy cluster in  $\alpha$ -Fe and obtained a very similar result; by increasing the number of vacancies in the cluster, the lifetime of trapped positrons increases and then gradually saturates for larger clusters [40].

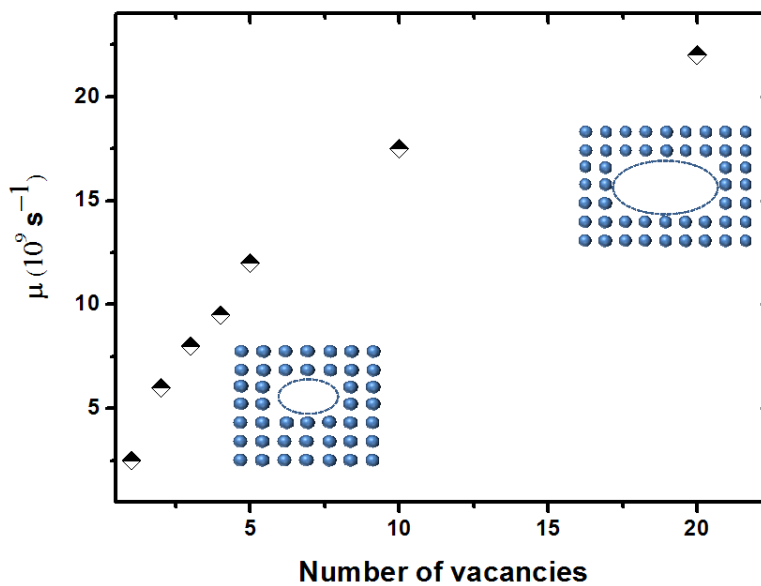


Figure 1.14: Numerical data from Nieminen and Laakkonen of trapping coefficient vs the number of vacancies in the cluster in Al [48].



### 1.3.3.5 Positrons trapping by vacancy-solute complexes

In alloys an interaction may occur between vacancies and some alloyed atoms (solutes), which form a vacancy-solute complex with a certain binding energy. *Wolverton* [50] calculated the binding energy of some elements to vacancies (i.e. Sn) in the Al matrix. The lifetime of trapped positrons in the vacancy-solute complex is found to be shorter than that of the monovacancy, since the solute atom having larger atomic radius usually reduces open volume in the vacancy [40].

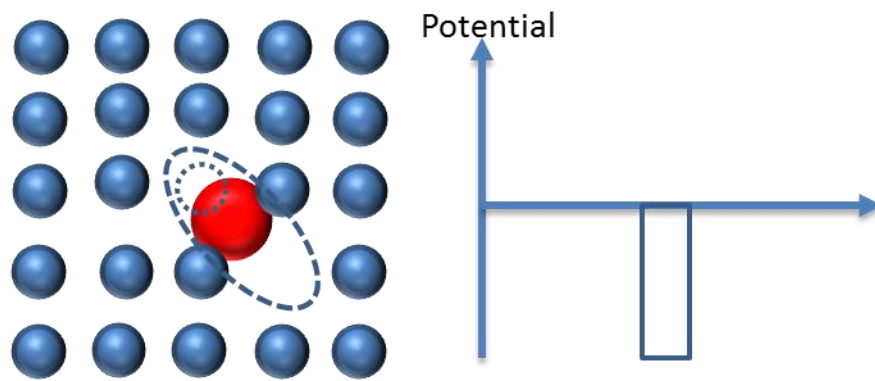


Figure 1.15: Scheme of positron trapping by vacancy-solute complex [51].

### 1.3.3.6 Positrons trapping by precipitates

Positron traps can be distinguished with respect to the origin of their positrons potential, either open volume (vacancy) or positron affinity (precipitates). The positron affinity plays the main role in case of precipitate attractiveness for positrons [52]. Coherent precipitates (i.e. GP zones) can be a potential well for positrons. If positron lowest energy state confined in a precipitate  $x$  is lower than that in the matrix Al ( $\Delta E_{x,Al}^+ < 0$ ), thus precipitate attracts positrons, otherwise positrons are repelled from the precipitate ( $\Delta E_{x,Al}^+ > 0$ ), see figure 1.16 (A,B) [40]. Moreover, positron trapping by a precipitate happens only at a certain size [52]. Suppose the precipitate is described by a spherical three-dimensional potential well with the depth of  $\Delta E^+$ , then the precipitate can bind the positron if its radius is bigger than the critical radius  $r_c$ ;  $r > r_c$  and  $r_c \approx \frac{5.8 a_0}{\sqrt{\Delta E^+}}$ , where  $a_0 = 52.9 \text{ nm}$  is the Bohr radius. In case of weak attractive potential of the precipitate (smaller difference in the positron affinity between the precipitate and the matrix), precipitates may act as a shallow positron trap and the ratio of detrapping and trapping rate is [15];

$$\frac{\delta}{\kappa} = \frac{1}{V_t \rho_t} \left[ \frac{\sqrt{\pi}}{2} \operatorname{erf} \left( \sqrt{\frac{E_t}{K_B T}} \right) - \sqrt{\frac{E_t}{K_B T}} \exp \left( -\frac{E_t}{K_B T} \right) \right] \exp \left( -\frac{E_t}{K_B T} \right) \quad (1.24)$$

where  $E_t$ ,  $V_t$  and  $\rho_t$  are the positron binding energy, the volume, and the density of the precipitate, respectively. It is known that the energy required for an electron to escape to the vacuum is the electron work function. The electron work function ( $\varphi_-$ ) is separated into chemical potential ( $\mu_-$ ) and the surface dipole potential ( $\Delta$ ) which repels the electrons and keeps them from escaping into the vacuum [53, 54].

$$\varphi_- = -\mu_- + \Delta \quad (1.25)$$

Contrary to the electron, positron is attracted by the surface dipole potential;

$$\varphi_+ = -\mu_+ - \Delta \quad (1.26)$$

The sum of electron and positron chemical potentials is the positron affinity ( $A_+$ ) [52];

$$A_+ = -(\varphi_- + \varphi_+) = \mu_- + \mu_+ \quad (1.27)$$

Where  $A_+$  is a negative quantity and more negative value for a certain phase or an element means a stronger potential for positrons. Theoretical calculations of the positron affinity for most pure elements can be found in Ref. [52].

The surface measurement such as reemitted-positron spectroscopy is very helpful in order to measure positron work function, and hence the affinity [55]. Figure 1.16 shows a schematic illustration of different types of precipitates, which can trap positron; fully coherent precipitates, semi-coherence precipitates and incoherent precipitates. Incoherent and semi-coherent precipitates have misfit defects located at the precipitate-matrix interface, which can trap the positron too. However, If the precipitates contain open volume defects in its interior, the positron is trapped first by the potential of the surface trap and then by the deeper potential [56, 57].

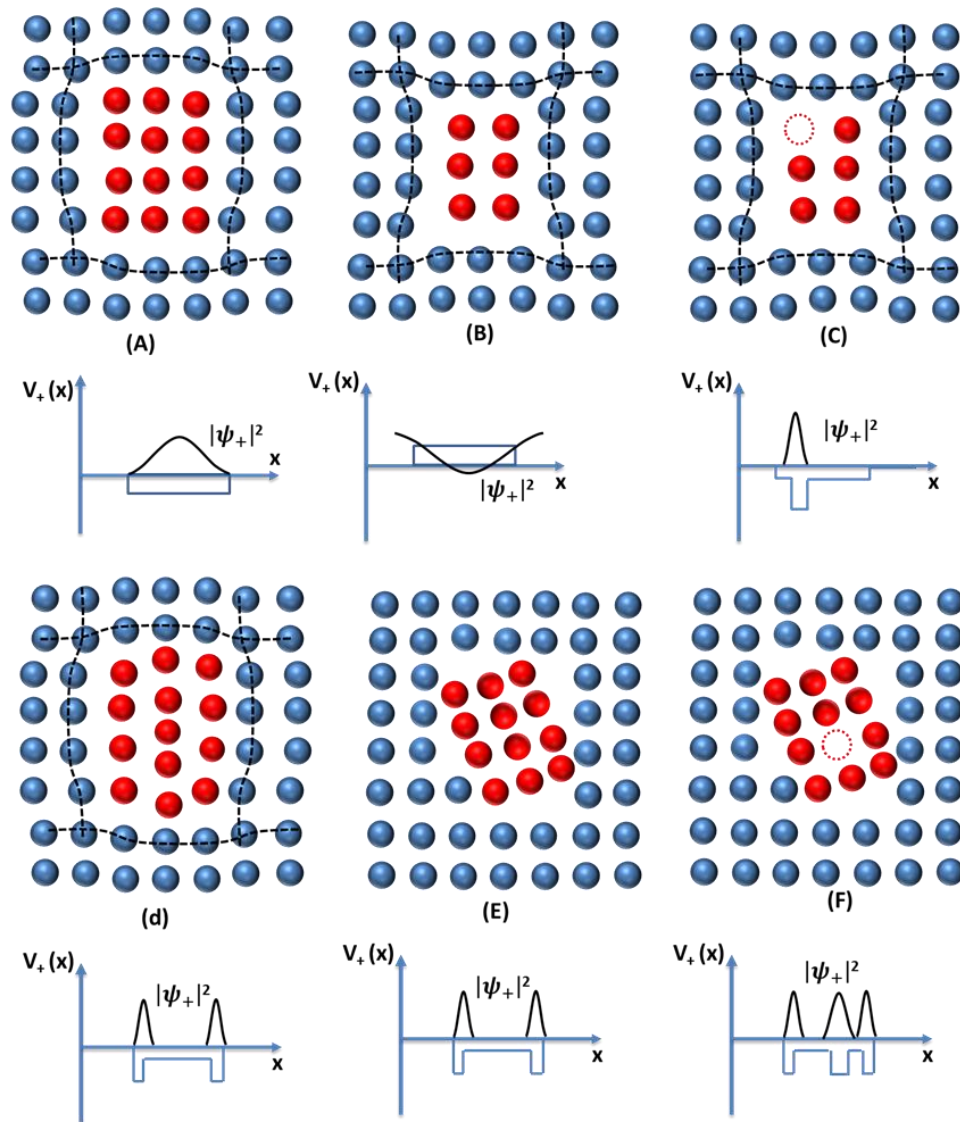


Figure 1.16: Positron potentials  $V_+(x)$  and wave functions  $\psi_+$  of different types of precipitates, (A) GP zones (Fully coherent precipitates  $\Delta E_{x,Al}^+ < 0$ ), (B) GP zones (Fully coherent precipitates  $\Delta E_{x,Al}^+ > 0$ ), (C) GP zones (Fully coherent precipitate containing a vacancy), (d) semi-coherent precipitates, (E) Incoherent precipitates, (F) Incoherent precipitates containing a vacancy [15, 40].

#### 1.4 Annihilation of positrons and electrons

The annihilation process is a spontaneous emission. To calculate the probability of that emission, quantum mechanics should be applied [3]. The probability of annihilation per unit time (annihilation rate  $\lambda$ ) expressed as [3, 15],

$$\lambda = \pi r_0^2 c n_e(r) \quad (1.28)$$

where  $n_e(r)$  is the electron density,  $r_0$  is the classical electron radius, and  $c$  is the speed of light. From equation 1.28, the electron density can be measured if the positron lifetime is known ( $\tau = \frac{1}{\lambda}$ ).

*Puska and Nieminen* [31] used a standard scheme based on the fact that positron density is very small has no effect on the bulk electron structure [40]. They considered that the effective potential for positron  $V_+(r)$  equals the Coulomb potential  $\phi(r)$  resulting from the electrons and nuclei plus the correlation function  $\gamma_{corr}$ , which describes the increase of electron density due to coulomb attraction between electrons and positrons (enhancement process) [31, 15];

$$V_+(r) = \phi(r) + \gamma_{corr} \quad (1.29)$$

By assuming that only one positron is present in the sample at a given time, the positron density  $n_+(r)$  equals the square of the positron wave function  $\psi^+(r)$ , which can be obtained from the solution of Schrödinger equation for a single particle. The annihilation rate  $\lambda$  is obtained from the overlap of positron density  $n_+(r) = |\psi^+(r)|^2$  and electron density  $n_-(r)$  [15];

$$\lambda = \frac{1}{\tau} = \pi r_0^2 c \int |\Psi^+(r)|^2 n_-(r) \gamma dr \quad (1.30)$$

The electron density at vacancy defects is noticeably lower than the average electron density probed by positrons in a delocalized Bloch state, so from equation 1.30, the lifetime of positrons captured by a vacancy is longer.

### 1.4.1 Positron annihilation spectroscopy

The positron finally annihilates with an electron, and two anti-parallel 511 keV gamma rays normally result. Detection of these annihilation events has led to the development of a number of positron annihilation spectroscopy techniques (figure 1.17). PAS can be classified into two groups, first, one concerned with the electron density (positron annihilation lifetime spectroscopy PALS) and the second based on the sensitivity of positron to electron momentum distribution inside the sample (Doppler broadening spectroscopy DBS and angular correlation annihilation spectroscopy ACAR). The concentrations and the type of the defects can be determined by analyzing the annihilation parameters since the electron density

and the electron momentum distribution at the site of the defect change in comparison with the defect-free crystal.

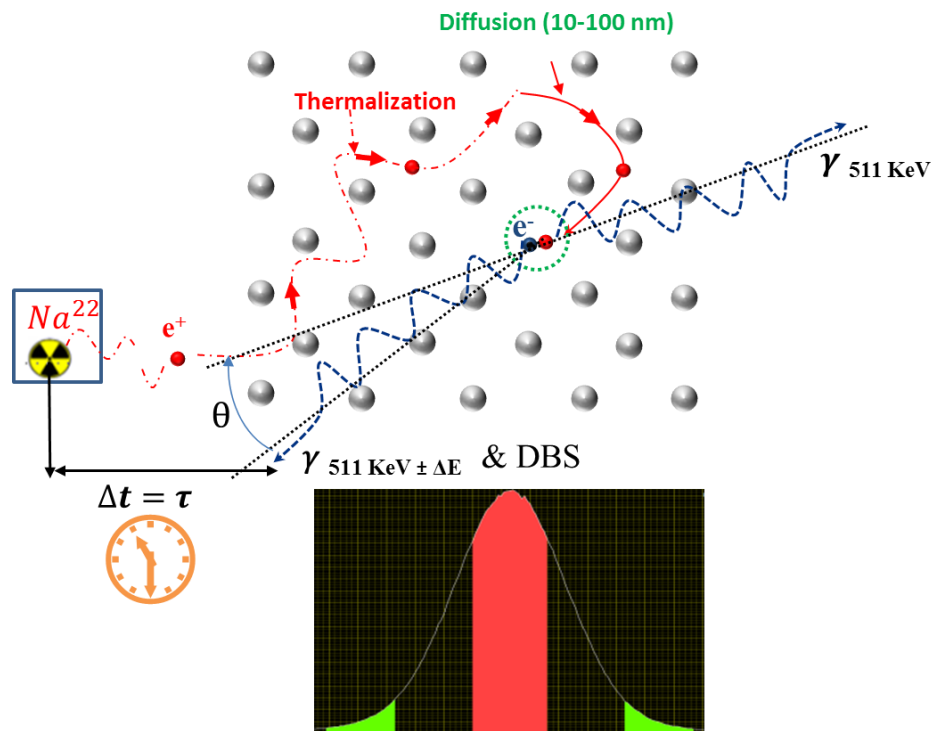


Figure 1.17: Positron annihilation experimental techniques (from [15] ).

#### 1.4.1.1 Positron annihilation lifetime spectroscopy

The defect concentrations and types can be demonstrated with the help of the positron lifetime spectroscopy since the electron density at the defect site is lower than that at the interstitial sites in the defect-free crystal. Thus, the annihilation probability of the positron-electron pair decreases and the average lifetime of the positron increases. As mentioned above,  $^{22}\text{Na}$  is usually used and its main advantage is the high positron yield, the simultaneous emission of 1.275 MeV  $\gamma$  quanta (exactly after 3.7 ps) during the formation of the positron which is used as a starting signal for the determination of the lifetime (figure 1.5). The 0.511 MeV  $\gamma$  quanta are used as the stop signal. The sample, i.e. “sandwich”, is located between two  $\gamma$ -ray detectors, from the time difference between these two signals, the positron lifetime can be determined. The positron thermalization time can be negligible as it is a few picoseconds compared to the positron lifetime. The  $\gamma$  quanta are converted into light pulses by scintillators. Photomultiplier tubes (PMT) then convert these pulses into electrical signals (the energy of the gamma quantum is proportional to the voltage pulse, this enables distinguishing start and stop signals) then passes to the digitizer. The signal is then stored as a lifetime spectrum. The

activity of the source is chosen in such a way that on the average only one positron is located in the sample under investigation [15].

The time resolution and its minimization are crucial to the PALS. Different factors can influence the time resolution such as scintillators, PMT (transit time spread (TTS) and applied high voltage), the pulse shaping, etc. The time resolution is characterized by the Full-Width at Half-Maximum (FWHM), which is the width of the Gaussian peak at half of its amplitude and equals to  $2.355\sigma$  ( $\sigma$  is the standard deviation). The rate of data collection is another important parameter of the spectrometer especially in case of volatile samples and spectrometers having instabilities with time [58]. Positron lifetime spectrum is a histogram of positron annihilation observations, the theoretical positron lifetime spectrum  $N(t)$  for an ideal spectrometer in the sample is the summation of the decay spectra and described by [15, 59];

$$N(t) = \sum_{i=1} \frac{I_i}{\tau_i} \exp\left(-\frac{t}{\tau_i}\right) \quad (1.31)$$

Where  $i$  is the number of lifetime components with relative intensities  $I_i$  and  $(\tau_i = \frac{1}{\lambda_i})$ .

Moreover, the delays within the cables and the software shift the spectrum by  $t_0$ , so  $t$  should be replaced by  $(t - t_0)$ . The lifetime spectrum is convoluted with at least one time resolution function ( $G(t)$ ). The time resolution function is a disturbance of the spectrum, which can be described by a Gaussian function, [15].

$$G(t) = \frac{1}{\sigma\sqrt{\pi}} \exp\left(-\left(\frac{t - t_0}{\sigma}\right)^2\right) \quad (1.32)$$

$$N_{meas}(t) = \sum_{i=1} \frac{I_i}{\tau_i} \exp\left(-\frac{t - t_0}{\tau_i}\right) * G(t) + b \quad (1.33)$$

where  $b$  is the background. On the other hand, the source contribution must be determined before the measurement using a defect-free reference sample, since its lifetime is proven by measurements and theoretical calculations [15].

### **1.4.2 Doppler broadening spectroscopy**

When positron-electron pair annihilates, 511 keV gamma rays are captured by detectors (Eq. 1.34), a peak is formed at this energy and from this peak the concentration of defects can be obtained.

$$E = m_0c^2 \approx 511 \text{ keV} \quad (1.34)$$

The shape of the peak resembles somewhat of a Gaussian distribution (not sharp peak at that specific energy as expected). When an electron and a positron annihilate, they don't give exactly 511 keV, but some deviation happens due to the longitudinal component of electron momentum ( $P_{||} = \pm 2m_e v$ ) in the propagation direction. This causes a double shift equals the energy of one of the gamma rays to a higher value, and the other to a lower value (Eq. 1.35) [60]. The annihilation process occurs after positron thermalization so, at RT according to  $E = k_B T$ , positron momentum is neglected and  $P_{||}$  represents the momentum of the electron only. If the two gamma rays are at an angle  $90^\circ$  from the path of the collision, the two annihilation gamma rays will be very close to the expected 511 keV energy. However it still not exactly 511 keV, since there will be a small deviation of energy due to the small angle difference from the  $180^\circ$  expected from the annihilation. On the other hand, if the positron-electron annihilation produces two gamma rays in the same direction of the collision, or close to it, there will be a large energy difference between the two gamma rays (figure 1.18). It is known that the Doppler observed frequency equals [61],

$$f = f_0 \left(1 \pm \frac{v}{c}\right) \quad (1.35)$$

where  $c$  is the speed of light and  $f_0$  is the source (emitter) frequency.

If  $f$  is the frequency of a moving light source along the x-axis, the observed frequency shift can be written as,

$$\Delta f = f - f_0 = f_0 \left(\pm \frac{v}{c}\right) \quad (1.36)$$

$$E_0 = m_e c^2, \quad E = E_0 \pm \Delta E, \quad (1.37)$$

$$\Delta E = h\Delta f = hf_0 \left(\pm \frac{v}{c}\right) = E \left(\frac{P_{||}}{2m_e c}\right) = \frac{1}{2} P_{||} c$$

This conservation of momentum finally causes broadening or narrowing of the 511 keV peak, depending on the path of produced gamma rays compared to the path of collision of the two particles, as described above.

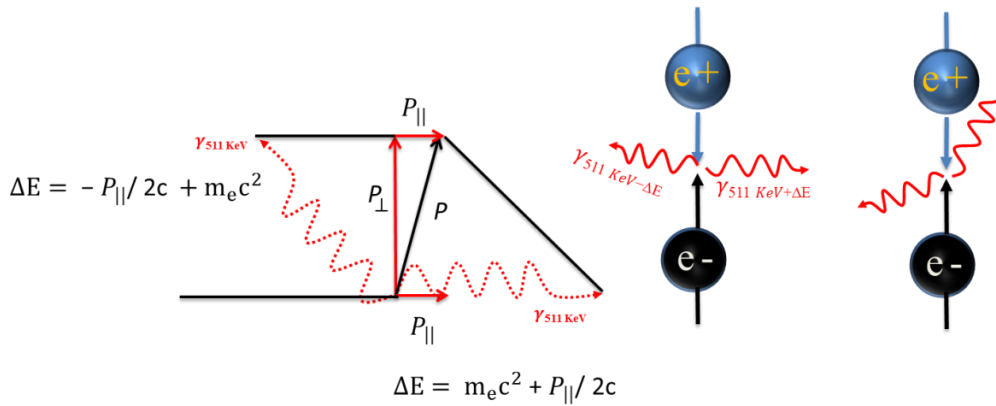


Figure 1.18: Momentum conservation during the  $2\gamma$ -annihilation process,  $P$  is the momentum of the electron-positron pair [62].

The shape (width and height) of the annihilation line depends on the measured sample whether it contains defects or not.

The centripetal force of an electron in a circular motion and the Coulomb force are equal to each other, which can be described as,

$$m \frac{v^2}{r} = k \frac{e^2}{r^2}, \quad p = mv, \quad p = \sqrt{\frac{ke^2 m}{r}} \quad (1.38)$$

If a positron is confined in a defect, it annihilates mostly with a valence electron (low momentum electrons) or with one of the core electrons (high momentum electrons). The peak of this Gaussian distribution deals with the low momentum annihilations, while the high momentum annihilations are expressed by the wings of the peak. This means that when we have only high momentum annihilations, the peak will be lower and the curve broader. However, when annihilations result from low momentum electrons, the peak will be higher and narrower. The analysis of DBS is simplified by the use of the line shape parameters,  $S$  (sharpness) and  $W$  (wing) [63]. These parameters are calculated by taking the area under the region of interest from the 511 keV peak by the total area of the peak (figure 1.19).

$$S = \frac{A_s}{A_0}, \quad A_s = \int_{E_0 - E_s}^{E_0 + E_s} N_D dE, \quad (1.39)$$

$$W = \frac{A_w}{A_0}, \quad A_w = \int_{E_1}^{E_2} N_D dE$$



The S parameter is calculated whereas the interval limits are chosen around the center of the annihilation line energy  $E_0 = 511$  keV,  $E_0 \pm E_s$ . The limits for the evaluation of W parameter,  $E_1$ , and  $E_2$ , should be selected far from the center of the peak.

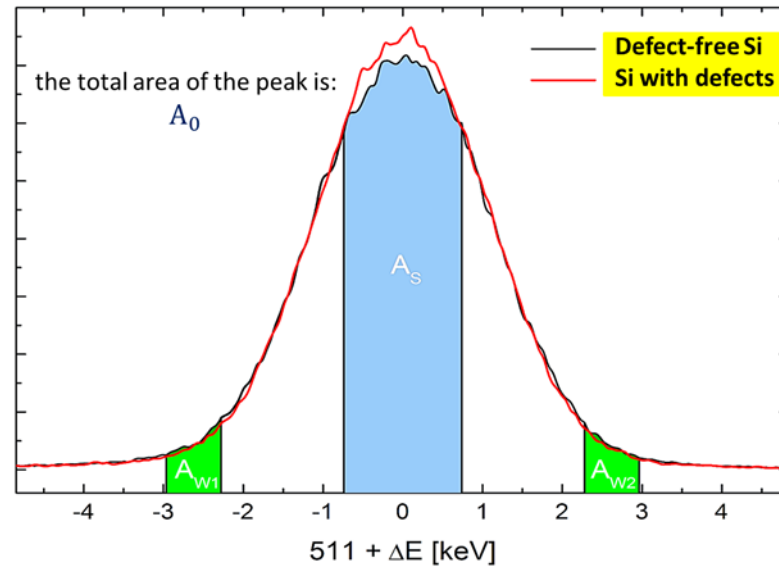


Figure 1.19: Doppler broadening spectra of two samples: defect-free Si and Si with defects. Both spectra are normalized to the same area [15].

The S parameter quantifies the fraction of low momentum annihilation events, while the W parameter quantifies the annihilation fraction in the high momentum region, wing. These two parameters are normalized to the total number of counts in the spectrum. The range used to define the S parameter is typically 50 % of the net area under the curve and that used for defining W parameter is usually taken to be as far from the peak as possible [64]. The statistical error of the S-parameter is given by,

$$\Delta S = \sqrt{\frac{S(1-S)}{N}} \quad (1.40)$$

Since N is the total counts. The smallest error is achieved if  $S = 0.5$ .

The limits were set to  $(511 \pm 0.8)$  keV for evaluation of S parameter and to  $E_1=513.76$  and  $E_2=515$  keV for the W parameter [15]. Usually, S and W parameters are normalized to their corresponding values of the bulk defect-free(reference) sample,  $S_b$  and  $W_b$ . This leads to a reliable comparison of the obtained values obtained from different groups. S and W parameters are responsive to the type and concentration of the defect but W parameter is more

sensitive to the chemical surrounding of the annihilation site. The chemical surrounding of the annihilation site can be identified using the high momentum part of the momentum distribution [15]. A third parameter, R, was introduced and it depends only on the defect types involved and not on the defect concentration [65], it is expressed as,

$$R = \left| \frac{S - S_b}{W - W_b} \right| = \left| \frac{S_d - S_b}{W_d - W_b} \right| \quad (1.41)$$

The S-W plot is used rather than the numerical computation of R using Eq. 1.41, which can be used to identify the number of defect types in the sample [66, 67]. The slope of the straight line through  $(W_b, S_b)$  and  $(W_d, S_d)$  gives the value of R for one defect type.  $S_d$  and  $W_d$  correspond to the complete annihilation of positrons in the defect (saturated trapping). In case of the existence of only one defect type, the apparent S parameter can be derived by weighting the sum of the  $S_b$  and  $S_d$  as [68],

$$S = (1 - \eta)S_b + \eta S_d \quad (1.42)$$

$\eta$  is the weighting factor is the fraction of positrons annihilating in the defect and expressed as [15],

$$\eta = \int_0^{\infty} n_d(t) dt = \frac{\kappa_d}{\lambda_b + \kappa_d} \quad (1.43)$$

The trapping rate can be determined as,

$$\kappa_d = \frac{1}{\tau_b} \frac{S - S_b}{S_d - S} \quad (1.44)$$

#### **1.4.2.1 Coincidence Doppler-broadening spectroscopy**

The Doppler spectrum, measured by a single Ge detector has a considerable high background in the high momentum part, which comes from the pile-up effect in the Ge detector and Compton scattering of the start gamma 1.274 MeV. Thus, W parameter in this case is not accurate enough.. In order to reduce this background, two Ge detectors are used to detect both 511 keV gamma quanta coincidentally (introduced by Lynn et al [69]), this technique is called coincidence Doppler broadening spectroscopy (CDBS) [70, 71, 72]. Doppler-broadened annihilation peak is specified by the momentum distribution of electrons which annihilated with positrons (the momentum of a thermalized positron is negligible). CDBS technique enables the identification of chemical species surrounding positron annihilation sites,

benefiting from unique momentum distribution of electrons for each element [40]. For this reason CDB spectroscopy is a powerful technique used for defects identification in alloys, in addition it can be used to characterize very small precipitates inside the alloy [73-74]. Coincidence measurement (as it is shown in figure 1.20) suppresses background and allows reliable investigation of annihilation radiation resulted from annihilation with core electrons. The energies of annihilation  $\gamma$ -ray is  $E_{1,2} = m_0c^2 \pm \Delta E$ , while  $\Delta E = 0.5 P_{||}c$ . Hence, the difference in energies of the annihilation  $\gamma$ -rays equals two times the Doppler shift, ( $E_1 - E_2 = 2\Delta E$ ), while the sum of these energies is  $E_1 + E_2 = 2m_0c^2 = 1022$  keV with neglecting the electron binding energies, gives the coincidence curve [40, 75]. It is a well-established fact that the interpretation of CDBS spectra may be reliable and comparable when they are presented as a ratio to a defect-free sample [15].

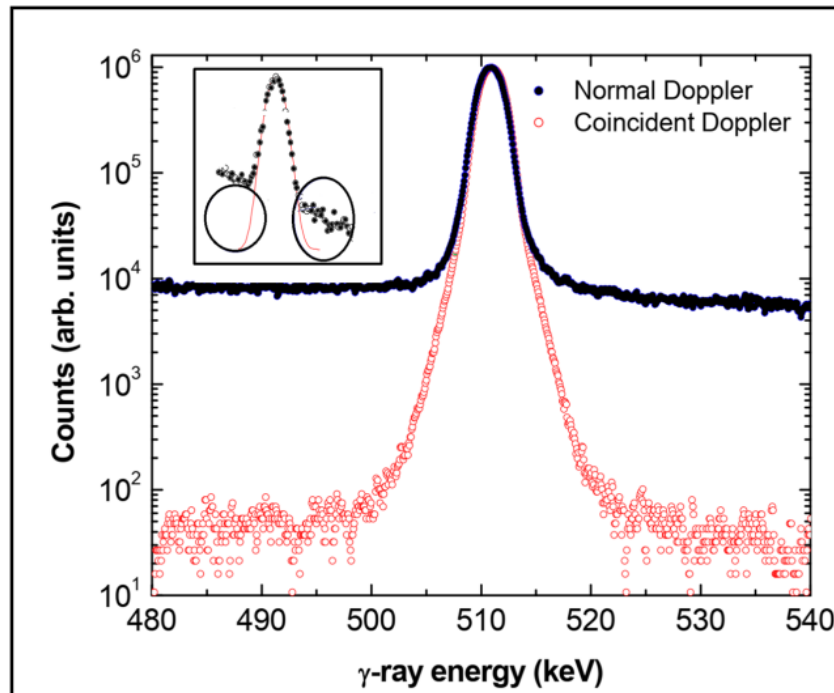


Figure 1.20: Two Doppler broadening spectra normalized to the same area. One of them (black) is measured with a single Ge detector and the other (red) is measured by CDBS [38].

### 1.4.3 Variable energy positron annihilation spectroscopy

Positrons emitted by radioactive nuclei ( $^{22}\text{Na}$ ) for the conventional positron annihilation system (PAS) are directly implanted into the material with an initial energy of several hundreds of keV, and thus penetrate the material to high depths [76]. However, many problems in physics are related to thin layers and to defects near the surface and at interfaces.

Thus, the conventional PAS cannot be used in research on surfaces, thin films or layered structures, because positrons penetrate deeper in the material density. This limitation of conventional PAS can be overcome by using variable positron beam energies lying typically between 0.01 and 50 keV [76]. This technique is called monoenergetic (slow) positron beam system. Positrons of such energies defined by a simple linear accelerators stop typically at an average depth of several nanometers up to few micrometers depending on the energy and the material. Stopping profile of monoenergetic positrons are described as the Makhov's distribution (see Eq.1.45 below). The slow positrons are obtained through the moderation but only a small fraction of less than 1 % of incident positrons undergoes this moderation process. The fast positrons must be separated from the beam of monoenergetic positrons that is used for defect experiments after defined acceleration. The moderation requires the spatial separation of the source and the sample, and thus a beam guidance system must be used [15]. For Doppler- broadening spectroscopy,  $^{22}\text{Na}$  sources are used with an initial activity of 50mCi. The generated positrons are moderated by a material with negative work function such as tungsten W (work function = -3 eV) and then separated from the fast positrons by a velocity filter. Usually, magnetic fields are used for beam transport.

### **1.4.3.1 Positron Implantation**

The penetration profile for different positron energies and materials considering the thermalization process can be determined by using Monte-Carlo simulations. Implanted positrons from a radionuclide source penetrate to a depth that depends on the material density and the maximum energy of the positron. The probability of a positron reaching a depth  $z$  into the material can be described by the empirical equation [31, 77],

$$P(z) = \exp(-\alpha z), \alpha = 17\rho \cdot E_{max}^{-1.43} \quad (1.45)$$

Where  $\alpha$  is the absorption coefficient ( $\text{cm}^{-1}$ ) [77].

The penetration depth depends on the density  $\rho$  ( $\text{g}/\text{cm}^3$ ) and the maximum positron energy  $E_{max}$  (MeV). The maximum penetration depth is defined as  $P(z) = 0.999$  [15]. For the isotropic emitted positron point source the penetration depth according to Schrader *et al.* [78] model is described as [79],

$$P(z) = \exp(-\alpha z) + \alpha z Ei(\alpha z) \quad (1.46)$$

$Ei$  is the exponential integral function.

Implantation of mono-energetic positrons with varying energies is possible also, this experiment is important to provide a complete description of the resulting implantation profile. *Valkealahti et al.* [80] have shown that this can be accurately described by a Makhovian profile [81] (figure 1.21), this was experimentally confirmed by *Vehanen et al.* [82], and is given below,

$$P(z, E) = \frac{mz^{m-1}}{z_0^m} \exp\left(-\frac{z}{z_0}\right)^m, z_0 = \frac{z}{\Gamma\left(1 + \frac{1}{m}\right)} \& \langle z \rangle = \frac{AE^r}{\rho} \quad (1.47)$$

Where  $E$  is the kinetic positron energy in keV,  $\rho$  is the density of the investigated sample,  $\Gamma$  is the gamma function,  $A$ ,  $r$ , and  $m$  are empirically derived parameters, which depend on material and energy [31]. *Valkealahti et al.* [80] listed for some elements (Al, Si, Cu, and Ag) the values of  $A$ ,  $n$  and  $m$ ; frequently used values are,  $A = 40 \mu\text{g cm}^{-2} \text{keV}^{-r}$ ,  $m = 2$ , and  $r = 1.6$  [80, 82]. In order to increase the mean implantation depth, the positron energy should be increased, but the width of the distribution increases too.

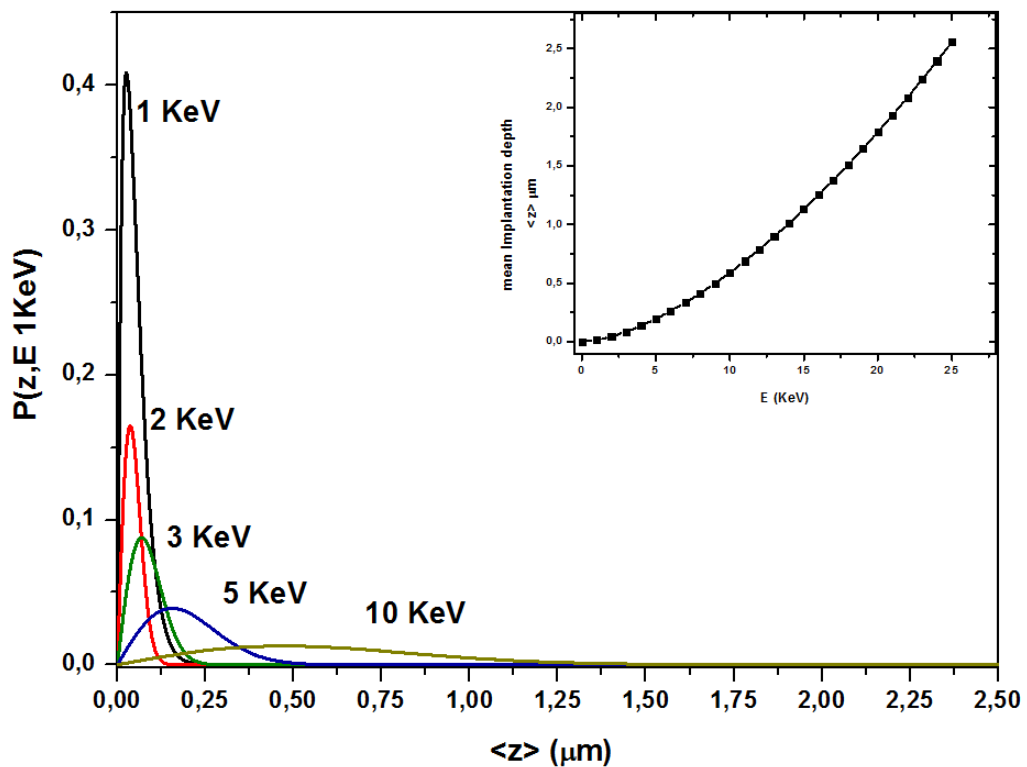


Figure 1.21: Makhovian positron implantation profile in Aluminum. Equation 1.47 was used to calculate the profiles, with  $A = 4 \mu\text{gcm}^{-2} \text{keV}^{-r}$ ,  $m = 2$ , and  $r = 1.6$  (inset mean implantation depth vs positron energy).

### 1.4.4 Positron beam system at Halle (POSSY)

In order to achieve a penetration depth of a few micrometers, moderated positrons are accelerated in a range between few eV and some keV. An energy spectrum of the  $^{22}\text{Na}$  source for positrons is illustrated in figure 1.22. Negative positron work function  $\phi_+$  of many solids is the principle of the moderation process. A thin moderator foil is usually located directly on the top of the source capsule. As the moderator foil thickness is smaller than the positron mean penetration depth, so only a small fraction of positrons thermalize and then diffuse inside it (about 0.05%) and most of the fast positrons (about 87%) penetrate the foil with high energy.

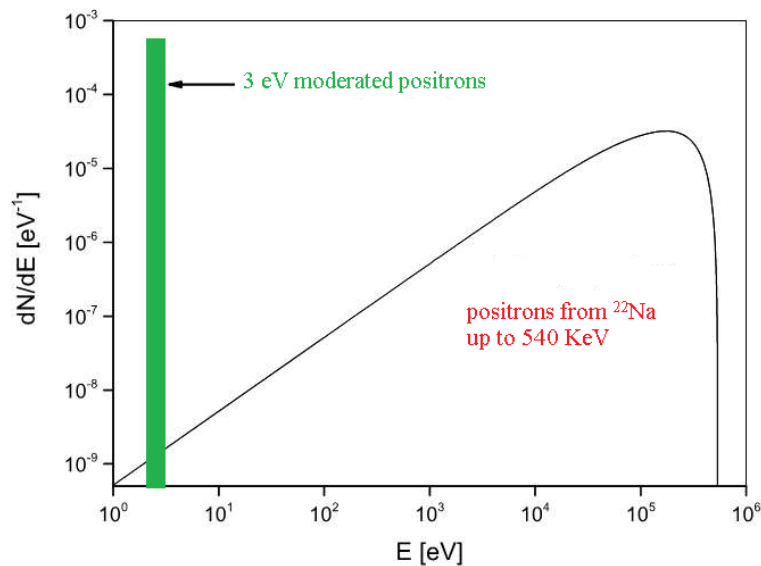


Figure 1.22: The positron emission of a  $^{22}\text{Na}$  source with and without moderator [83].

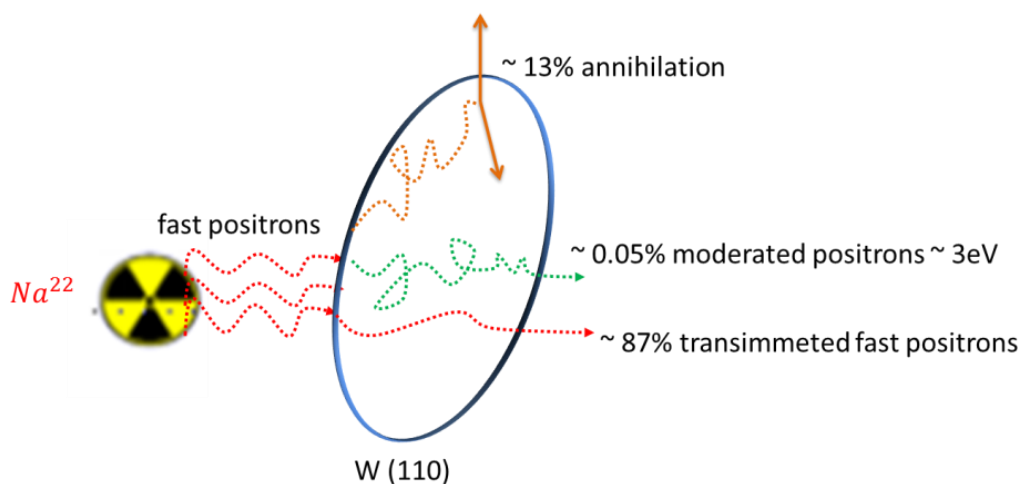


Figure 1.23: Schematic illustration of the positron moderation process by a (110) tungsten foil [15].

As soon as the diffused positrons reach the surface, they are reemitted from the film with kinetic energy equals the work function  $\phi_+$ . Materials with high atomic numbers are favorable for moderation because the ratio of the mean diffusion length to the thermalization distance is larger. A suitable material is a single-crystal tungsten (W) foil in a (100) with the work function  $\phi_+ = -3 \pm 0.3$  eV [83] and moderation efficiency can be up to  $10^{-3}$  [15]. Because of the low moderation efficiency, a strong source and an intensive radiation shield are required.

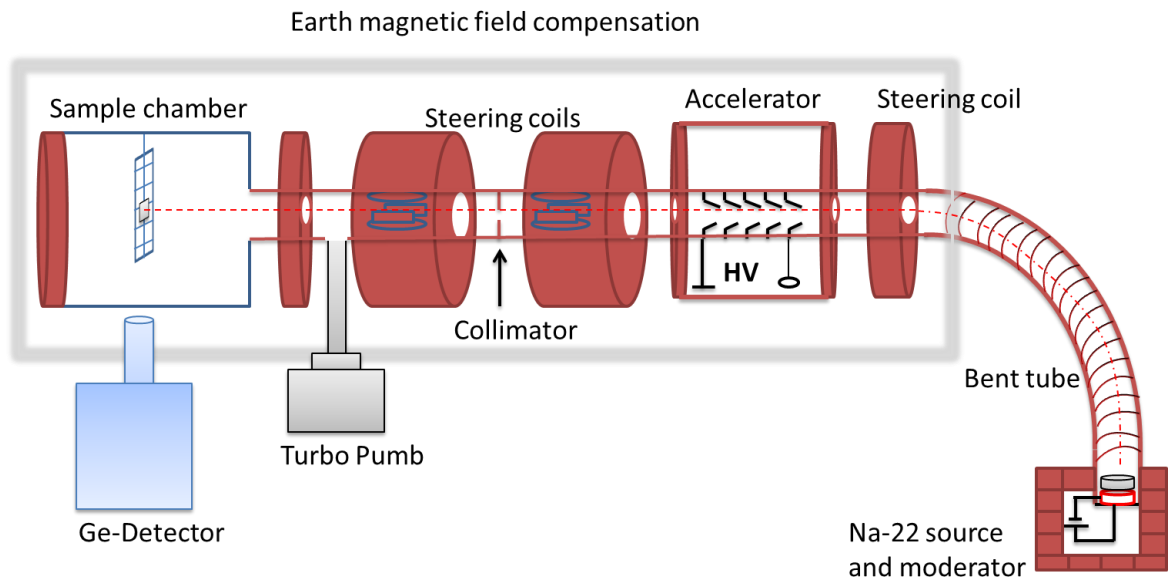


Figure 1.24: Schematic diagram of the slow-positron-beam system at Martin Luther University Halle– Wittenberg (POSSY) (modified from [84]).

What we need to perform an experiment are the moderated positrons, which we can control their energies, thus the moderated positrons (low energy) should be separated from the unmoderated fast positrons by using a velocity (energy) filter. It may be achieved in a magnetically guided system using internal electrodes in an  $E \times B$  filter (electrostatic filter using electrostatic lenses) [85], or by utilizing external magnetic fields perpendicular to the beam direction [86]. Another additional and preferable method is to use bend solenoids. Two copper wire layers wound directly on the surface of the bent tube (10 A and 50 Gauss). The copper wires compensate the effect of centrifugal force and the inhomogeneous magnetic field in the bend. Because of the high voltage can be connected at vacuum tube outside the end of the source, the bent tube is on HV potential too, therefore a transformer with 30 kV is used for isolation in order to keep a constant current mode at the bent tube. For guiding the positron beam and performing surface studies, an ultra-high vacuum is used.

### 1.5 Other defects analytical techniques

Not only PAS techniques but also other techniques are used. Examples of these techniques are Optical microscopy (such as transmission electron microscopy TEM, atomic force microscopy AFM, scanning tunneling microscopy STM, and optical microscopy OM), small angle x-ray scattering (SAXS), neutron scattering (NS), and photoluminescence are also used to characterize point defects [87], but typically (although not always) these are interstitial-type, mainly in bulk materials and usually for large (> few nm) cavities. However, some of them are destructive. Each of them has its own sensitivity and limitation to defects. Figure (1.25) compares the sensitivity of positron annihilation lifetime spectroscopy and some other techniques to detect defects of different sizes and concentration at different depths. It is clear that positron annihilation lifetime spectroscopy is very effective in giving accurate and detailed information about size and concentration at any depth below the effective resolution of other generally applied techniques [88].

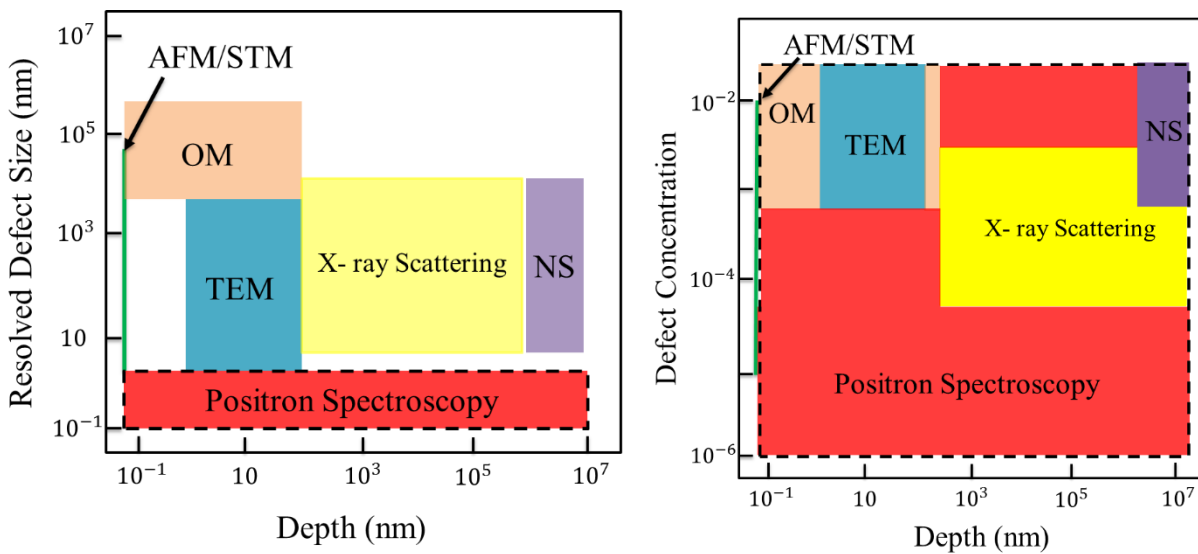


Figure 1.25: Comparison of positron annihilation spectroscopy to other techniques [87, 88].



## Chapter 2 : Defects in crystal

### 2.1 Introduction

In practice, there are no ideal (no perturbations of periodicity) or perfect (only perturbed by thermal vibrations) crystals, only real solids that have a variety of different disorders which may be point, line, surface or volume defects [89]. All real solids are intentional or unintentional impure. Very pure metals (99.9999% or 6N) have one impurity per  $10^6$  atoms. Many properties of solids, especially the mechanical and electrical ones, are significantly influenced by defects and deviations from the ideal structure, and hence their presence can remarkably modify the properties of crystalline solids [90].

#### 2.1.1 Point defects

The dimensionless defects are beneficial to differentiate intrinsic defects from defects produced by impurity atoms, since they distort the crystal at an isolated position [91].

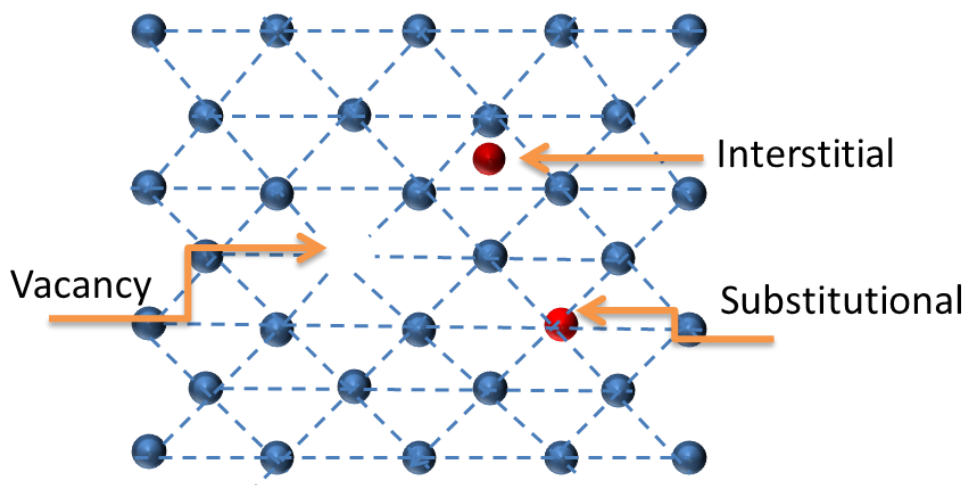


Figure 2.1: Schematic two-dimensional lattice with vacancy, interstitial and substitutional defects [91].

A vacant atomic site (**vacancy**) and **an interstitial** atom are the two types of point defects, which are dominant in a pure metal. The vacancy has been formed by the elimination of an atom from an atomic position; however, the interstitial is an atom in a non-lattice site (figure 2.1). In fact, there are two kinds of the interstitial defects; when the interstitial atom is of the same crystalline solid, it is called self-interstitial. On the other hand, when a foreign atom

occupies the interstitial position, it is called interstitial. Unlike interstitial defect, when the foreign atom replaces an original atom and occupies its lattice site, a **substitutional** defect forms. The neighboring atoms may feel tensile or compressive stress depending on the size of the impurity atom. It is known that vacancies are the dominating defects at high temperature, there is a thermodynamically stable vacancy concentration at temperatures  $> 0$  K. Vacancies and interstitials can be produced in materials by plastic deformation and high-energy particle irradiation [15] however, vacancies are often not stable. The distortion, which defects can produce in the crystal, depends upon the space between atoms and the size of the atoms. The space between atoms has generally a volume of less than one atomic volume, thus the interstitial atoms tend to produce a large distortion among the surrounding atoms.

The change in the free enthalpy (Helmholtz free energy)  $\Delta F$  during formation of  $n$  vacancies or self-interstitials in the crystal is;

$$\Delta F = nE_f - T\Delta S \quad (2.1)$$

Where  $E_f$  is the formation energy of a defect (to remove one atom from its position), and  $\Delta S$  is the change in the formation entropy.  $nE_f$  is a positive energy term and can be compensated by a gain of entropy, but this is offset by an increase in the configurational due to the presence of the defects [90]. ( $\Delta S = S_2 - S_1$ ), where ( $S_1 = k_B \ln G_1$ ) and ( $S_2 = k_B \ln G_2$ ) are the entropy of the crystal without and with vacancies respectively,  $k_B$  is Boltzmann's constant, and  $T$  is the absolute temperature.  $G$  is the probability to form  $n$  vacancies in  $N$  atoms, which equals to the probability of choosing  $n$  atoms out of  $N$  atoms (number of ways in which they can be arranged) and equals;

$$G_1 = \frac{N!}{N!} = 1, \quad G_2 = \frac{N(N-1) \dots (N-n+1)}{n!} = \frac{N!}{(N-n)!n!} \quad (2.2)$$

By applying Stirling's approximation, the complete entropy gain is equal;

$$\Delta S = k_B \ln \frac{N!}{(N-n)!n!} = k_B [N \ln N - (N-n) \ln (N-n) - n \ln n] \quad (2.3)$$

The change in the free enthalpy in thermal equilibrium is minimum and hence,

$$\Delta F = E_f - k_B T \ln \frac{N-n}{n} = 0 \quad (2.4)$$

In real crystals  $N \gg n$ , hence the number of vacancy equals [92];

$$n = N \cdot \exp\left(-\frac{E_f}{K_B T}\right); C_v = \frac{n}{N} = \exp\left(\frac{S}{K_B}\right) \cdot \exp\left(-\frac{E_f}{K_B T}\right) \quad (2.5)$$

From Eq. (2.5), the vacancy must exist in an ideal crystal at  $T > 0$  [15].

$$n = N \cdot \exp\left(-\frac{E_m}{K_B T}\right) \quad (2.6)$$

With increasing the temperature, the rate at which a point defect migrates from site to site in the crystal is increased and Eq. (2.5) becomes;

$E_m$  is the migration energy.

The equilibrium concentration of di-vacancies can be calculated in a similar manner. Suppose that  $Z$  is the coordination number of the lattice, so there are  $ZN/2$  adjacent pairs of lattice sites. Amongst these sites,  $n_2$  di-vacancies can be distributed in the following number of ways [93],

$$G_2 = \frac{(ZN/2)!}{(ZN/2 - n_2)! n_2!} \quad (2.7)$$

$$n_2 = \frac{1}{2} ZN \cdot \exp\left(-\frac{E_{f1v} - E_{f2v}}{K_B T}\right);$$

$$C_{2v} = \frac{1}{2} Z(C_v)^2 \cdot \exp\left(-\frac{E_{f1v} - E_{f2v}}{K_B T}\right). \quad (2.8)$$

Similarly, the energy required to remove one atom and insert it into an interstitial position is the formation energy of interstitials  $E_f^i$  and it is much higher than that of vacancies. In metals and under thermal equilibrium, the concentration of interstitials may be neglected in comparison with that of vacancies. In ionic bonding materials such  $K^+ Cl^-$  or  $Na^+ Cl^-$ , where the difference in size between the cation and the anion is small, the number of cations and anions vacancies (missing of  $K^+$  and  $Cl^-$  atoms) are equal due to conservation of the overall

neutral charge. This type of point defects is named as **Schottky** defect after the German scientist Schottky [94].

There is another type of point defect known as **Frenkel** defect, where an atom or ion moves from its original lattice site to an interstitial position; it occurs usually when the size of the anion is considerably larger than that of cation ( $Zn^{+} S^{-}$ ). Important to realize that the density of the crystal remains constant in contrast to Schottky defect, which decreases due to the vacancies as it is noticed from figure 2.2 [95].

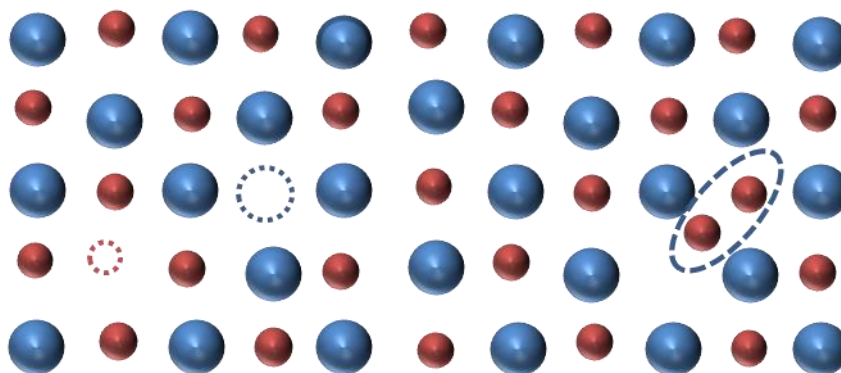


Figure 2.2: Schematic illustration of Schottky and Frenkel defects.

### 2.1.2 Linear defects (Dislocations)

Dislocations are lines in the crystal along which the atoms are out of position in the crystal structure. Dislocations are produced and displaced consequence to an applied stress. As a result of this motion, a glide- plastic deformation is emerged [96]. Dislocations may act as electrical defects in semiconductors (they are almost always undesirable); they participate in the crystal growth and in the structures of interfaces between crystals. Many endeavors have been done to proof the existence of dislocations. For instance, comparing the theoretical and the experimental values of the applied shear stress required to plastically deform a single crystal. Frenkel in 1926 was the first one, who calculated the applied shear stress on a perfect rectangular-type (figure 2.3 and 2.4) [90, 97]. Figure (2.3) shows atom positions used to calculate the theoretical critical shear stress for a slip. In order to displace the top atomic row, a periodic shearing force is needed. The shearing force is periodic, because the lattice resists the applied stress for the displacement  $x < b/2$  ( $b$  is the spacing of atoms in the shear direction) whereas the lattice forces assist the applied stress in case of  $x > b/2$  [98].

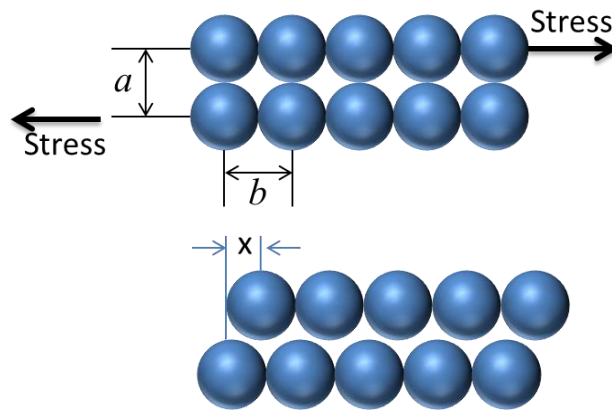


Figure 2.3: Slip of crystal planes,  $b$  the spacing between atoms in the direction of the shear stress,  $a$  the spacing of the rows of atoms and  $x$  is the displacement [99].

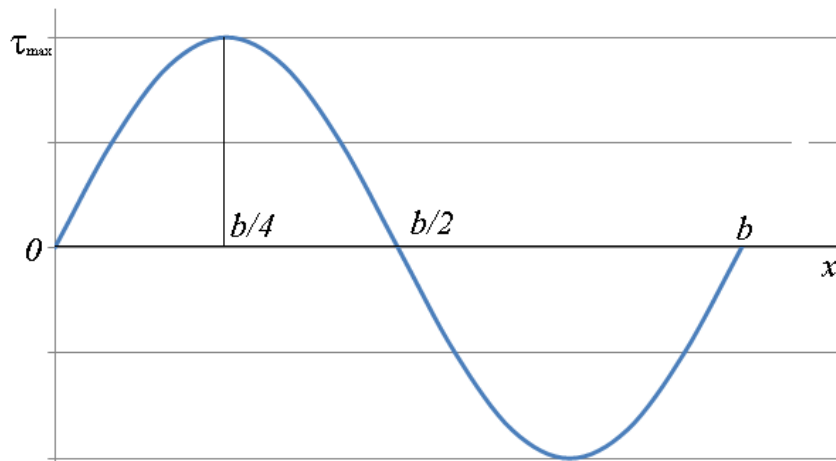


Figure 2.4: Shear stress versus displacement curve [100].

$$\tau_{sh} = \tau_{max} \sin(\omega x) = \tau_{max} \sin\left(\frac{2\pi x}{b}\right) \cong \tau_{max} \frac{2\pi x}{b} \quad (2.9)$$

$\tau_{sh}$  is the shear stress described by: Eq 2.9 where  $\tau_{max}$  is the theoretical critical shear stress at displacement  $b/4$  (figure 2.4). The shear modulus  $= \frac{\tau}{\tan \theta}$ , where  $\tan \theta$  is the elastic shear strain and given by  $x/a$  for small displacement, hence;  $\tau_{max} = \frac{G}{2\pi} \frac{b}{a}$ , taking into consideration that  $a \cong b$ , thus the maximum shear stress a sizeable fraction of the shear modulus,  $\tau_{max} = \frac{G}{2\pi} \cong G$  [98].

In 1930s, it has been possible to produce crystals with a high degree of perfection. The existence of dislocation referring to a line defects on the atomic scale was deduced independently by *Taylor, Polany, and Orowan*, could get strength of some fiber crystals close to the theoretical strength [101, 102, 103].

The presence of dislocations in the crystal is confirmed also when comparing the preferential deposition process between perfect and real crystals during crystal growth in a supersaturated vapor. According to the nucleation theory, approximately 50 % supersaturation degree would be required for the growth of the smooth faces (low degree of supersaturation is needed for irregular facets). However, this is found to be in contrary to the experiments, which showed that growth occurs at 1 % supersaturation. Dislocations generated during crystal growth could result in the formation of steps on the crystal faces, which are not removed by preferential deposition but also providing sites for deposition, which eliminates the difficult nucleation process [90]. Regardless of all these evidences, many metallurgists remained doubt about the dislocation theory until the development of the transmission electron microscope in the late 1950s [104].

### **2.1.2.1 Geometry of dislocations**

Figure 2.5(A) represents a front face of the atomic arrangement in a simple cubic crystal. Dislocations arise from adding an extra half plane (stretching the atomic bonds) or removing a half plane (compressing the atomic bonds) as illustrated in figure 2.5(B). As a result, an unstable configuration is formed, the distance or bonds between atoms doubled or halved. Finally, after relaxation of atoms, a new defect configuration is obtained (figure 2.5(c)). This type of defect is called *edge dislocation*. The extra half plane is abruptly ended, which creates the dislocation only at the bottom edge. Dislocations are considered as line defects not planar, since the suddenly ending of the extra half plane creates the defect, not the whole plane. It is clear from figure 2.5(c) that upward (and downward) the dislocation, a normal plane, not an extra half plane (no missing half plane) is found, since the atoms are allowed to come to equilibrium. The orange line in figure 2.5(c) (points into the drawing plane) represents the dislocation line and the edge dislocation is positive. On the other hand, inserting the extra plane of atoms from below, a negative edge dislocation is obtained, (see figure 2.5(D)) [105]. Edge dislocations introduce compressive, tensile, and shear lattice strains.

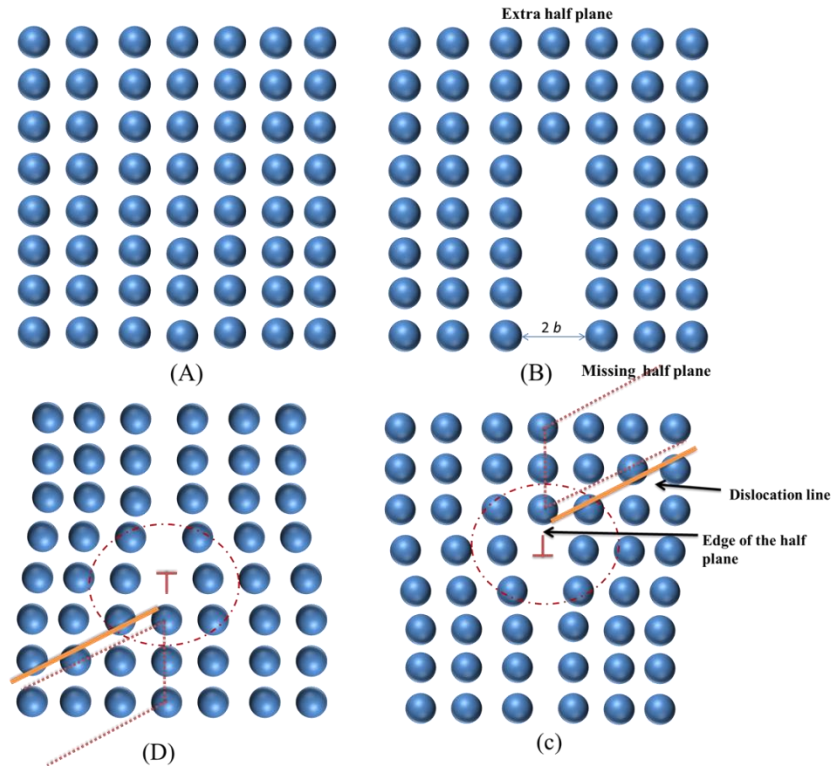


Figure 2.5: Schematic description of the edge dislocation (the atomic bonding is not drawn here).

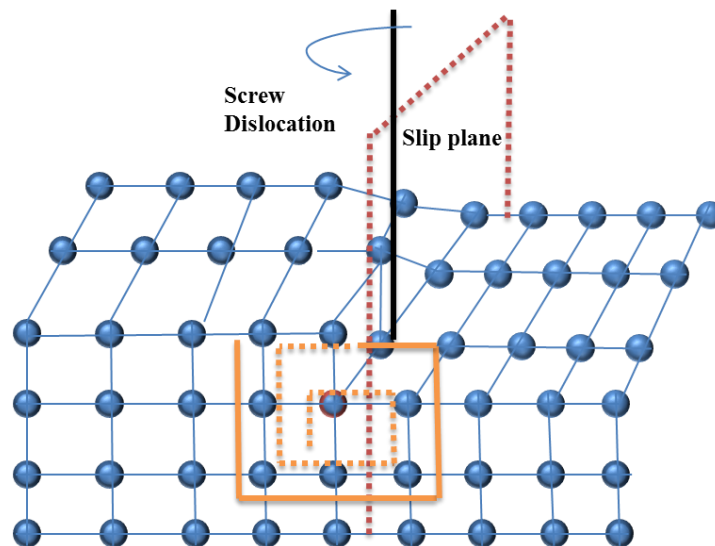


Figure 2.6: Schematic description of the left-handed screw dislocation.

The second type of dislocations is a *screw dislocation*, where the atoms are displaced in two separate planes perpendicular to each other forming a spiral tilt around the dislocation as it

illustrated in figure (2.6). Screw dislocations introduce shear strain only. However, dislocations are never pure “edge” or “screw” type, they are usually mixed.

### 2.1.2.2 Dislocation motion

Plastic deformation (applied stress) is the reason for the net movement of large numbers of atoms. During this process, interatomic bonds must be broken and then remade. In crystalline solids, plastic deformation most often involves the motion of a large number of dislocations. This motion is called a slip, thus, the material strength can be improved by putting obstacles to slip [106]. Figure 2.7 (up) shows that an edge dislocation moves in response to shear stress applied in the direction perpendicular to its line during plastic deformation. It is analogous to the motion of a caterpillar or a carpet over a floor; forming a hump or a ruck corresponds to the motion of extra half-plane of atoms.

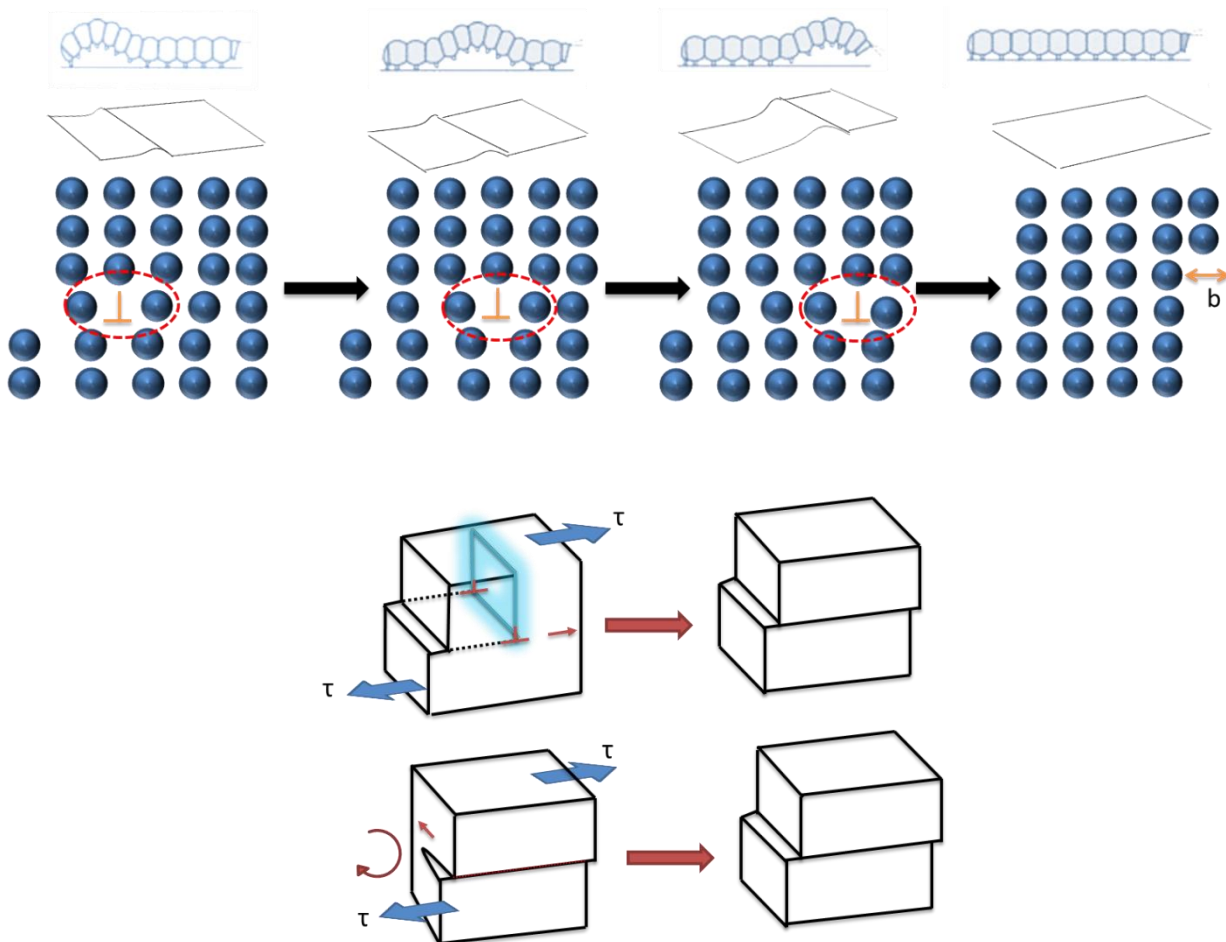


Figure 2.7: Dislocation movement during plastic deformation [107, 108].

Dislocations cannot end within the lattice, only if they meet external free surfaces, internal grain boundaries, other dislocations forming a node or they can end on themselves forming a



loop. When dislocations (opposite of each other) are brought together in the same plane, they annihilate and restore the perfect crystal.

**Prismatic dislocation loop**

It is known that dislocations can end on themselves forming a loop. Consider a slip plane and contains a closed loop (dislocation lines, figure 2.8), the tangent vector changes from point to another through this loop. Let's consider that the Burger vector, which shows how much the entire region is slipped relative to the un-slipped one, pointing up and since it is constant, different types of dislocations will be obtained.

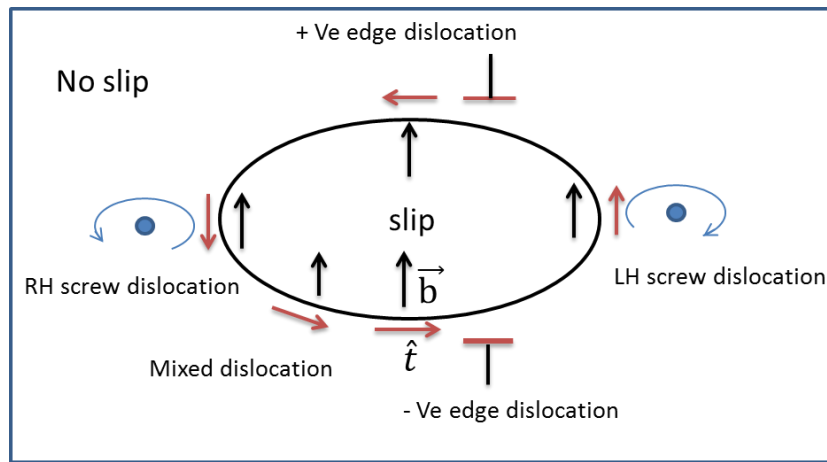


Figure 2.8: Dislocation loop [109].

The Only plane which contains the Burger ( $\vec{b}$ ) and linear vector ( $\hat{t}$ ) is the surface of a cylinder (surface of a prism) and dislocation line is its base (see figure 2.9).

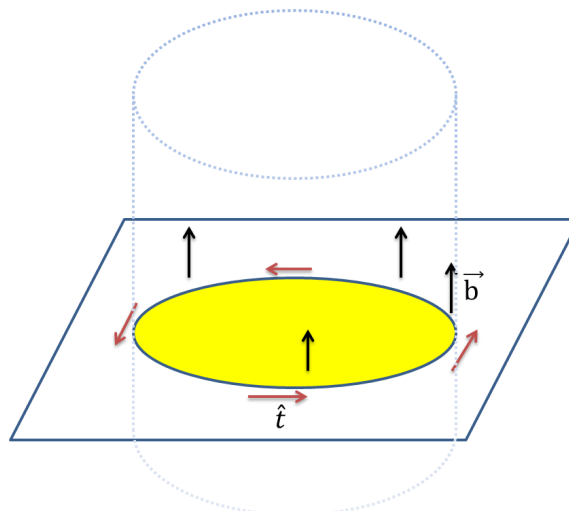


Figure 2.9: Schematic illustration of a prismatic dislocation loop [109].

The vacancy loop (condensation of vacancies) in a closed-packed plane behaves exactly like a prismatic loop with only an edge dislocation (figure 2.10).

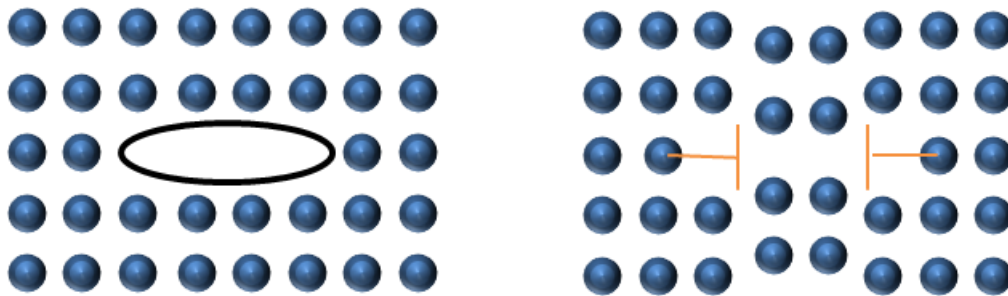


Figure 2.10: Vacancy loop acts as a prismatic dislocation [109].

### 2.1.3 Bulk (volume) defects

Volume defects are 3-dimensions defects, which are normally introduced during fabrication steps. These include pores, cracks, foreign inclusions, precipitations and voids based on a combination of the size and effect of the particle. In some cases, foreign particles are added purposefully to strengthen the parent material [110]. The procedure is called precipitation hardening where foreign particles act as barriers to the movement of dislocations. Inclusions are undesirable particles that entered the system as dirt or formed by precipitation. Voids are holes in the solid formed by trapped gases (it is commonly called porous) or by the accumulation of vacancies. When a void occurs due to the shrinkage of a material as it solidifies, it is called cavitation [111].

### 2.1.4 Planar (Interfacial) defects

Planar defects are boundaries that have two-dimensional imperfections such as grain boundaries, twin boundaries, and stacking faults. These imperfections are meta-stable and arise from the clustering of line defects into a plane [110, 112].

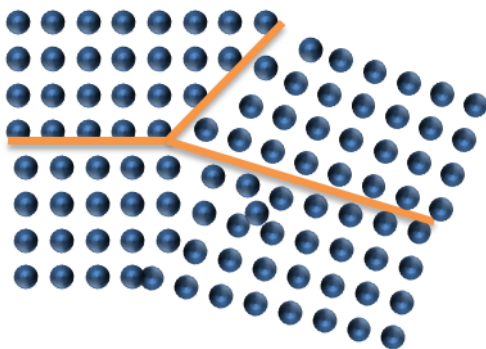


Figure 2.11: Schematic presentation of the grain boundaries [110, 112]

Grain boundaries are the boundaries which separate the grains due to a mismatch of the orientation of grains because of the dislocations as shown in figure 2.15. On the other hand, any change in the stacking sequence of the crystal causes an imperfection. The fault in the stacking sequence leads to a stacking fault, but when the change in the sequence is a mirror image, in this case a twin boundary is formed (figure 2.16) [110].

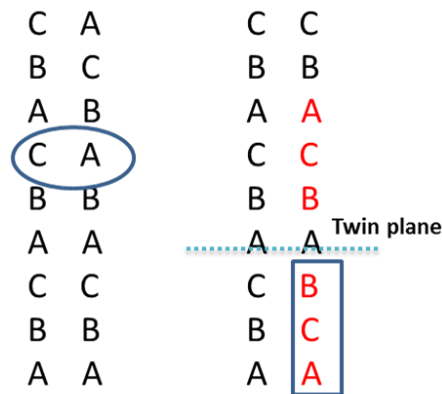


Figure 2.12: Schematic presentation of twin boundaries and stacking fault

## 2.2 Diffusion

### 2.2.1 Introduction

Controlling the microstructure, which determines many of the physical and all of the mechanical properties of the material, is a matter of interest in material science. The microstructure is controlled by the phase transformation, which involves the diffusion process [113]. Many microstructure changes in solid happen through diffusion, i.e. mass transfer (atoms) in solid phases. The existence of defects, e.g. vacancies, interstitial, dislocations and grain boundaries are responsible for diffusion [114, 115]. Diffusion is always important for processes at an elevated temperature such as; ordering and disordering processes in alloys (formation of precipitations, defect annealing after plastic deformation) [15]. Similarly to Fourier's and Ohm's laws, which explain the heat and charge flow respectively, the mass flow is governed by Fick's laws [116].

### 2.2.2 Fick's first law of diffusion

In 1855 formulated *Adolph Fick* [116] an equation in order to describe the flow of mass (particles or moles) from high to low concentrations. This means that the mass flux  $j$  ( $\text{Kg m}^{-2} \text{s}^{-1}$ ) is driven by the concentration ( $\text{Kg m}^{-3}$  or  $\text{mol m}^{-3}$ ) gradient  $-\frac{dC}{dX}$  and hence;

$$j = -D \frac{dC}{dx} \quad (2.10)$$

$D$  ( $\text{m}^2 \text{s}^{-1}$ ) is the diffusivity or diffusion coefficient and its typical value in solids:  $10^{-9}$  to  $10^{-24}$   $\text{m}^2 \text{s}^{-1}$ .

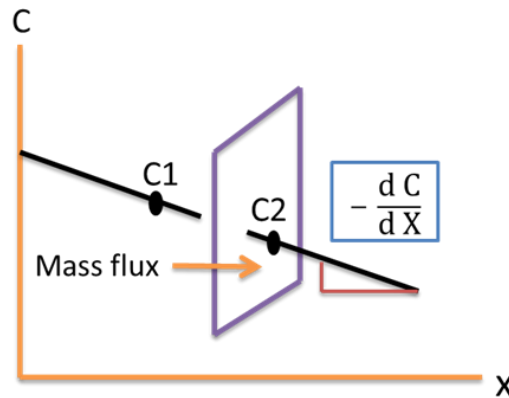


Figure 2.13: Schematic illustration of Fick's first law. The concentration  $C1 > C2$  so mass flux will move from high to low concentration [115].

The diffusion coefficient is strongly temperature dependent;

$$D = D_0 \exp \left( \frac{-Q}{k_B T} \right) \quad (2.11)$$

$Q$  is the activation enthalpy of diffusion,  $k_B$  is the Boltzmann constant, and  $T$  is the absolute temperature. The pre-exponential factor  $D_0$  can be written as:

$$D_0 = D_o \exp \left( \frac{\Delta S}{k_B T} \right) \quad (2.12)$$

$\Delta S$  is the diffusion entropy and  $D_o$  is the geometry factor. For example, one atomic distance at  $RT$  in self-diffusion Au takes  $10^{-10}$  m/day, since diffusion coefficient equals  $10^{-24}$   $\text{m}^2 \text{s}^{-1}$ .

### 2.2.3 Fick's second law of diffusion

Fick's first law assumes a fixed concentration gradient. In case of the concentration gradient changes with time, Fick's second law is used. It can be easily derived on the basis of mass conservation. By assuming a bar containing diffused particles (the concentration of the

diffused particles is high in one end and gradually decreasing up to the other end (figure 2.15). The concentration gradient is different between the two positions ( $x$  and  $x+\Delta x$ ).

The flux at  $x$  is  $j_x$ , which moves the mass into the volume  $\Delta v$ , and at  $x+\Delta x$  is  $j_{x+\Delta x}$ , which move the mass out from the volume [105].

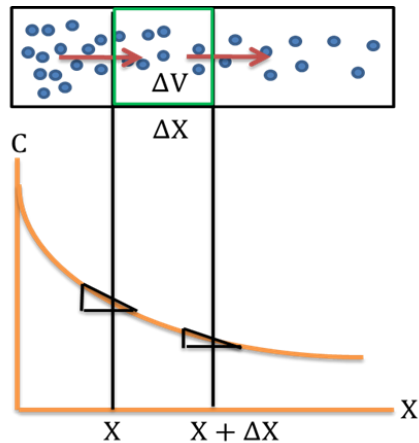


Figure 2.14: Change of the concentration gradient with time [115].

Fick's second law of diffusion is [105, 115, 117],

$$\frac{\partial C}{\partial t} = D \frac{\partial^2 j}{\partial x^2} \quad (2.13)$$

A special solution of the diffusion equation can be found in [118].

## 2.2.4 Atomic diffusion Mechanisms

### 2.2.4.1 Substitutional diffusion mechanism

Presence of some vacant sites in the crystal facilitates the diffusion process, as an atom can jump into the neighboring vacancy (figure 2.16). Self-diffusion in metals and alloys, in many ionic crystals and also in ceramic materials often occurs via vacancy mechanism [117].

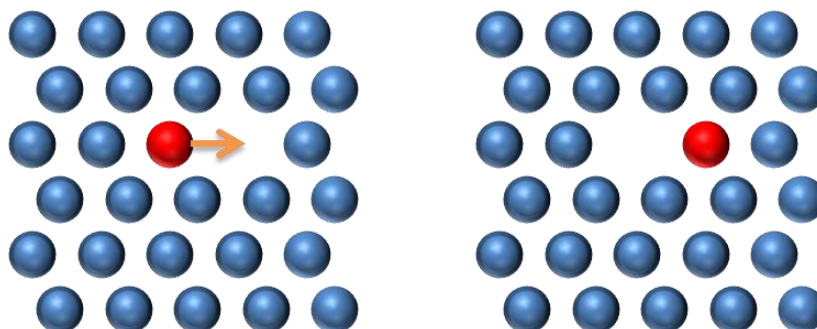


Figure 2.15: Single vacancy mechanism of diffusion [117].

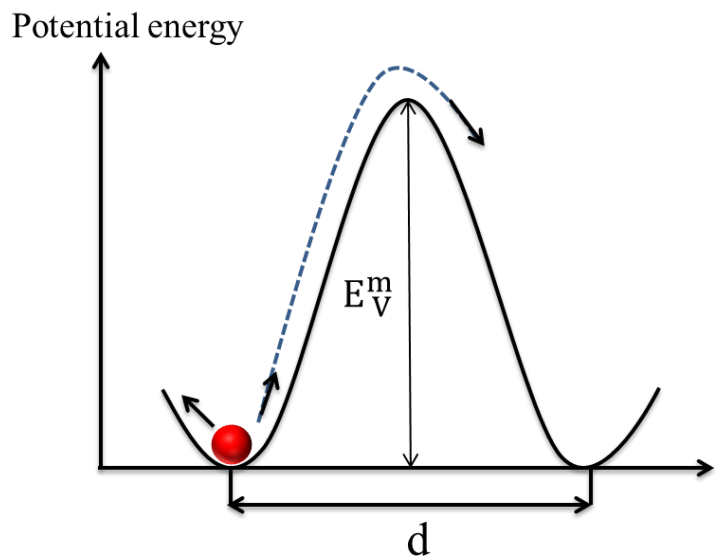


Figure 2.16: Schematic illustration of potential energy of an atom jumps into a vacancy [115].

On the other hand, the number of di-vacancies becomes quite large at higher temperature; hence the single vacancies mechanism is accompanied by divacancy mechanism (figure 2.18). However, single vacancy mechanism dominants below  $2/3 T_m$  [117].

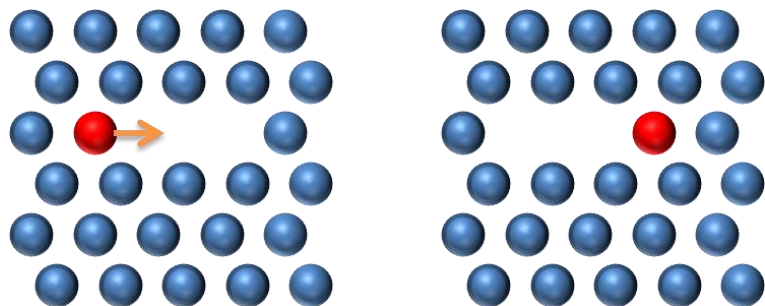


Figure 2.17: Divacancy mechanism of diffusion [117].

### 2.2.4.2 Interstitial diffusion mechanism

It is a diffusion of solute in an interstitial solid solution. An atom jumps from one interstitial to a neighboring interstitial site (figure 2.23).

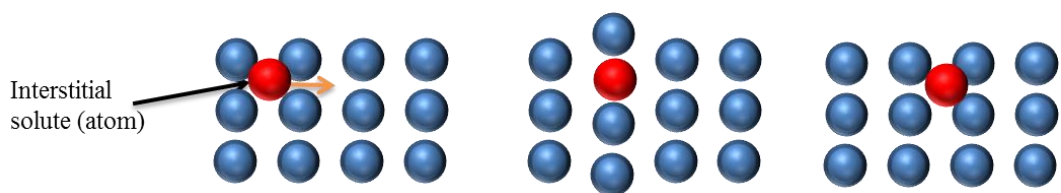


Figure 2.18: Interstitial diffusion mechanism [117].

Interstitial diffusion is generally faster than substitutional diffusion since the probability of finding a neighboring vacant interstitial is much higher than that of a neighboring vacancy, interstitial diffusion is often activated at very low temperature,  $E_V^m \gg E_i^m$  [117].

### 2.2.4.3 Frank-Turnbull (dissociative) mechanism

An impurity atom gets trapped in a vacancy, whereupon it is almost immobile. The atom starts from a regular lattice site then moves to an interstitial position, and diffuses as an interstitial but relatively fast.

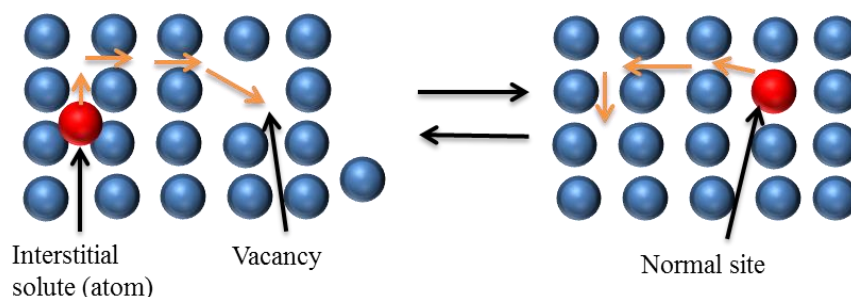


Figure 2.19: Frank-Turnbull mechanism [117].

### 2.2.4.4 Kick-out mechanism

Interstitial impurity atom moves (rather fast) by a direct interstitial mechanism until they finally kick out a lattice atom from its site which itself starts interstitial diffusion.

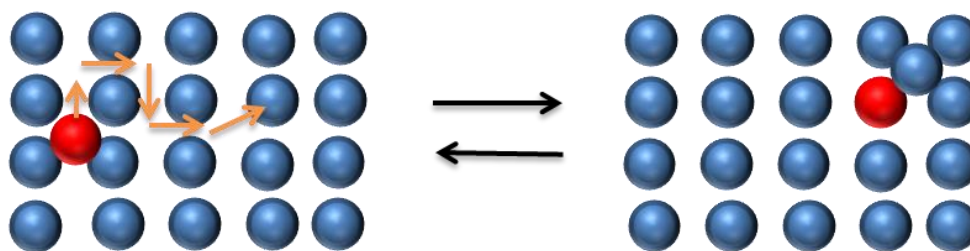


Figure 2.20: Kick-out mechanism [117].

# Chapter 3 : Phase transformation and precipitation hardening

## 3.1 Introduction

Phases are formed from the alloying elements in the alloy; their size and shape have a significant effect on the metal properties. In order to change the phases in an alloy, heat treatment is needed. Forming phases from a different phase is called a phase transformation. There are different kinds of phase transformation such as; eutectoid and precipitation. In both transformations, atoms move through the metal to rearrange themselves forming the new phase. At the eutectoid transformation (as in Steel), a single phase transfers into two other phases through cooling from an elevated temperature. However, particles of one phase (precipitates) are formed within the origin phase in case of precipitation transformations. The alloy is heated to elevated temperature so that a solid solution phase of the matrix and the alloying elements can form. This heating is followed by fast cooling to avoid the coarsening of the precipitates [119]. We can control transformation (and in turn control the size, shape and orientation of the precipitation) by controlling heating temperature, heating time, and cooling rate, which will have a big influence on the properties of the metal [119].

## 3.2 Phase diagram

Phase diagram is a diagram in the space of relevant thermodynamic variables (such as temperature and composition) indicating phases in equilibrium [120, 121]. The phase is a part of a system, which is chemically homogeneous, physically distinct, and mechanically can be separated. For instance, the solid phases of iron are Body Centered Cubic (phase  $\alpha$ ) and cubic centered packing (phase  $\gamma$ ). The components of a phase are the independent chemically species (element, compound) in terms of which the composition of a system is specified [122].

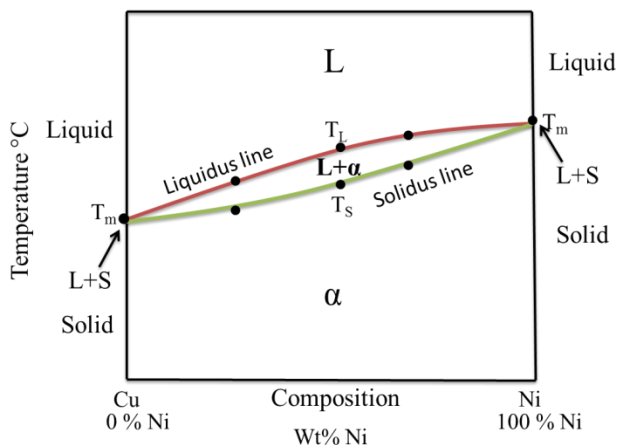


Figure 3.1: Cu-Ni binary phase diagram, L for liquid, S for solid and  $\alpha$  is the substitutional solid solution [120].



Figure (3.1) shows the binary phase diagram of Cu-Ni with complete miscibility. It is noticed that the entire melting for a pure metal happens at a fixed temperature ( $T_m$ ) and the solid phase is still converting to liquid phase after  $T_m$  due to the latent heat. Contrary to the pure metal, the alloy melts over a range of temperatures [122].

### 3.2.1 Gibb's phase rule

Gibb's phase rule (named after *Josiah Willard Gibbs* [123]) gives the number of intensive variables (not dependent on quantity such  $P$ ,  $T$ ) to determine the state of a system [124].

$$F = n - P + 2 \quad (3.1)$$

$F$  is the number of intensive variables that has to be defined (degrees of freedom),  $n$  is the number of components, and  $P$  is the number of phases [125, 126]. However, Gibb's phase rule for metallic Alloys is given by;

$$F = n - P + 1 \quad (3.2)$$

Since melting and boiling point of metals operates usually at constant pressure (atmospheric pressure).

By looking to figure 3.1, the pure metal at the melting point has  $F = 0$ , since  $n = 1$  and  $P = 2$ . At this point, the solid and the liquid are in equilibrium. On the other hand,  $F=1$  for the binary alloy (two phases and two components), which means that one intensive variable needs to be defined to figure out the state of the system (in this case the variable is the composition  $C$ ).

### 3.2.2 Phase present in a system

Consider a constitution point A in a binary phase diagram at 60 wt% Ni (figure 3.2). When the alloy is heated to a temperature  $T_1$ , the present phase will be  $\alpha$  with 60 wt% Ni or 40 wt% Cu. On the other hand, for a constitutional point B, which lays at 40 wt% Ni, if the alloy is heated to  $T_2$  and hold in equilibrium, the Present phase will be mixture of liquid and alpha (two phases are obtained). Generally, for a binary phase diagram moving horizontally along an isotherm from one single phase to another, a two-phase region mixture from both phases is formed [105].

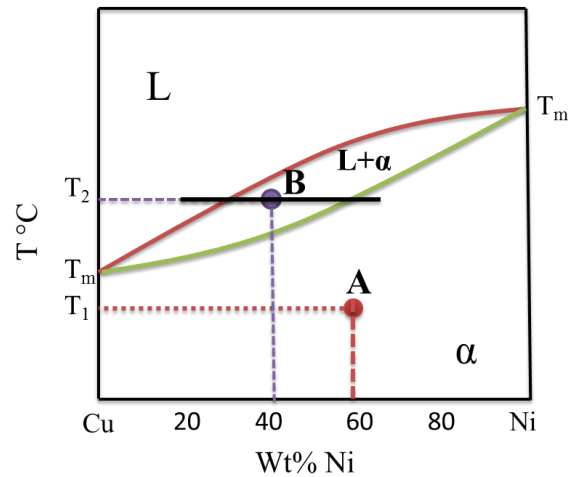


Figure 3.2: Phase present in a system [105].

### Composition of phase present in a system

The composition is the fraction or percentage of different components either in weight% or atom%. For a single phase, the alloy composition  $C_0$  equals the phase composition. While in the two phases region, the composition of the phases is calculated by drawing a tie line, which is an isotherm running from one boundary to the other (figure 3.3).

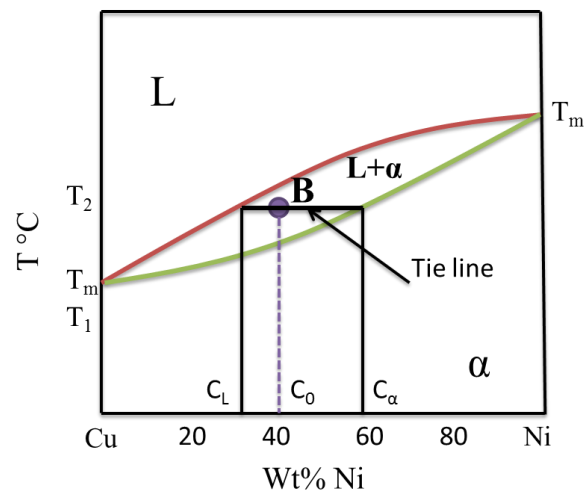


Figure 3.3: Composition of phase present in a system [105].

Consider a constitution point A (figure 3.4); the alloy composition  $C_0$  equals the phase composition  $C_\alpha$  (single phase), and the fraction of  $\alpha$  phase in the whole alloy is  $f_\alpha = 1$  or 100%. However, in two phase region, i.e. point B, the fraction of both phases is calculated by the lever Rule [127].

$$f_{\alpha} = \frac{c_0 - c_L}{c_{\alpha} - c_L}; \quad f_L = 1 - f_{\alpha} \quad (3.3)$$

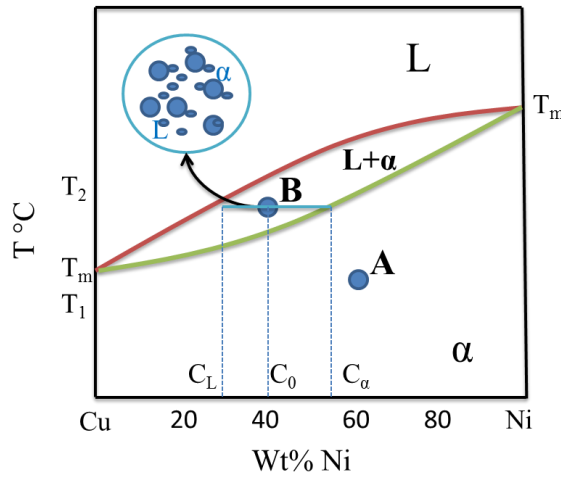


Figure 3.4: Relative amounts of phases present in a system.

### 3.3 Diffusive phase transformation

Transformation from phase to another needs a thermodynamic driving force, which is the difference in free energies between the two phases. For example, when a liquid phase transfer to a solid  $\alpha$  phase, the transformation is thermodynamically feasible if the free energy of  $\alpha$  is lower than of liquid;  $\Delta G = G_{\alpha} - G_L$ . It is shown from figure 3.5 that the melting temperature is a critical temperature for transferring between the two phases, i.e. liquid can transfer to solid below  $T_m$ . Diffusive phase transformation occurs through two processes; first one is a precipitation transformation, which involves the formation of a new phase (Nucleus) and this is called Nucleation. Further increase in the size of the Nucleus is called growth (figure 3.6 ). The second process is a continuous transformation (a spinodal decomposition ).

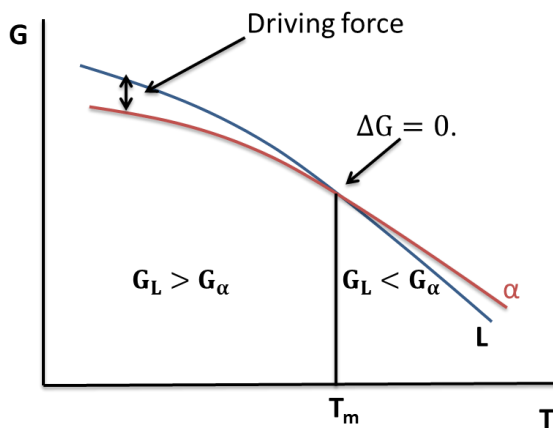


Figure 3.5: Driving force of phase transformation [105].

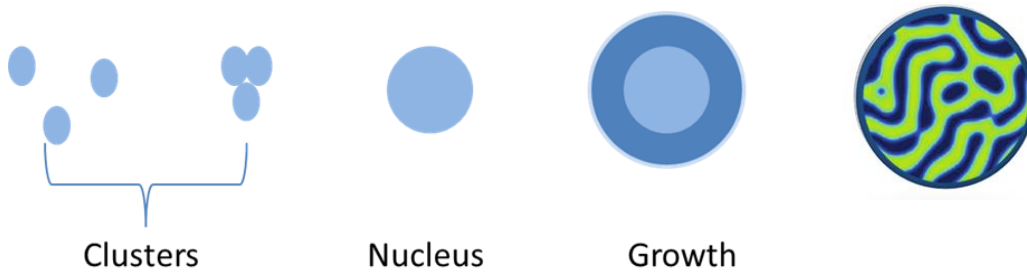


Figure 3.6: Schematic illustration of nucleation, growth, and spinodal decomposition [128].

### 3.3.1 Nucleation

Nucleation occurs when a small nucleus begins to form in the liquid. The nuclei then grow as soon as atoms from the liquid attach to it (figure 3.7). Nucleation can be homogeneous or heterogeneous depending on the presence of foreign particles (defects) in the liquid. Homogeneous nucleation takes place spontaneously and haphazardly without favorable nucleation site. While, heterogeneous Nucleation occurs at preferential sites such as grain boundaries, dislocations or impurities [129].

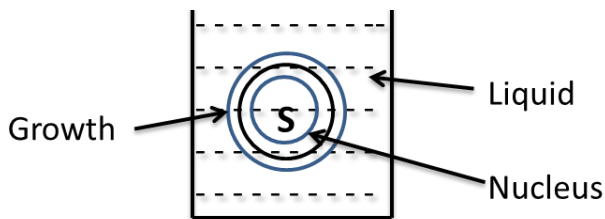


Figure 3.7: Schematic description of the solidification process (nucleation and growth), S represents solid.

#### 3.3.1.1 Homogeneous Nucleation

Homogeneous nucleation takes place spontaneously without any aid from any surfaces or defects. Consider a solidification process; a solid ball S of radius  $r$  nucleates in an unstable liquid L. In reality, the liquid can be kept undercooling in a metastable form, and hence a solid/liquid interface is formed with the solid sphere (figure 3.8).

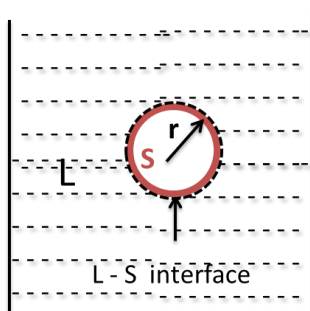


Figure 3.8: solid/liquid interface.

Assume that there is no change in volume ( $\rho_S = \rho_L$ ). The change in Gibb's free energy  $\Delta G_{Hom}$  is calculated as:

$$\Delta G_{Hom} = \underbrace{\frac{4}{3}\pi r^3(G_S - G_L)}_{\text{volume free energy}} + \underbrace{4\pi r^2\gamma}_{\text{interfacial or surface energy}} \quad (3.4)$$

where  $G_S$  &  $G_L$  are the Gibb's free energies per unit volume of solid (which is added to the system), and of liquid (which is subtracted from the system), respectively.  $\gamma$  is the energy per unit area of the solid/liquid interface. In case of  $T < T_m$ , the volume free energy is negative, since  $G_S < G_L$  (see figure 3.5). Figure 3.9 represents the Gibb's free energy as a function of the nuclei radius. It is obvious that the change in the free energy reaches a maximum value at a critical radius  $r^*$ . The nuclei with radii lower than  $r^*$  will not grow since  $\Delta G_{Hom}$  is high. In contrast to the nuclei with radii higher than  $r^*$ ,  $\Delta G_{Hom}$  decreases and this is thermodynamically favorable for the growth [124, 130].

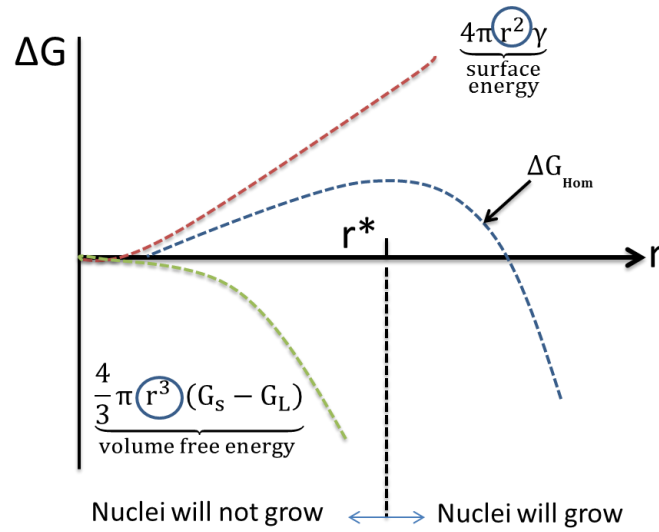


Figure 3.9: Total free energy vs nucleus radius [124, 131, 132].

The energetic barrier needs to be surpassed to achieve nucleation ( $\Delta G^*_{Hom}$ ) is given by;

$$\frac{\partial \Delta G^*}{\partial r} \Big|_{r=r^*} = 0 \quad (3.5)$$

After differentiation, the critical radius for nucleation equals;

$$r^* = \frac{-2\gamma}{G_S - G_L} \quad (3.6)$$

The numerator  $\gamma$  increases the free energy and that acts as an obstacle to nucleation, contrary to the denominator  $G_s - G_L$ , which represents the driving force;

$$G_s - G_L = \frac{\Delta H \Delta T}{T_m}, \quad (3.7)$$

where  $\Delta H$  is the latent heat of fusion. The critical radius equals,

$$r^* = \frac{-2\gamma T_m}{\Delta H \Delta T} \quad (3.8)$$

### 3.3.1.2 Heterogeneous Nucleation

In case of heterogeneous nucleation, the phase transformation takes place with the help of some surfaces such as container wall, grain boundaries, or some other defects. In order to promote the heterogeneous nucleation and growth; a nucleation agent or an inoculants are added to the molten metal (act as a catalyst).

The nucleation as shown before depends on the surface energy, which in turns depends on the wetting or contact angle  $\theta$  [124, 132, 133]. In case of metal solidifies on a foreign substrate, the substrate should be wet by liquid metal.

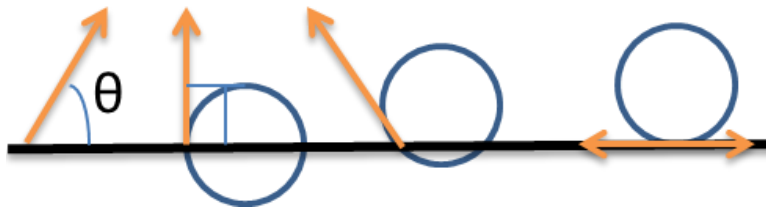


Figure 3.10: The wetting angle  $\theta$  [134].

In order to calculate the critical radius  $r^*$ ; consider a solid phase ( $\beta$ ) is formed in a liquid phase (L) on a foreign substrate (container wall (M)).The new phase nucleates as a spherical cap nucleus (see figure 3.11).

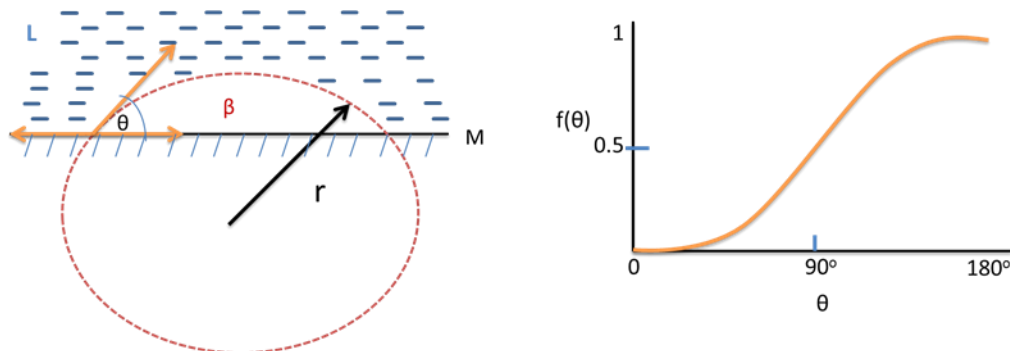


Figure 3.11: Schematic of heterogeneous nucleation mechanism; spherical cap of solid phase in liquid on a substrate [135].

As we have three surfaces, a three interfaces are presented; liquid –substrate interface ( $\gamma_{LM}$ ), liquid –solid interface ( $\gamma_{L\beta}$ ), and solid-substrate interface ( $\gamma_{\beta M}$ ), which;

$$\gamma_{LM} = \gamma_{\beta M} + \gamma_{L\beta} \cos \theta \quad (3.9)$$

The change in Gibb’s free energy  $\Delta G_{Hetr}$  is calculated as:

$$\Delta G_{Hetr} = f(\theta) \Delta G_{Hom} = f(\theta) \underbrace{(V_{\beta}(G_{\beta} - G_L))}_{\text{volume free energy}} + \underbrace{(A_{L\beta}\gamma_{L\beta} + A_{\beta M}\gamma_{\beta M})}_{\text{interfacial or surface energy}} \quad (3.10)$$

However, before nucleation the interface of solid and substrate  $\beta M$  was between liquid and substrate LM, so a surface energy  $A_{LM} \gamma_{LM}$  should be subtracted from Eq. (3.10). This term in addition to the volume free energy act as a driving force of nucleation;

$$\Delta G_{Hetr} = f(\theta) \underbrace{(V_{\beta}(G_{\beta} - G_L))}_{\text{volume free energy}} + \underbrace{(A_{L\beta}\gamma_{L\beta} + A_{\beta M}\gamma_{\beta M} - A_{\beta M}\gamma_{LM})}_{\text{interfacial or surface energy}} \quad (3.11)$$

Where  $A_{LM} = A_{\beta M}$  and  $V_{\beta} = \frac{4}{3}\pi r^3 f(\theta)$ ,  $A_{L\beta} = 4\pi r^2 \frac{1-\cos\theta}{2}$  and  $A_{\beta M} = \pi r^2 (1 - \cos^2\theta)$

Similarly to the homogenous nucleation, the energetic barrier needs to be surpassed to achieve nucleation ( $\Delta G^*_{Hetr}$ ) and the critical radius are given by;

$$\frac{\partial \Delta G^*_{Hetr}}{\partial r} \Big|_{r=r^*_{Hetr}} = 0, \quad r^*_{Hetr} = \frac{-2\gamma_{L\beta}}{G_{\beta} - G_L} \quad (3.12)$$

this is the same value of  $r^*_{Hom}$  in Eq. (3.6). However,  $V^*_{Hetr} = V^*_{Hom} f(\theta)$  &  $\Delta G^*_{Hetr} = \Delta G^*_{Hom} f(\theta)$ , therefore for smaller contact angles  $\theta$ , the heterogeneous nucleation is preferable over the homogenous nucleation (figure 3.12).

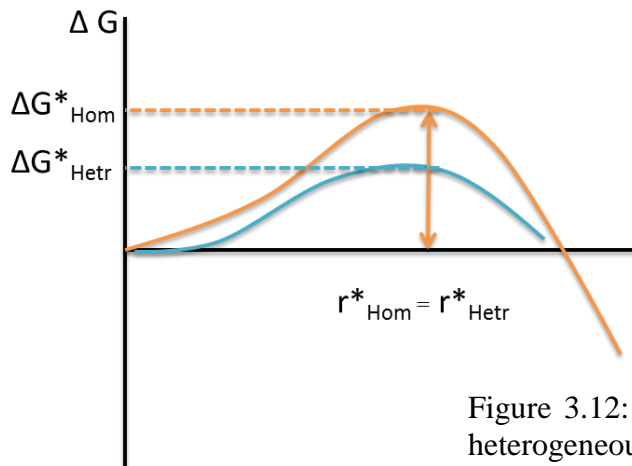


Figure 3.12: Total free energy for homogenous and heterogeneous nucleation [136]

In the precipitation transformation  $\alpha_{\text{origin}} \rightarrow \alpha_{\text{final}} + \beta$ , the new phase will still have the structure of the origin phase even if the composition is changed. The formation of the new phase (precipitate,  $\beta$  in this example) adds a distortion or strain energy. In case of the formation of a new phase in an imperfection sites, this strain energy varies with the shape of the precipitate [92]. Consider an ellipsoid with equator diameter and polar axis  $c$  and  $a$ , respectively. Different shape factors ( $c/a$ ) lead to different shapes of precipitations (figure 3.13) [132].

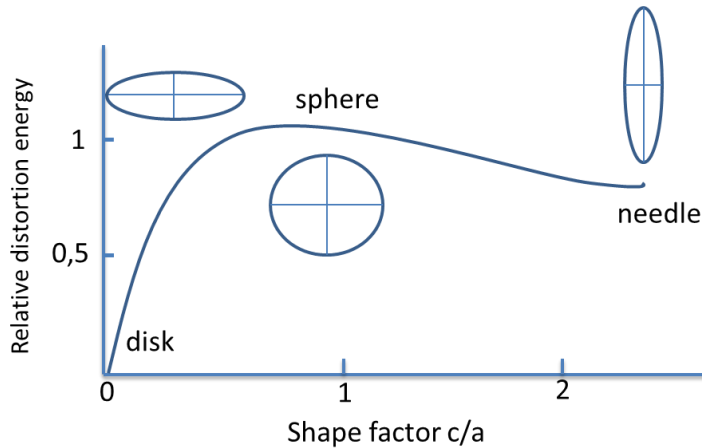


Figure 3.13: Strain energy as a function of precipitate shape [92, 132].

### 3.3.1.3 Nucleation and growth rate

The overall transformation rate ( $\frac{dx}{dt}$ ,  $s^{-1}$ ) depends upon the nucleation and growth. Figure 3.14 shows that nucleation and growth happen at a time interval. The nucleation rate ( $I$ ,  $m^{-3}s^{-1}$ ) is the number of nucleation events per unit volume per second. The rate of increase the size of growing nuclei ( $R$ ) per second is the growth rate ( $\frac{dR}{dt}$ ,  $ms^{-1}$ ) [124].

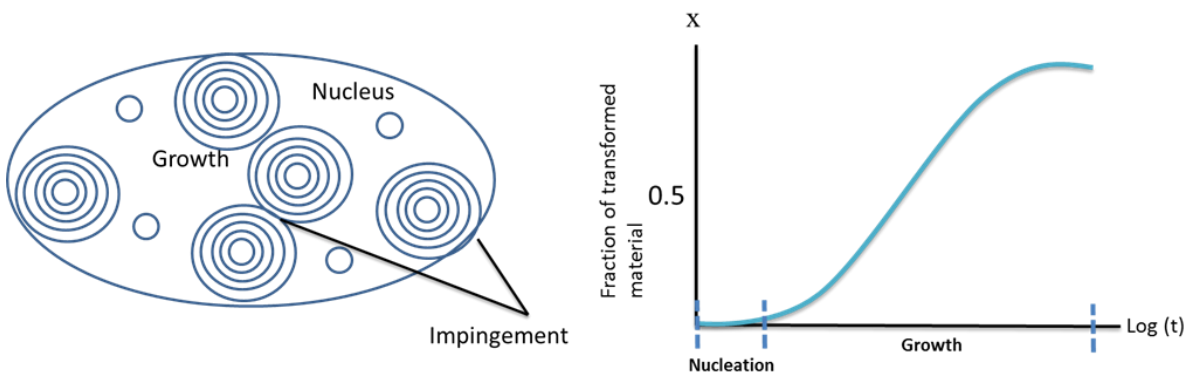


Figure 3.14: The overall transformation rate [124].



The transformation rate starts slowly at the beginning (due to small number of nuclei) and ends slowly also because of the volume reduction (due to impingement). The three rates depend on the temperature; they reach the maximum at a specific T. Figure 3.15 shows that at  $T_m$  and  $T=0$ , there is no nucleation (due to zero driving force and reduction of atomic mobility).

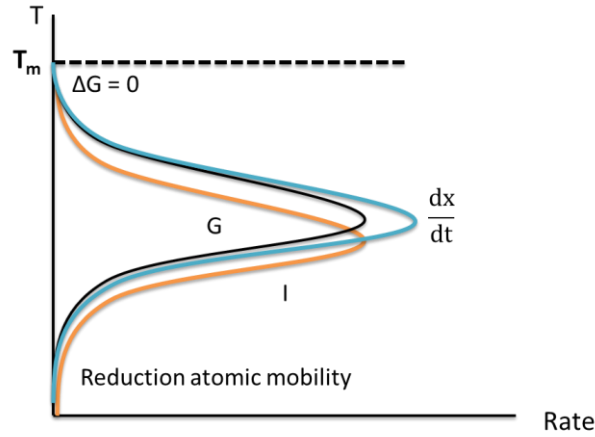


Figure 3.15: Temperature dependence of the transformation rates [124].

Rate of homogeneous nucleation for a given undercooling is [137],

$$I = I_0 \exp\left(-\frac{\Delta G_{Hom}^*}{KT}\right) \text{ clusters}/m^3 \quad (3.13)$$

$I_0$  is the atoms per unit volume in the liquid,  $C^*$  is the number of atoms that have reached critical size.

Rate of heterogeneous nucleation is [138],

$$I^* = I_1 \exp\left(-\frac{\Delta G_{Hetr}^*}{KT}\right) \text{ nuclei}/m^3 \quad (3.14)$$

$I_1$  is the number of atoms in contact with the heterogeneous nucleation sites.

### 3.3.2 Spinodal decomposition

In the classical nucleation and growth, the growth is controlled by the diffusion in which atoms diffuse from the original phase across the phase boundary (a barrier has to be overcome), and then into the second phase.



### **3.4 Strengthening of aluminum**

Strength is the ability of a material to withstand an applied stress until it breaks. It determines whether the material can be used for specific applications [141]. Strength depends on the stress type and duration as well as the temperature. Tensile, bending, fatigue, and compressive are various types of strength depending on the type of the applied stress. Tensile strength is the most important one; it is determined using a tensile testing machine. The maximum tensile stress (expressed in Newton per mm<sup>2</sup>) is the maximum duration that the test piece can withstand without failure [141]. Most pure metals are ductile however, alloying or heat treatments lead to an increase in the strength [141].

Pure aluminum is soft (not ideal for building strong structures.) and, thus easily deformed. Deformation results from the presence of defects in the crystal lattice – so-called ‘dislocations’. When a force is applied to a metal, these dislocations can move along special slip planes, causing the metal to deform [142-145]. If dislocations are prevented from moving in this way, there will be an increase in the strength of the material (hardness and stability). Dislocations may be pinned with other dislocations and solute particles due to stress field interactions.

There are four main strengthening mechanisms for metals; work (cold/Strain), grain boundary, solid-Solution, and precipitation (Age) hardening. Each of them make it energetically unfavorable for the dislocation to move [146, 147]. We are here focusing in the precipitation hardening.

#### **3.4.1 Precipitation (Age) hardening**

##### **3.4.1.1 History**

In precipitation hardening, precipitate particles are produced within the metal matrix to obstacle the dislocations motion. The formation of precipitates required rapid cooling (quenching) after solution heat treatment at higher temperatures. The solution heat treatment of an alloy forms a single stable phase (however still has very small amount of the solute atoms), while fast cooling or quenching is required in order to prevent the creation of lattice defects [148]. Age hardening of aluminum was discovered accidentally by *Alfred Wilm* [149] during the years 1901 -1911 [150]. Similar to steel, which hardens by quenching, Wilm was trying to quench Al alloys and measure the hardness. He started to heat several Al –Cu alloys (Al- 3.5-5.5 wt%Cu-Mg-Mn, Mg and Mn were < 1%), hold them for some time, quench, and then directly measure the hardness (figure 3.17 left).

After several attempts such as varying the holding time and the quenching rate, he could not improve the alloys hardness. The hardness of the alloys increases incidentally with Wilm when he quenched the alloy and wait for some time then measure the hardness (from here came the name of ageing) [105]. Natural-ageing is the process of age-hardening by holding the quenched alloy at room temperature. Although the hardness increases with time, after a certain time it starts to decrease and overageing occurs without any change in the microstructure. Wilm examined his samples in an optical microscope but he was unable to detect any structural change as the hardness changes (figure 3.17).

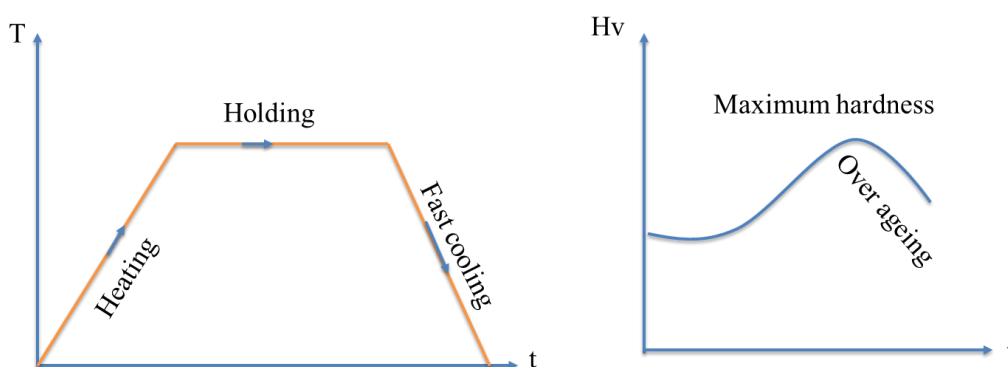


Figure 3.17: Heat treatment and hardness of Al-4wt%Cu alloys according to Wilm [105].

In 1919, *Mercia, Waltenberg and Scott* [151] found that with decreasing the temperature, the solubility of Cu atoms in Al-matrix decreases. They attributed that to precipitate out of Cu from supersaturation solid solution phase [152]. *Mercia et al* [153] suggested in 1932 that Cu atoms gather in small clusters (“knots”) when the grains of an alloy are deformed. The knots in turn interfere with dislocations resulting in age hardening [154]. *Mercia* suggestion had no evidence until 1938, when *Guinier* [155] and *Preston* [156] studied independently aged Al-alloys by X-ray and noticed scattering of X-ray due to those knots.

### 3.4.1.2 Mechanism of age hardening

Formation of the precipitates requires heating the alloy to higher temperatures. In order to avoid melting and oxidation, which may affect the ductility, the heating temperature should be ( $T_{\text{solidus}} < T < T_{\text{solvus}}$  [105, 120]. The alloy reaches the stable single phase  $\alpha$  at this temperature (figure 3.18). After that, fast cooling is indispensable to reach the supersaturated solid solution. Figure 3.18 shows quenching of solid solution phase ( $\alpha$ ) in Al-4% wtCu alloy to a temperature of the tie line (at point **a**). According to the tie line, the initial concentration of the

precipitation is 4% and that is much more the equilibrium concentration, which is at point **b**. This excess of Cu in  $\alpha$  phase will increase the driving force for formation the precipitation and help in a quick nucleation. The extra Cu atoms come out of the matrix and concentrate homogeneously in many regions forming an intermetallic compound  $\text{Al}_2\text{Cu}$  ( $\theta$  phase). However, in reality this is not simply happen, there are three phases forego this intermetallic phase ( $\theta$ ) [105, 120].

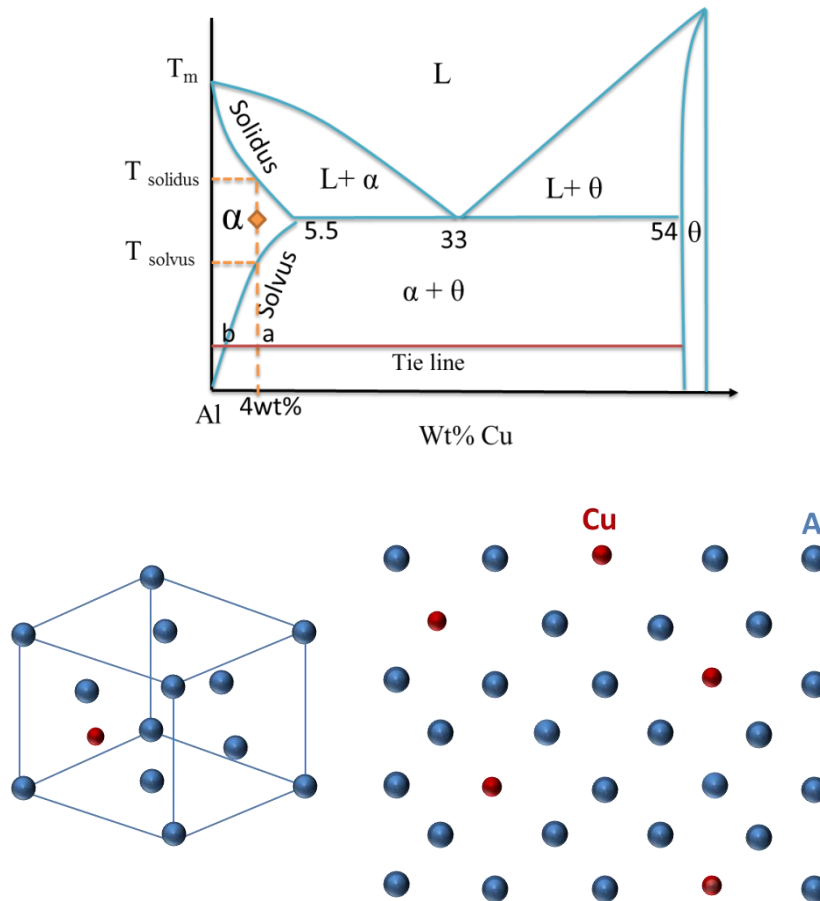


Figure 3.18: Al-Cu alloy Phase diagram (up);  $\alpha$  is a cubic closed pack substitutional solid solution of Cu in Al,  $\theta$  is an intermetallic compound  $\text{Al}_2\text{Cu}$  (down) [120].

In spite of the excess of Cu atoms, this is not sufficient to form  $\theta$  precipitates. The extra Cu atoms diffuse (with the help of the quenched-in vacancies or by substituting Al atoms) configuring a preferable lowest energy shape, which is a disc with a diameter from 3 to 10 nm. This first precipitates are the Guinier–Preston (GP) zones [155, 156]. As it is illustrated in figure 3.19, **GP zones** are coherent with Al matrix (have the same crystal lattice as that of aluminum, 0.404 nm). **GP zones** are possible only in one dimension; however the lattice planes must be bent to give one-to-one matching. This slightly distortion produces lattice-

strains, which hinder the dislocation motion, and therefore creates hardness in the alloy [51, 157].

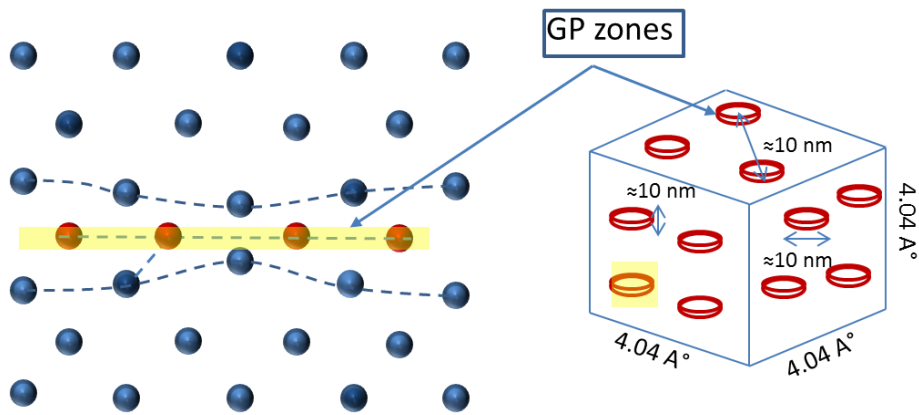


Figure 3.19: Schematic illustration of GP zones in Al-4wt%Cu alloy [158].

GP zones are then starting to nucleate and grow, since Cu atoms diffuse towards them producing plates of precipitates called  $\theta''$  ( $\text{Al}_3\text{Cu}$ ) with a maximum diameter of 150 nm.  $\theta''$  precipitates have different crystal structure than matrix; tetragonal with a lattice constant 0.384 nm. They have a lattice constant less than that of the matrix, this result in a coherency strain in this direction (figure 3.20) [158, 159].

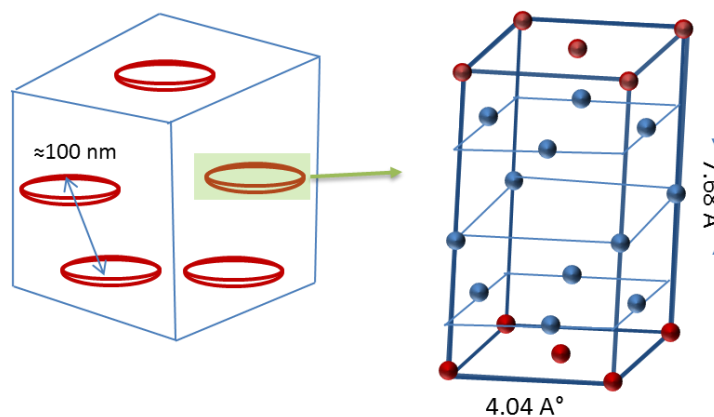


Figure 3.20: Schematic diagram of  $\theta''$  precipitates in Al-4wt%Cu alloy [158, 159].

Growth of more Cu atoms is not energetically preferable due to the high strain energy. As a result of that, a heterogeneous nucleation at dislocations starts producing a new phase called  $\theta'$  with maximum diameter of 1000 nm.  $\theta'$  precipitates are semi-coherent with Al matrix and have a tetragonal structure with a lattice constant of about 0.290 nm.

The strain around those precipitates is a bit small due to the dislocations strain field (figure 3.21) [159]. This phase is the main reason of increasing the hardness in Al-Cu based alloys.

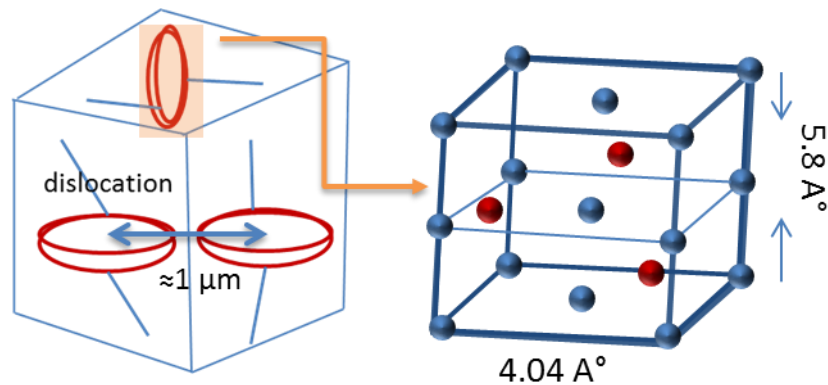


Figure 3.21: Schematic description of  $\theta'$  precipitates in Al-4wt%Cu alloy [158, 159].

Eventually, the equilibrium fully incoherent precipitates  $\theta$  ( $\text{Al}_2\text{Cu}$ ) are formed within the matrix; the lattice constants are  $a=0.607\text{nm}$  and  $c=0.487\text{ nm}$ .  $\theta$  phase (figure 3.22) has the lowest strain energy and results from the heterogeneous nucleation at the grain boundaries and dislocations at  $\theta'$  precipitates [160].

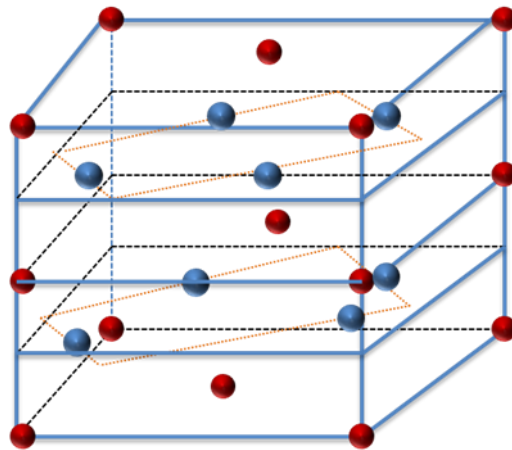


Figure 3.22: Schematic description of  $\theta$  precipitates in Al-4wt%Cu alloy [92, 158, 159]

The strain energy of  $\theta'$  precipitates and the dislocations cancel each other, which leads to softening of the alloy. Fine precipitation becomes coarse and the interfacial energy decreases due to the ‘‘Ostwald ripening’’ process [161]. The average precipitate size increases and the total number of precipitates decreases (the interparticle spacing increase) as a function of time; so  $\theta$  precipitates are formed and overageing occurs [162]. The actual ageing mechanism is illustrated in figure 3.23.

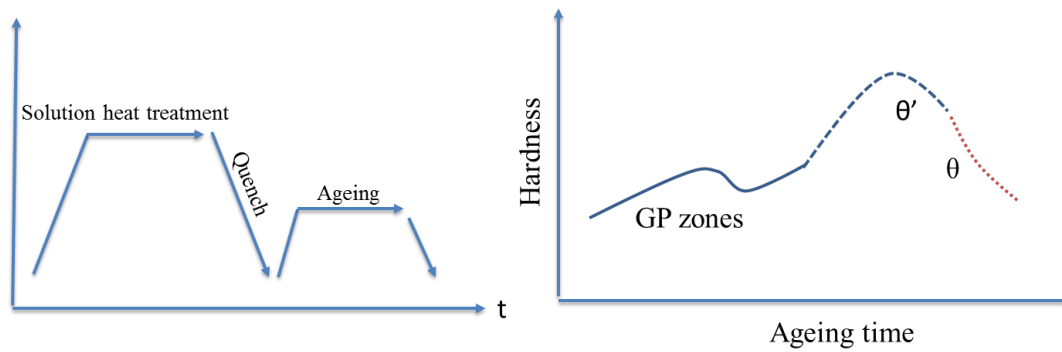


Figure 3.23: schematic illustration of heat treatment and hardness mechanism of Al-4wt%Cu alloys [159].

### 3.4.1 Mechanisms of obstacle dislocations

#### 3.4.1.1 Precipitation cutting mechanism

Consider a precipitate particle in the motion of a slip plane and a dislocation line move towards it (figure 3.24). If the precipitate is coherent and small, then the dislocation line will move through and cut it [163]. As a result of that, the upper half will slip corresponding to lower half by a Burger vector  $\mathbf{b}$  and, therefore a new surface is formed. The formation of a new surface requires extra energy, which substitutes from the dislocation energy [90, 164].

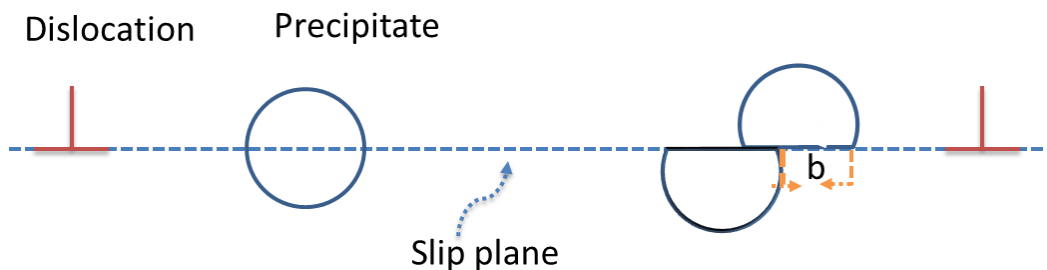


Figure 3.24: Schematic illustration of precipitate cutting by a dislocation [165].

#### 3.4.1.2 Dislocation bowing mechanism

When the precipitates become much large, and hence difficult to be cut (the spacing in between is large enough), the dislocation can bow between them (Orowan mechanism [103]) forming a loop around the particle. Similarly, these loops need an extra energy, which will hinder the motion of the dislocation (figure 3.25) [90, 164].



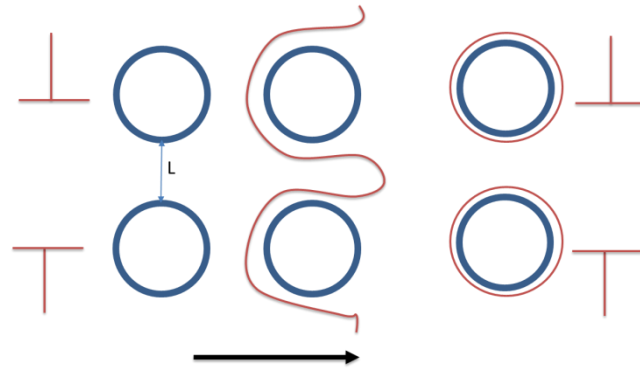


Figure 3.25: Schematic representation of dislocation bowing around precipitates (Orowan mechanism) [90, 159].

The shear stress required to bend a dislocation is inversely proportional to the average interspacing ( $L$ ) of precipitates,

$$\tau = \frac{Gb}{L}, \quad L = \frac{4(1-f)r}{3f} \quad (3.15)$$

$G$  is the shear modulus,  $b$  is the Burger vector,  $r$  is precipitate radius, and  $f$  is the volume fraction. Increasing  $L$  will decrease the stress, which is required to move dislocation, and hence overageing occurs. Once the right interspacing of particles is achieved, optimum strengthening occurs during ageing.

### 3.4.2 Hardness

Hardness is a relative term when referring to materials; both metal and non-metal. In general, hardness involves high melting points, scratch resistances, and high resistances to deform under pressure. Chromium is among the hardest metallic elements compared to transition metals such as copper and iron. However, compounds and alloys of metals and other elements can be harder than those in their pure state [166].

### 3.4.3 Hardness vs Temperature

The maximum hardness is reached in a shorter time at higher temperatures. Whilst, the slow cooling results in the formation of  $\theta$  precipitates, which decreases the hardness. After quenching, the transformation temperature is very low, and thus the hardness increases. The growth will be slow after the fast nucleation and this leads to form fine and coherent precipitates (figure 3.26).

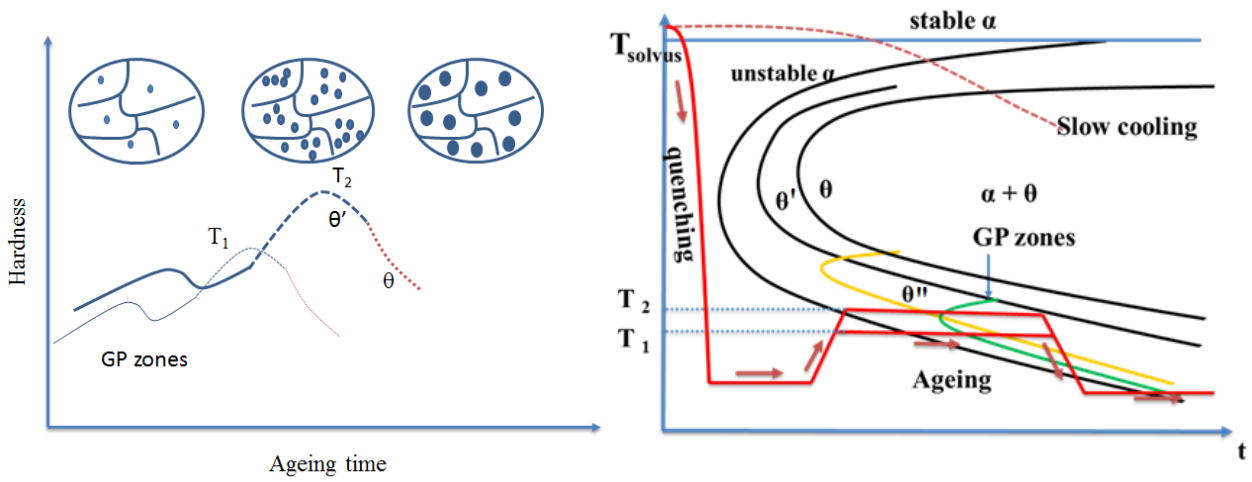


Figure 3.26: Hardness vs Temperature. TTT diagram illustrates the precipitation reaction  $\alpha \rightarrow \alpha + \text{Gp zones} \rightarrow \alpha + \theta'' \rightarrow \alpha + \theta' \rightarrow \alpha + \theta$  [136].

## Chapter 4 : Experimental Techniques

### 4.1 Samples

#### 4.1.1 Sample Preparation

A very high Purity aluminum (5N5) and a 4N purity of the alloying elements were used. A copper mold of about 70 mm in length and 11 mm in diameter was used in casting the alloys. The diameter was reduced by about 1 mm by removing the outer layer by a turning machine to avoid any contamination from the casting process. The alloys were then annealed at 520 °C in air for 4 h. After slowly cooling, the alloys were cut into discs of thickness about 1mm. The measured compositions of all investigated samples are in the table (4.1).

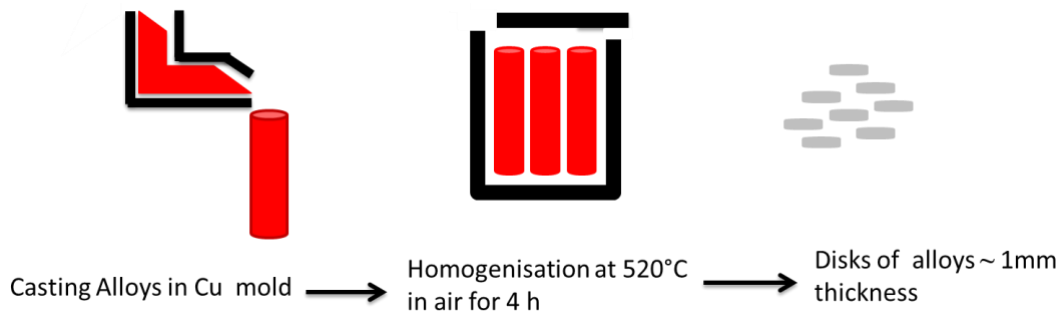


Figure 4.1: Schematic illustration of alloys preparation.

Table 4.1: Chemical compositions of all alloys under investigation.

Sample (nominal composition)	Cu	In	Sn	Bi	Pb	Sb
Al (5N5)	-	-	-	-	-	-
<b><u>Binary Al-alloys</u></b>						
Al-0.005 at. % In	-	0.005	-	-	-	-
Al-0.025 at. % In	-	0.025	-	-	-	-
Al-0.005 at. % Sn	-	-	0.005	-	-	-
Al-0.025 at. % Sn	-	-	0.025	-	-	-
Al-0.025 at. % Sb	-	-	-	-	-	0.025
Al-0.025 at. % Cu	0.025	-	-	-	-	-
Al-0.025 at. % Pb	-	-	-	-	0.025	-
Al-0.025 at. % Bi	-	-	-	0.025	-	-
<b><u>Al-1.7 at.% Cu ternary alloys</u></b>						
Al-1.7 at. % Cu- 0.01 at.% In	1.7	0.01	-	-	-	-
Al-1.7 at. % Cu- 0.01 at.% Sn	1.7	-	0.01	-	-	-
Al-1.7 at. % Cu- 0.01 at.% Pb	1.7	-	-	-	0.01	-

#### 4.1.1.1 Solution Heat Treatment (SHT), Quenching, and Annealing

Temperature is a physical quantity that describes the mean kinetic energy of the particles. In the case of metals, this is the energy of the lattice vibrations of the atoms (phonons). If this energy is sufficiently large, individual atoms leave the regulated lattice structure forming vacancies; it is known as a vacancy concentration in thermal equilibrium [167]. The temperature-dependent concentration of the vacancies is defined by Eq. (2.5) [92, 132],

$$C_v(T) = A \cdot \exp\left(-\frac{E_f}{k_B T}\right) \quad (4.1)$$

A is the pre-exponential constant associated binding entropy of a vacancy,  $\exp(S_f/k_B)$  defined by the change in the lattice vibration around the vacant site,  $S_f = 0.7 k_B$ ,  $E_f$  is the formation energy ( $E_f = 0.67$  eV), which must be applied to create a vacancy [168, 169]. In order to measure the vacancy concentration at a certain temperature, quenching of the desired equilibrium temperature is used. Quenching process is used to freeze vacancies (become immobile to avoid migration to sinks) generated at a high temperature for determining  $C_v(T)$  and obtaining information on the equilibrium defects in metals [169-171]. However, the concentration of the quenched-in vacancies at RT is less than the equilibrium concentration [172]. The quenched-in vacancies are predominantly vacancies, which are present under conditions of thermal equilibrium at higher temperature and do not cluster at lower temperatures [173]. In FCC metals such as Al, mono-vacancies are the main reason of self-diffusion [174]. The number of vacancies in aluminum according to Equation 4.1 is shown in Figure (4.2).

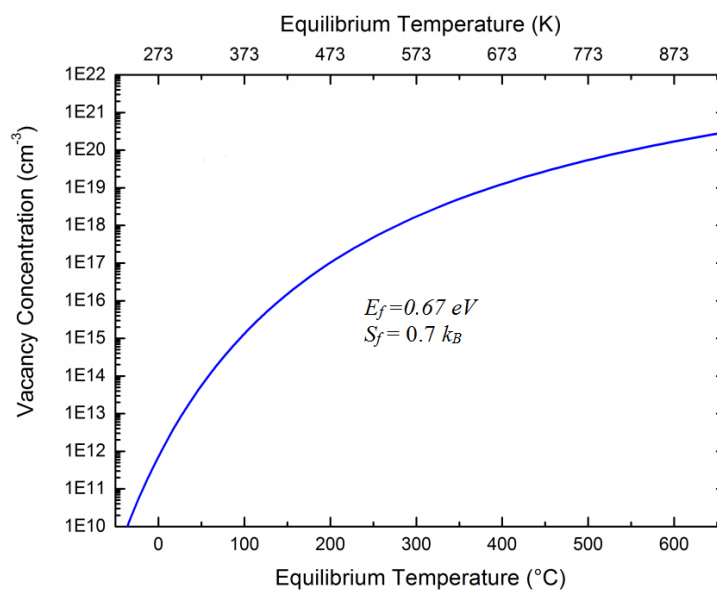


Figure 4.2: The concentration of equilibrium vacancies per cubic centimeter in pure Al.

In order to be able to recognize the nature of the defect, it is not enough to characterize the frozen state only; more information can be provided by the annealing process [167, 175]. Studying of the temperature dependence on the concentration of vacancies enable in estimation of the formation energy of a vacancy in pure metals in addition to the solute-vacancy binding in alloys [176]. The migration energy of vacancy and the binding energy of solute-vacancy can be estimated by studying the rate of decay of excess of vacancies in pure metals and alloys [169]. If the diffusion occurs by vacancy mechanism, the summation of vacancy migration and formation energies must be equal to the activation energy of the diffusion [177, 178]. Annealing of vacancies is the process of disappearance of the supersaturation defects. Because of the mobility of defects increases rapidly with increasing temperature, a suitable temperature interval can always be found in which that rate of disappearance can be measured.

A distinction is made between isothermal and isochronal annealing. Isochronal annealing means heating the sample in steps to successively higher temperatures for constant time. The change in the vacancy concentration is measured at the end of each step. It determines the temperature ranges in which annealing occurred (recovery stages or disappearance of the supersaturation defects).

In order to characterize the recovery stages, heating the sample at each temperature of the recovery temperatures for different times is needed; this is called isothermal annealing. In isothermal annealing, the recovery temperature  $T_R$  (temperature at which vacancies become mobile) is adjusted and the vacancy concentration decreases to the equilibrium value over time. From the isothermal annealing one can calculate the vacancy migration and the solute-vacancy binding energies.

The defect kinetics of quenching and annealing depend heavily on the external parameters such as quenching rate speed [167, 169]. During quenching, the sample is rapidly cooled from a quench temperature  $T_Q$  to a lower temperature  $T_0$ . Typically, the heated sample is dropped into a medium of defined temperature such as ice water, liquid nitrogen, or alcohol solution [167]. The material is suddenly releases the heat energy and assumes the equilibrium temperature, whereby the speed is very decisive. To prevent vacancies from disappearing into sinks, the quench rate should be at least  $10^4$  K / s [167, 179].

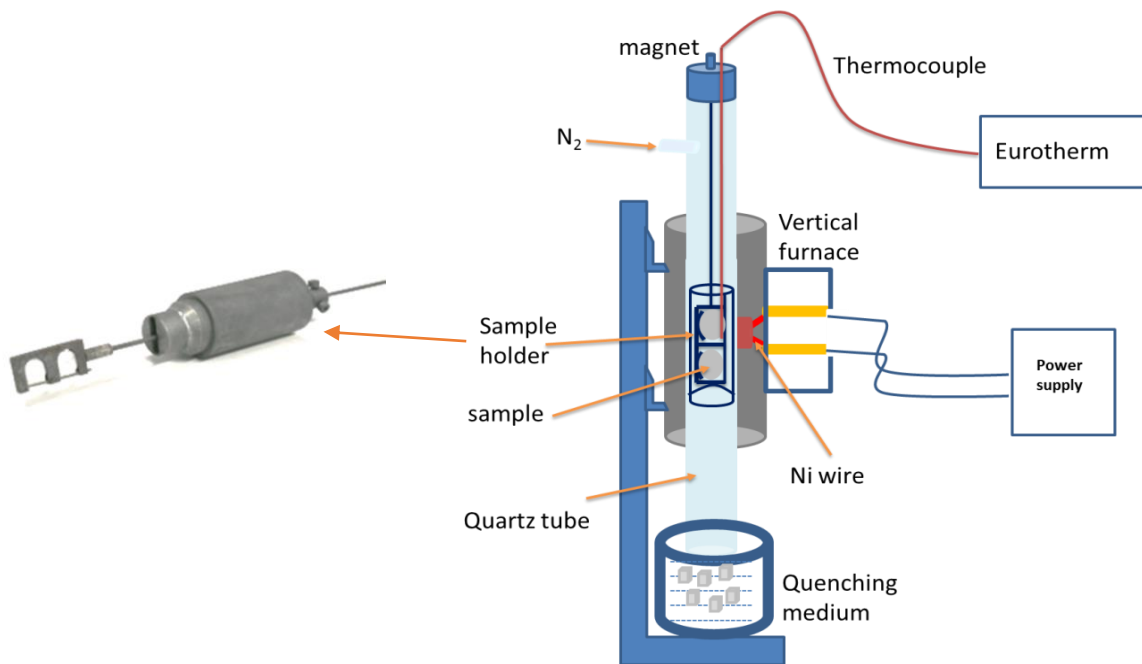


Figure 4.3: Schematic diagram of the quenching setup.

The quenching setup includes a resistance furnace in which the sample is pendulous. To avoid reactions with oxygen, a nitrogen-flooded glass tube is located around the sample. In order to regulate the temperature, a thermocouple is located on the sample holder, which is connected to the oven via a control unit (Eurotherm). The sample holder is fixed by a strong magnet and can be easily decoupled from the outside (figure 4.3). The sample holder is designed for circular samples with 10 mm diameter and 1mm thickness. During the heating, the aluminum samples including sample holder are located in the middle of the oven and can be dropped in the quenching medium by removing the magnet.

Although the quenching rate should be as high as possible, one should minimize creating defects such as dislocations, grain boundaries, and vacancies, i.e. plastic deformation of the sample. This may decrease the concentration of the quenched-in vacancies. During the quenching, di-vacancies or even larger vacancy clusters may be formed due to vacancies interaction. Consequently, the distribution over the various aggregate is not the same as at quenching temperature even if we succeeded in quenching-in all the vacant sites present in thermal equilibrium at the quenching temperature. Even so, in order to reduce vacancies agglomeration during quenching; the vacancy concentrations and, thus the quenching

temperatures must not be so high [92, 169]. For example, vacancies are released more quickly when the dislocation concentration is about  $10^{-3} \text{ cm}^{-2}$  [179].

In the real experiment, there is always a combination of dislocations, impurities, voids, and other lattice defects that interact with each other. Depending on the concentration of each type of defect, the annealing behavior of the metal will change [167].

## 4.2 Instruments and Data Analysis

### 4.2.1 Digital Positron annihilation lifetime spectroscopy (DPALS)

Figure (4.4) shows schematic diagram of the digital positron lifetime spectrometer. It has two photomultiplier tubes (PMT) with two scintillators, a coincidence unit with high-impedance signal extraction, and a dual high voltage box. DPALS uses fast digitizer (50 ohm upstream), which converts the anode pulses from the PMTs to digital values and sent them to a PC for processing [180, 181]. In order to enhance the time resolution, the sampling rate must be high enough ( $\geq 2\text{GS/s}$ ) to capture the leading edge of the detector's signal [58, 180].

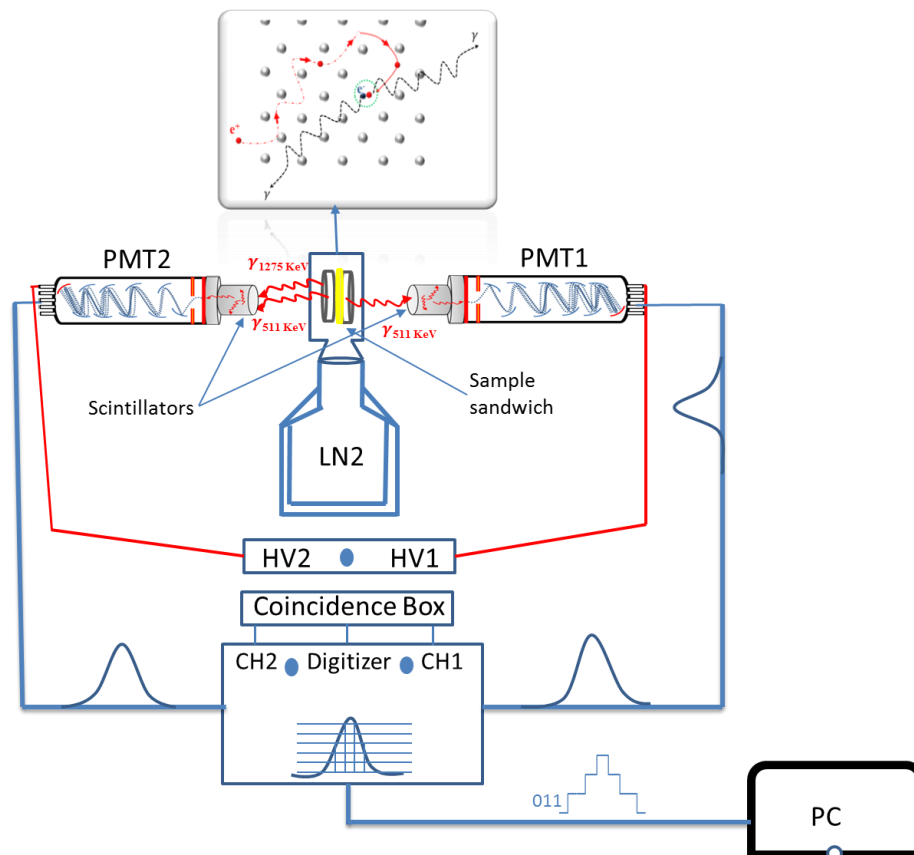


Figure 4.4: Schematic diagram of digital Positron lifetime spectrometer.

Digitizer allows direct sampling of detector signals instead of using analog nuclear instrument modules (constant-fraction discriminator CFD, single channel analyzer SCA, time-to-amplitude converter TAC). In addition to easy setup, low power consumption, and pulse analysis, DPALS has faster and automatic tuning. It has also calibration and multichannel trigger synchronization [58, 182]. An Analog-to-Digital Converter (ADC) is used for the digitization process. The start-of-the-art of DPALS uses a digitizer with different sampling rate (1GS/s, 2GS/s, 3GS/s and 4GS/s), 8 & 10 bit amplitude resolution [58] with more than 3000 event per second for the analysis and storing rate. DPALS is used nowadays instead of the digital oscilloscopes, which has low data throughput.

### **How does DPALS software work?**

DPALS software inverts the data, which come from a PMT. It searches for the first value between its threshold and the trigger box threshold (Point A in figure 4.5); this point is considered as the start point of the signal. The software will then search for another point between the two thresholds to take it as a stop point of the signal (point B). The software will look then for a point at the beginning of the signal (point C, under the black line and smaller than point B) to interpolate the signal itself. Then a cubic spline interpolation will be done to cover the whole area (containing the peak until a point equal to point C in height from the other side of the signal). After interpolation, the interpolated maximum of the pulse is obtained with a smoothed leading edge (see figure 4.5) [181].

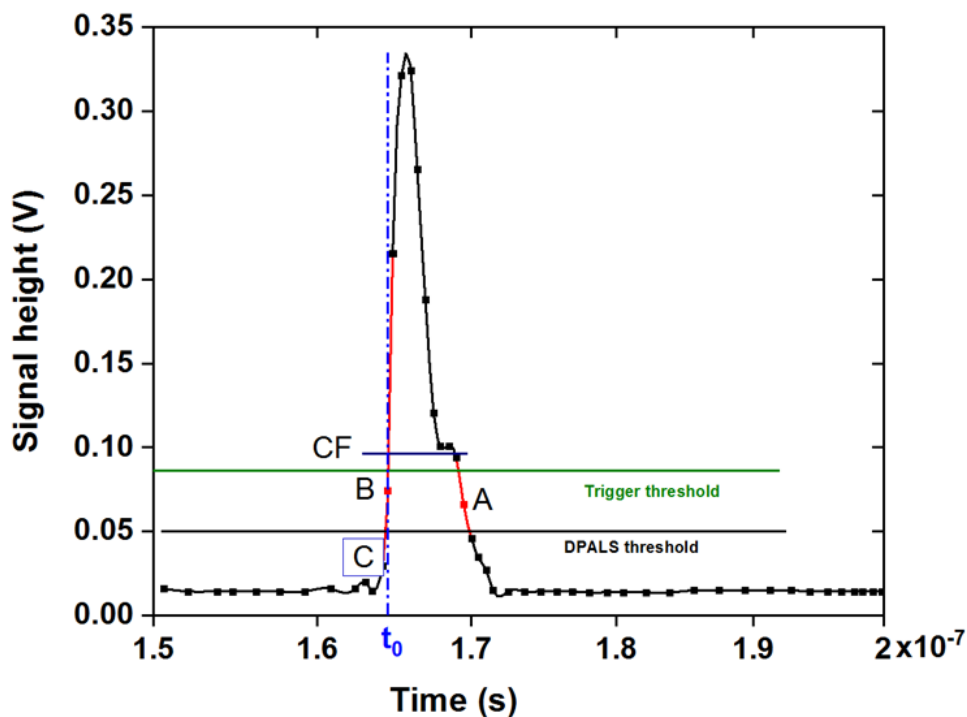


Figure 4.5: Digital timing process with constant fraction [58].



To avoid the mismatching of the signals heights, i.e. signals rise time may be much longer than the desired resolution; the interpolated maximum shall be multiplied by a constant fraction level CF of the total peak height (30% from the whole signal). The first interpolated point above this constant fraction value will be searched at the leading edge of the pulse. Thereafter, the interpolated points below and above the constant fraction value are used for a linear fit with two points to get the exact value of the signal time zero. The difference between the two values of the signal time zero of the start and stop signals gives the positron lifetime [58, 181].

The digitizer is triggered by a coincidence trigger unit. As soon as the trigger triggers and a signal is sent to the digitizer, the recorded data will be sent to the DPALS software in the PC. The trigger triggers when a set voltage pulse threshold is exceeded the adjustable time range in the two PMTs. The software then checks whether they fit into the energy window of start or stop pulses. Contrary to the analog, in the digital system each PMT can be used for a start or a stop pulse. This allows improving the count rate with using more PMTs. The number of measured individual spectra N is calculated as  $N = n(n-1)$ , where n is the number of the used PMTs. Two spectra are recorded simultaneously by using two PMTs with 180° geometry while, four tubes with 120° geometry gives 12 spectra [167].

DPALS at Halle University can measure the positron lifetimes at different annealing temperatures; the positron lifetime is measured at RT after each annealing step. The cooling is done by liquid nitrogen; pre- and turbo molecular pumps are necessary for cooling. The temperature control operates via a resistance heater, which is mounted below the sample holder and controlled by an Eurotherm. A thermocouple on the sample holder provides the required actual temperature value. The decomposition of the lifetime spectra is performed using standard computer programs, which are based on Gauss-Newton non-linear fitting routines. LT9 or LT10 programs are used for the evaluation of the positron lifetime spectra [183, 184]. MELT (Maximum Entropy for LifeTime analysis) is another program [185], which specifies the distribution of the lifetime and number of the components.

#### **4.2.2 Digital Coincidence Doppler Broadening Spectrometer**

Figure (4.6) shows a schematic diagram of digital CDB spectrometer; it uses two channels 8-bit digitizer. In order to improve signal-to-noise ratio, the preamplified HPGe detector pulses

are first amplified and shaped by Spectroscopy Amplifier Ortec 672 with timing constant of  $6\mu\text{s}$ . Pseudo-Gaussian waveform pulses produced by the spectroscopy amplifier are then sampled by a digitizer, which is triggered by a coincidence Ortec 414A with coincidence time of 110 ns.

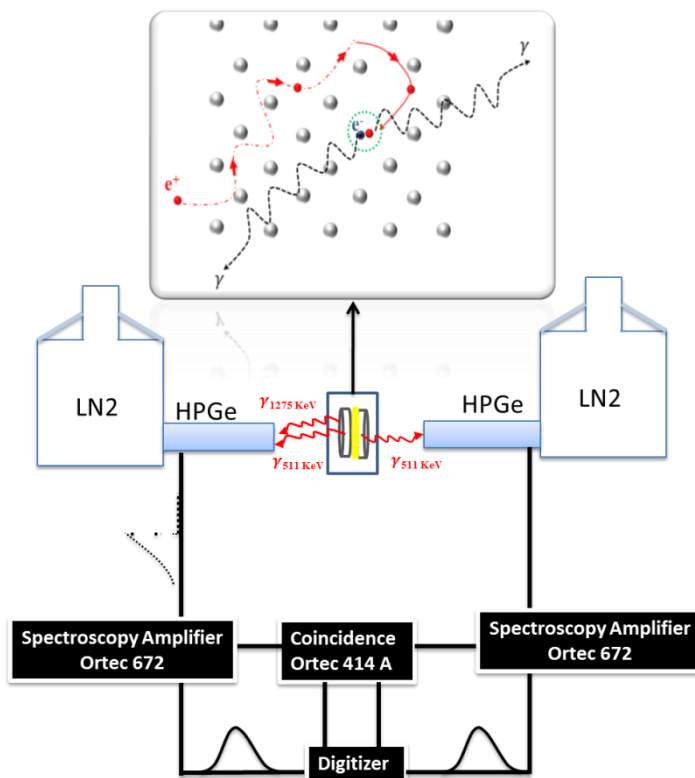


Figure 4.6: Schematic illustration of coincidence Doppler broadening spectrometer [15, 74].

The sampled waveforms are analyzed off-line by using a software [74]. Different modes of analysis, i.e. single mode and coincidence mode can be selected by setting the trigger level of the digitizer. In the single mode, one photon detected in any detector is the trigger. However, the trigger in the coincidence mode is triggered by two photons detected simultaneously in both detectors [74]. The trigger level of digitizer may be adjusted at any time during measurement by a simple software command [74].

#### 4.2.3 Heat flux Differential Scanning Calorimetry (DSC)

A calorimeter measures the heat into or out of a sample. A differential calorimeter can measure the heat of a sample relative to a reference [186]. Differential scanning calorimetry (DSC) is utilized to study the thermodynamics of phase changes in alloys.

The difference in the amount of heat required for increasing the temperature of a sample and a reference is measured as a function of the temperature.

DSC is useful for precipitation reactions in light alloys. The nucleation (formation) or dissolution of a phase in a DSC experiment is characterized by a heat flow peak over the reaction temperature range [187]. The sample and the reference materials are heated by separate heaters in order to keep their temperatures equal, i.e. zero temperature difference [188].

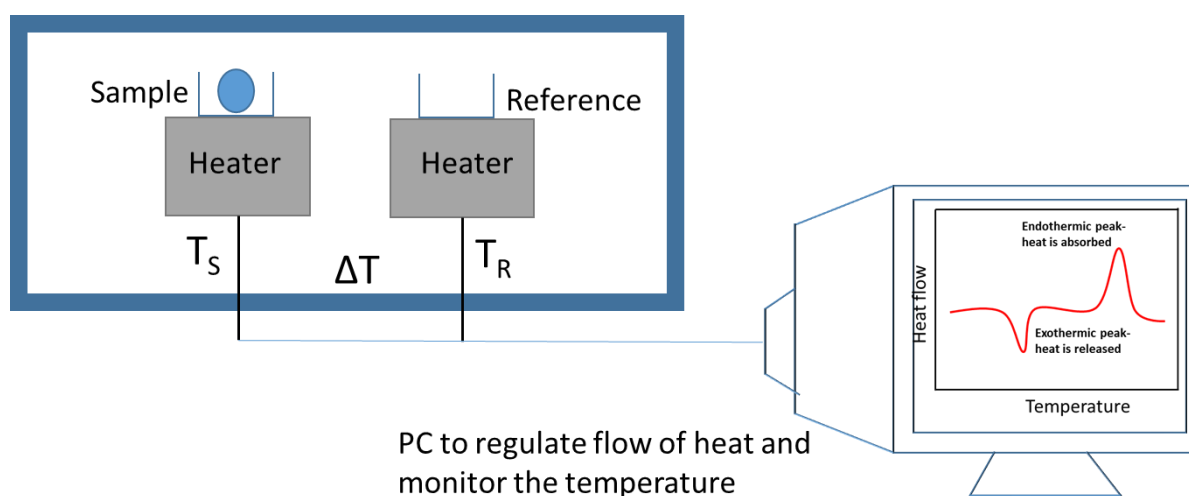


Figure 4.7: Schematic diagram of the heat flux DSC.

If the sample absorbs some amount of heat, the reaction is said to be endothermic. In this case, more heat is needed to maintain the zero temperature difference, i.e. the dissolution of the precipitates (upward peak in the DSC curve). In contrast, the formation of the precipitates will release some amount of heat. Here, less heat is needed to maintain zero temperature difference, this process is called exothermic (downward peak in the DSC curve) [189].

The alloys under investigation were cut as square-shaped samples with a mass of 45 mg to be used in DSC technique. A surface grinding on one side was important to ensure a good contact with the Al-crucible. The heat-flux DSC measurement was carried out in a Netzsch 204 F1 Phoenix apparatus with a heating rate of 20 K/min in a range from -20°C to 530°C under nitrogen atmosphere. To provide equal heat capacities over the temperature range, all samples are measured against pure aluminum (5N) as a reference. Finally, for a better visualization, the data were corrected for baseline, displayed, and then shifted by a similar amount [190, 191].

#### 4.2.4 Electron microscopy

The interaction of electrons with matter makes electron microscopy possible, since change in the electrons after interaction (or new electrons with different energies) will be generated.

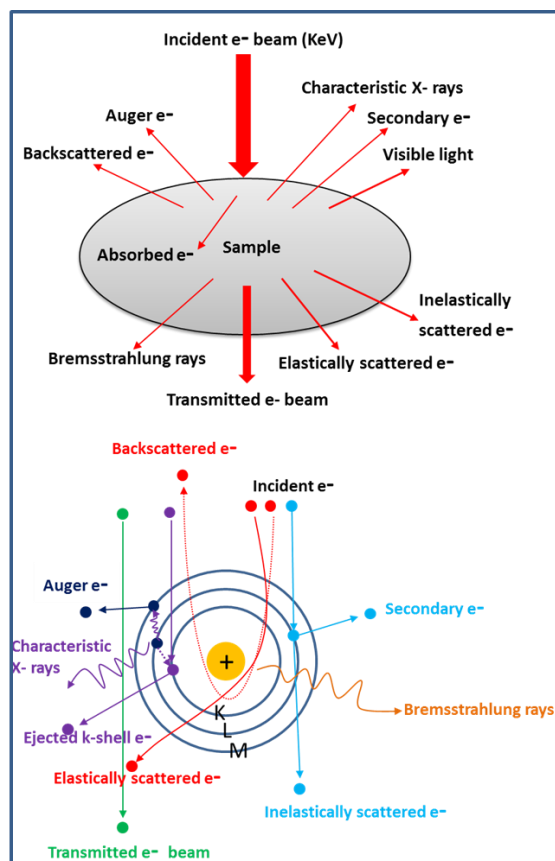


Figure 4.8: Schematic description of the processes result from the interaction of electrons with matter.

##### 4.2.4.1 Transmission electron microscope

Transmission electron microscope (TEM) is a very powerful tool, which is used to observe crystal structure and features in the structure (precipitations, dislocations, and grain boundaries). A strong electrons beam (instead of light as in light microscopy) is transmitted through a very thin sample, which forms an image of the crystal structure. The image is then magnified and focused onto an imaging device or detected by a charged couple device (CCD camera). One of the main applications of TEM is to study particles size and shape. The size distribution of particles (the growth of layers and their composition), i.e. precipitations can be also investigated. The beam of electrons are emitted from a tungsten filament and then

focused by magnetic coils, which act as an electromagnetic condenser lenses system [192, 193].

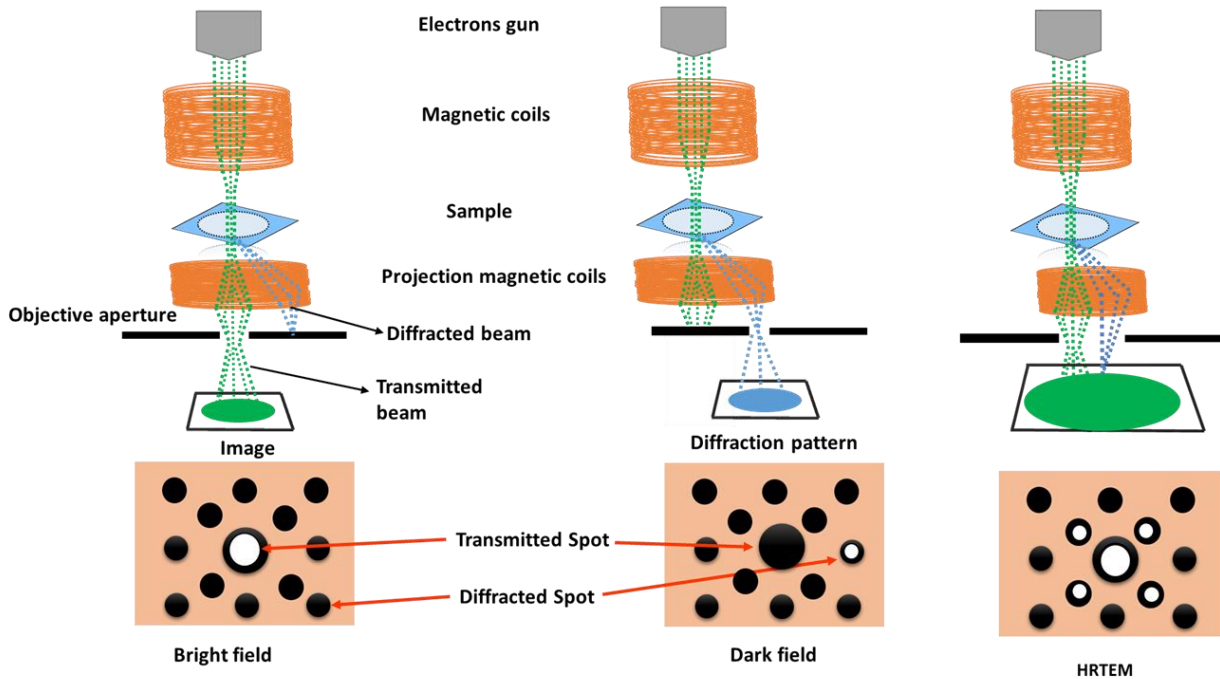


Figure 4.9: Schematic diagram of different mode of imaging of TEM [194].

Figure (4.9) shows different imaging modes of TEM; in the bright field (BF) mode, only the transmitted beam is allowed to pass through the objective aperture. However, in the dark field (DF) images, the transmitted beam is blocked, while one or more diffracted beams are allowed to pass the objective aperture. The high-resolution transmission electron microscope (HRTEM) uses both beams for imaging. To obtain lattice images, a large objective aperture has to be selected, which allows many beams including the direct beam to pass. The image is formed by the interference of the diffracted beams with the direct beam (phase contrast). If the point resolution of the microscope is sufficiently high and a suitable crystalline sample oriented along a zone axis, then high-resolution TEM (HRTEM) images are obtained. In many cases, the atomic structure can directly be investigated by HRTEM [195].

#### 4.2.4.2 Scanning electron microscope

Scanning electron microscope (SEM) allows directly studying the surface of a solid by detecting the secondary and backscattered electrons produced by the specimen. The electron beam is scanning across the sample; secondary electrons generate a topographical image of

the sample surface, while the backscattered electrons give useful information about the composition [196].

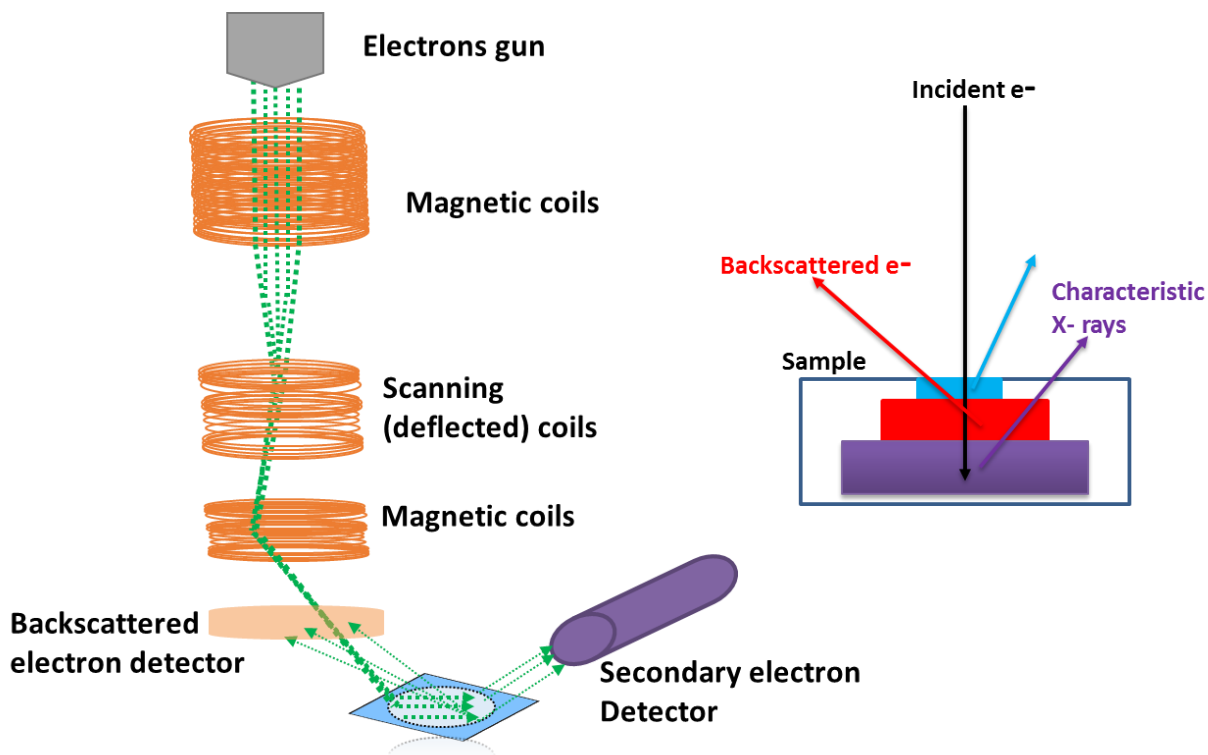


Figure 4.10: Schematic diagram of SEM.

In case of using the transmission electron microscope in the scanning mode, transmitted, secondary, and backscattered electrons can be detected. In the scanning transmission electron microscope (STEM), electron beam is focused to a small spot and scanned across the sample [196].

#### 4.2.5 Vickers Hardness

To rate and compare the hardness of materials, many tests and measurement scales are used. For example, the Mohs scale (after *Friedrich Mohs* [197]) is a relative rating system that compares the scratch resistance of the materials. The material must be harder if it can scratch another. The Vickers scale uses a pyramidal indenter made from diamond, which is pressed into the material, the resulted number reported as Vickers Hardness (VHN) [166]. The material is harder when the indentation is smaller. The Vickers Hardness test is easy to use, it has a very wide scale, and its small indenter reduces the risk of possible damage of the test material.

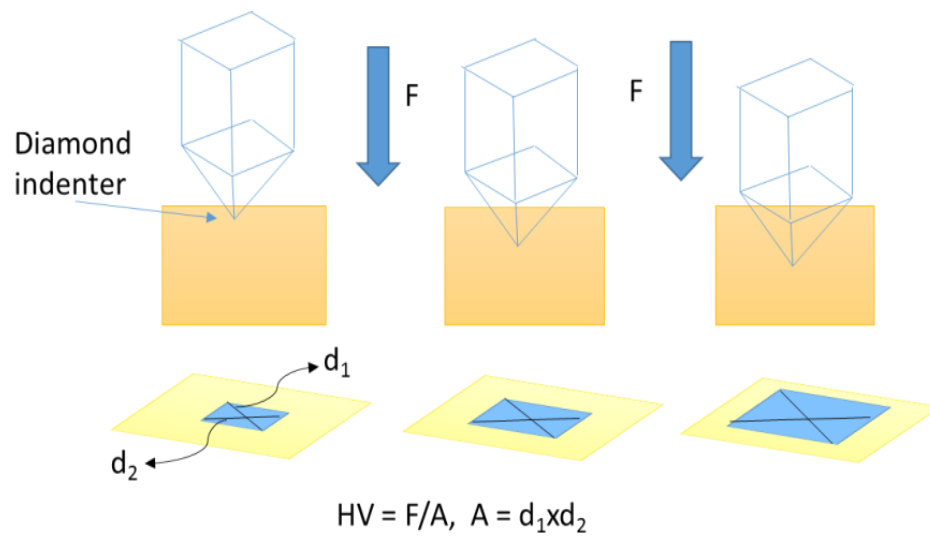


Figure 4.11: Schematic diagram of Vickers hardness test indentation [198].

Hardness testing of the alloys under investigation was done on a tool of the type VMHT by the company Uhl following the norm ISO 6507 using the load level HV0.5. The printed result is the average of 5 single measurements.

## Chapter 5 : Results and discussion

### 5.1 Introduction and survey

The strengthening of Al-Cu alloys returns to the precipitation hardening occurred by Cu-rich precipitates, as it was explained in chapter 3. It has been found that adding small amounts of Cd, In or Sn can affect the precipitation sequence, which has different sizes and distributions (GP-I  $\rightarrow$  GP-II/ $\theta''$   $\rightarrow$   $\theta'$   $\rightarrow$   $\theta$ ) in Al-Cu alloys [199, 200]. As a result of that, the final strength is changed. This returns most likely to the diffusion of solute (Cu atoms) facilitated by quenched-in vacancies [200-202]. Vacancies can interact not only with each other but also with solute atoms forming solute-vacancy complexes (bound vacancies), which can keep the vacancies thermally stable. Quenched-in vacancies can bind the trace elements in the Al matrix, which can influence the diffusion behavior of Cu atoms, and thus change of the precipitation sequence inside the alloy [200]. The solute-vacancy binding energy  $E_b$  is defined as the difference between the energies required for the formation of a vacancy in the solute free atom and in a site, which has only one solute atom in its nearest neighboring position. The exact equilibrium concentration difference of vacancies in a pure metal and in an alloy is a function of temperature, solute concentration, and binding energy. Binding energy for i.e. In-atoms is about 0.2 eV [50, 203].

Al-Cu system led to search for other alloys (by adding or even subtracting other alloying elements to aluminum) that might precipitate harden [199]. *Hardy, Chadwick, and Vonzeerleder* [204, 205] predicted that addition of a small amount of the trace element (0.05-0.1wt% of Cd, In, Sn) can accelerate and increase the hardening in the Al-Cu alloys. They return this to the interaction between Sn atoms and the vacancies (Sn atoms bind the vacancies). Moreover, *Hardy* [204] said that atoms, which are larger than aluminum, could affect the nucleation of the precipitation. *Polmear* and *Hardy* [206] return that to the formation of intermediate precipitates in the ternary alloys. *Silcock et al.* [207-209] investigated systematically the effect of trace elements on the precipitation behavior in Al-Cu binary alloys. They found that the intermediate precipitates  $\theta'$  is formed at a temperature less than 300 °C. While, the solid solubility of In, Sn is small but fine at 530 °C and decreases with decreasing temperature. The effect of quenching rate and trace elements on the formation of  $\theta'$  was studied by *silcock* in 1959 [210], he found that not only slow quenching but also trace elements e.g. In, Sn decreases the formation rate of GP zones. Trace elements form more efficient nuclei for  $\theta'$  than dislocations since strong solute-vacancy binding prevent Cu atoms





## 5.2 Hardness measurement

Figure (5.2) displays hardness curves\* for Al-1.7at.% Cu with and without trace elements during natural (bottom) and artificial (top) ageing. For natural ageing, one immediately recognizes that Al-Cu alloy is harder than Al-Cu-In and Al-Cu-Sn due to the formation of GP-I zone. However, there are only a very small deviations for Al-Cu-Pb compared to the pure Al-Cu alloy. The alloy with indium shows the first rise of hardness after about 4 h and the hardness stays for all times above the alloy containing tin. The hardness first rise of the alloy containing tin is reached after about 20 h.

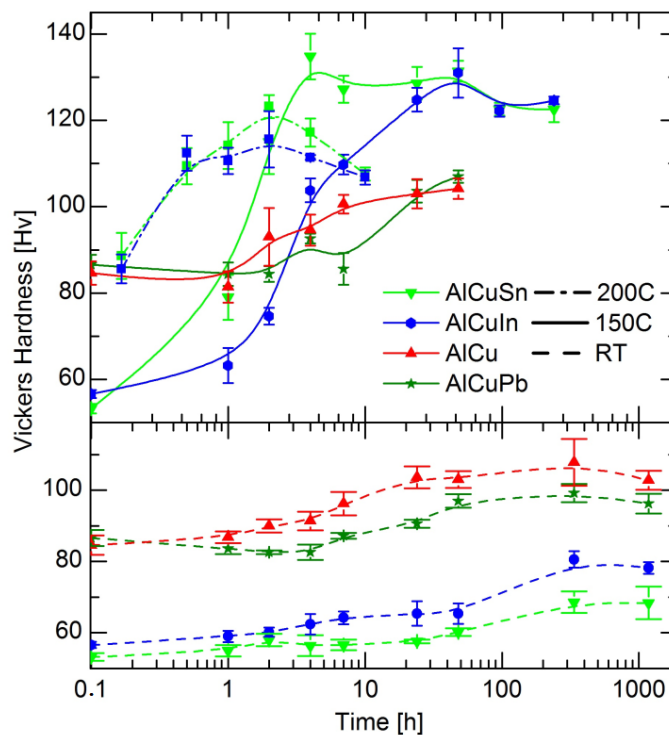


Figure 5.2: Hardness curves as a function of natural ageing (bottom) and artificial ageing at 150 and 200 °C (top) for Al-1.7 at.% Cu binary alloy and the ternary alloys with 100 ppm trace elements (In, Sn and Pb).

For artificial ageing at 150 °C (figure 4.5 top), there is no significant difference between Al-1.7 at.% Cu alloy with and without Pb and the behavior is similar to that of the natural ageing. The hardness peak reached 100 Hv after 48 h artificial ageing. On the other hand, Al-1.7 at.% Cu containing In and Sn show a very rapid hardening response with higher values of 130 Hv after different ageing times: 48 h for In and 4 h for Sn. Artificial ageing was performed also at 200 °C. The maximum hardness is reached after only 2 h ageing (120 Hv) for both alloys with In and Sn, which is above that of artificial ageing at 150 °C.

\*Done by Dr. Birgit Vetter (TU Dresden)

### 5.3 Positron measurements

Positron lifetime measurements were carried out by a digital positron lifetime spectrometer having a time resolution of 170 ps (FWHM) [200, 214]. A 25  $\mu\text{Ci}$   $^{22}\text{Na}$  positron source is deposited on 6  $\mu\text{m}$ -thick Al foil and sandwiched between two identical samples. The source correction of 16.9 % is obtained. After source and background corrections, the lifetime spectra were decomposed to one or two components,

$$n(t) = \left(\frac{I_1}{\tau_1}\right) \exp\left(-\frac{t}{\tau_1}\right) + \left(\frac{I_2}{\tau_2}\right) \exp\left(-\frac{t}{\tau_2}\right).$$

The spectra are convoluted with the Gaussian resolution function of the spectrometer using the lifetime program (LT9) [183]. The average positron lifetime is determined from the lifetime decomposition,  $\tau_{\text{avg}} = \sum_i I_i \tau_i$ . Here,  $\tau_i$  and  $I_i$  are the positron lifetime and its relative intensity, respectively, of each lifetime component  $i$ .

#### 5.3.1 Al (5N5)

Well annealed high purity aluminum (99.9995 %, 5N5) has been used for two reasons; firstly, to determine the source contribution, which is subtracted from all measurements. Secondly, to figure out the influences of adding the trace elements to the pure Al. Positron in Al-5N5 matrix and after thermalization presents far away from the positively charged nuclei, mainly in the interstitial regions, then it annihilates preferentially with valence electrons. Positron bulk lifetime in Al-5N5 is about 158 ps, which is in a good accordance with [42]. Positron is trapped into a vacancy or vacancy clusters of various sizes in aluminum, and thus its lifetime depends on the number of the vacancies in the cluster [215].

*Puska and Nieminen* [216] calculated positron lifetimes in FCC aluminum for positrons trapped at vacancies, vacancy clusters and impurity-vacancy complexes in order to help in the analysis of the experimental data [216]. The difference between the lifetimes at a vacancy and at divacancy is rather small: about 20% in FCC metals however, the lifetime increases sharply when the cluster becomes three dimensional. Figure (5.3) shows the calculated positron lifetime in vacancies in FCC Al [216].

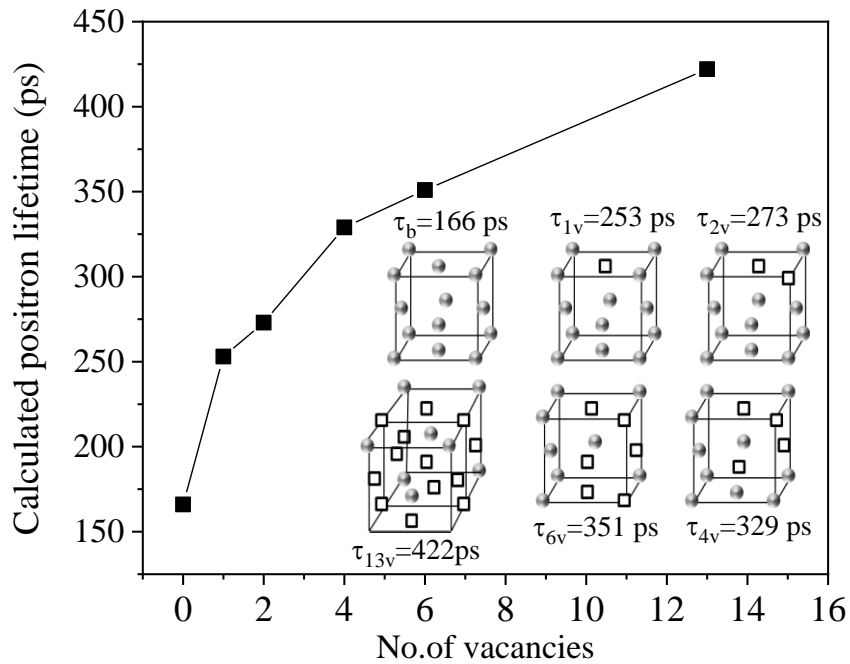


Figure 5.3: Calculated positron lifetime in FCC Al with and without vacancies [216]

Besides annihilation in the vacancy-type defects, positrons also annihilate in the bulk, since the concentration of vacancies is most likely lower than the saturation trapping limit [42, 217]. Vacancies are the dominating defects at higher temperature; there is a thermodynamically stable concentration above 0 K [15]. The experimental defect-specific positron lifetime for mono- and di-vacancies in Al-matrix is about 240 and 280 ps, respectively [218]. *Puska and Nieminen* attributed the difference between the calculated and the experimental positron lifetime to the neglect of a self-consistent electronic relaxation at the defect. Moreover, the positron wave function in the vacancy (or interstitial) region likes to relax towards higher electron density. Figure (5.4) shows the generation of thermal vacancies in Al (5N5). The vacancies are induced by increasing temperature. Starting from 550 K (277 °C), the defect-related positron lifetime is  $\tau_2 \sim 242$  ps with high intensity  $I_2$ . By applying the trapping model, the reduced bulk lifetime  $\tau_1$  is always lower than the bulk lifetime  $\tau_b$  [15, 219]. After cooling the sample, the average positron lifetime is reached the bulk value ( $\tau_{av} = \tau_b = 158$  ps) at room temperature.

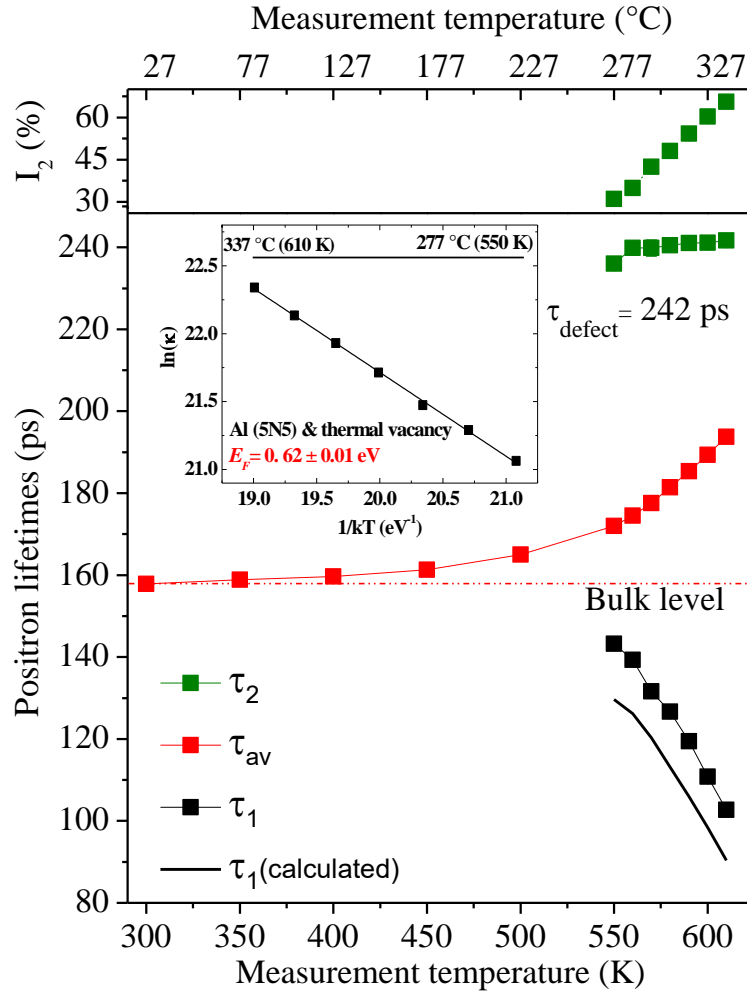


Figure 5.4: Thermal vacancies generation in Al (5N5) (inset, the vacancy formation energy calculated from positron lifetimes).

### 5.3.1.1 Quenched-in vacancies in Al-5N5

The sample is homogenized and quenched in ice water ( $\sim 0$  °C) at  $T_Q$  of 470 and 620 °C. After quenching, the sample is directly prepared as a sample-source sandwich and mounted into the spectrometer. There is a time of 5 to 10 minutes, which is negligible compared to the duration of the measurements. Although a large number of generated vacancies are expected [170], the sample showed an average lifetime of 171 ps, which is close to the defect-free bulk lifetime (158ps) (see figure 5.5). This indicates that only a slightly lower amount of defects induced by the quenching process, i.e. quenching high purity Al-5N5 from low temperature (470 °C) resulted in a slightly lower amount of vacancies surviving the quenching process. The defect-related lifetime  $\tau_2$  of the as quenched sample indicates the presence of vacancy clusters (about 325 ps) with very small intensity. The defect-related lifetime  $\tau_2$  increases due to locally reduced electron density. *Ehrhart and Gavini et al.* [168, 220] confirmed by

calculations that the vacancy cluster in pure aluminum is energetically favorable and prefers to further cluster rather than split into mono or divacancies [171].

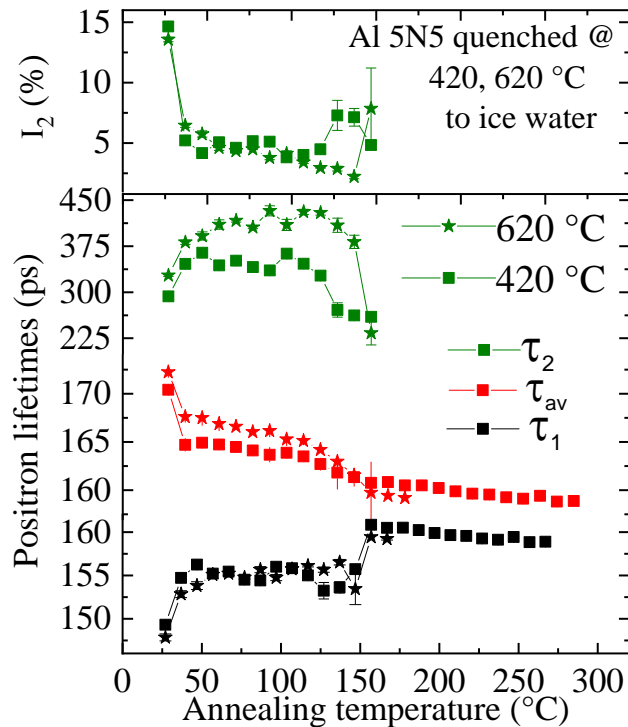


Figure 5.5: The measured positron lifetimes of pure aluminum (5N5) as a function of the annealing temperature.

In order to see the recovery stages, isochronal annealing of the sample is done at the given temperature (25-267 °C) for 30 min in steps of 10 °C. It is noticed that the recovery stage appeared very fast and the quenched-in vacancies become mobile at RT. They diffuse quickly to sinks such as dislocations or grain boundaries [171, 172, 221], and thus positron lifetime decreases reaching the bulk value (the bulk annihilation becomes more and more dominant).

### 5.3.2 Quenched-in vacancies in highly diluted binary Al- alloys

#### 5.3.2.1 Al-0.025 at. % Sb, Pb, Bi and Cu at 520-550 °C in ice-water (~ 0 °C)

In order to keep the quenched-in vacancies thermally stable, alloying elements are added to pure aluminum to bind the vacancies [221]. Study of the precipitation behavior in Al binary alloys will help in getting insight into the processes, which take place in aluminum ternary alloys during annealing. A comparison with Al-5N5 is also made. After the alloys are quenched at temperatures in the range of 520-550 °C, they are mounted directly into the

measurement place to be isochronally annealed. The lifetime is measured at RT after each annealing step.

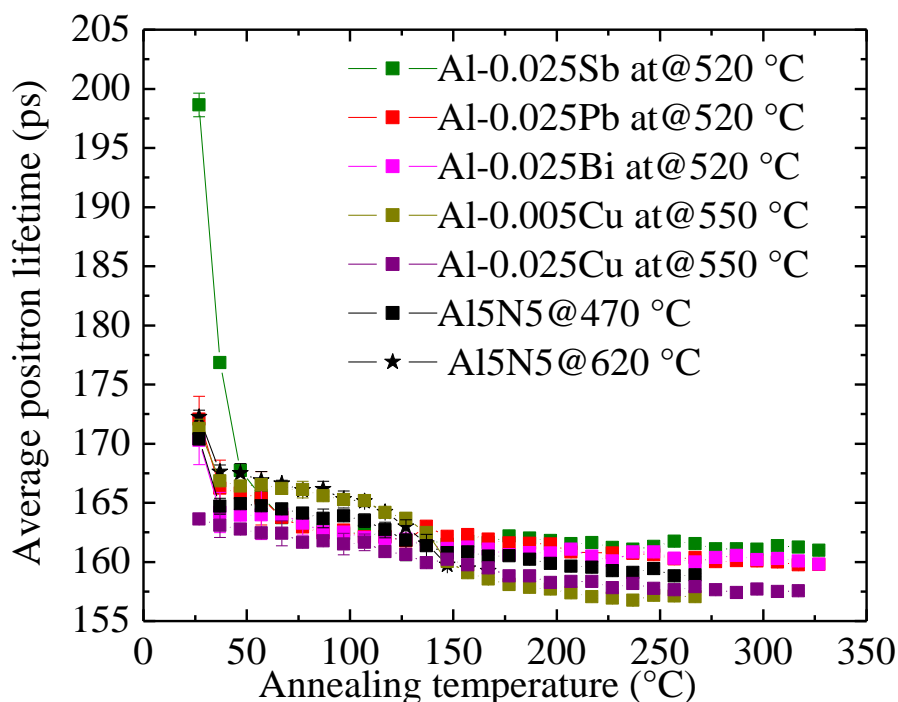


Figure 5.6: Average positron lifetime for aluminum binary alloys with comparison to pure aluminum. The alloys were quenched from 520 or 550 °C to ice water.

According to the calculations done by *Wolverton* [50], it was expected that lead (Pb) and bismuth (Bi) will show stronger interaction with the quenched-in vacancies due to their high binding energies, 0.41 and 0.44 eV, respectively. However, the effect of these elements is surprising (figure 5.6). In all alloys (except Al-0.025 at.% Sb), the defect concentration generated by quenching is very low and very similar to pure aluminum. This is also observed from the low intensity of the generated vacancies ( $I_2$ ) and its quick decrease (see figure 5.7 below). This result is expected for Cu due to its low solubility in Al matrix and hence, very weak binding energy of vacancies ( $\sim 20$  meV according to the calculation). On the other hand, this is surprising for Pb and Bi. The reason for this very weak interaction with quenched-in vacancies may return to the low concentration of Pb and Bi in Al matrix since they have a restricted solubility in Al [200, 222, 223]. Consequently, they bind small amount of vacancies but the concentration is under the positron detection limit.

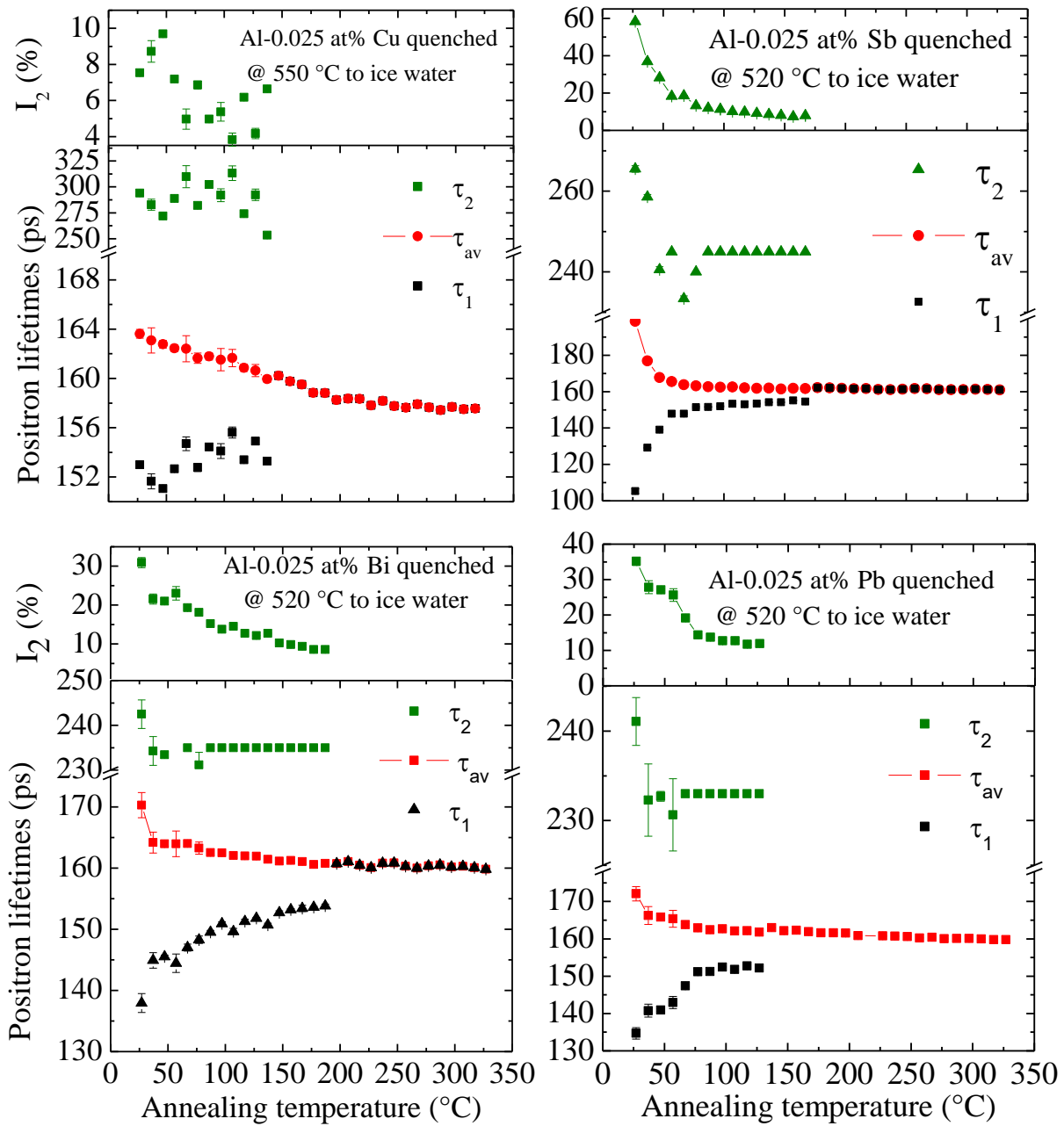


Figure 5.7: Positron lifetimes vs isochronal annealing temperatures of Al-0.025 at.% Cu, Al-0.025 at.% Bi, Al-0.025 at.% Pb and Al-0.025 at.% Sb alloys quenched from 520 °C to ice water.

In case of the alloy that contains 250 ppm antimony, a considerable amount of vacancies bind the solute atoms immediately after quenching. This can be noticed from the increase of the intensity ( $I_2$ ) to about 60%. However, the recovery happens very fast, the average positron lifetime reaches the bulk value after annealing only at 50 °C, which means fast vacancies release. This is however, in strong contradiction to *Wolverton* calculations of Sb-vacancy binding energy ( $\sim 3\text{eV}$ ). It might be that *Wolverton* calculations are not accurate, since he used



quite small supercells of only 64 atoms, which may lead to a finite size effects, and thus overestimate the solute-vacancy binding [200]. Moreover, the weak interaction between the vacancies and the solute atom may attributed to the low solubility of Sb in Al matrix ( $< 0.01\%$ ) [222], so only low vacancy concentration binds the antimony atoms. It is shown that higher energy (i.e. temperature) typically results in higher concentration of the thermal vacancies (see figure 4.2), thus one can expect that the concentration of quenched-in vacancies should be higher when quenching occurs from higher temperatures. Slightly higher thermal vacancies are generated when the alloys are quenched at 620 °C to ice water. However, the recovery starts also early. One can notice the steep decrease in the intensity  $I_2$  (figure 5.8). It seems that the binding energy to quenched-in vacancies of Cu, Pb and Bi is very small, and hence their complexes are not thermally stable at  $T \geq RT$ . Consequently, the influence of binding energies should be studied at quite low temperatures. The alloys were quenched to lower temperature ( $\sim -100$  °C) to check the thermal stability of the vacancies and their concentration below RT.

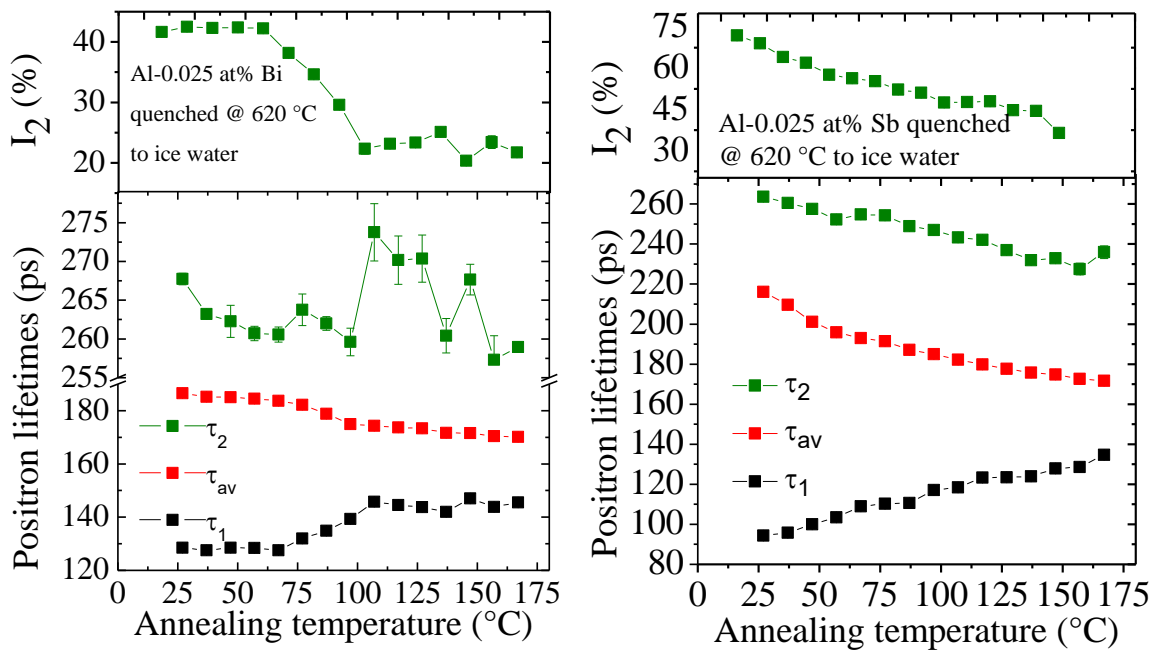


Figure 5.8: Positron lifetimes in Al-0.025 at.% Bi and Al-0.025 at.% Sb alloys as a function of isochronal annealing temperatures. The alloys were quenched from 620 °C to ice water.

### 5.3.2.2 Quenching the binary alloys at low temperatures (~ -110 °C).

The alloys are quenched to -110 °C in order to freeze vacancies and prevent them from the very fast migration to the sinks. This low temperature can be achieved by using freezing mixtures. The mixtures are often made from a mixture of liquid nitrogen or dry ice with an organic solvent; liquid nitrogen forms a slush. The viscosity of this slush depends on the solvent [224]. A temperature of -110 °C can be maintained by slowly adding liquid nitrogen to ethanol in an isolated container until it begins to freeze (ethanol freezes at -116 °C) [225]. The samples are homogenized in the two zones furnace for 2 hours and then quenched in the cooled alcohol, where the sample-source sandwich is done.

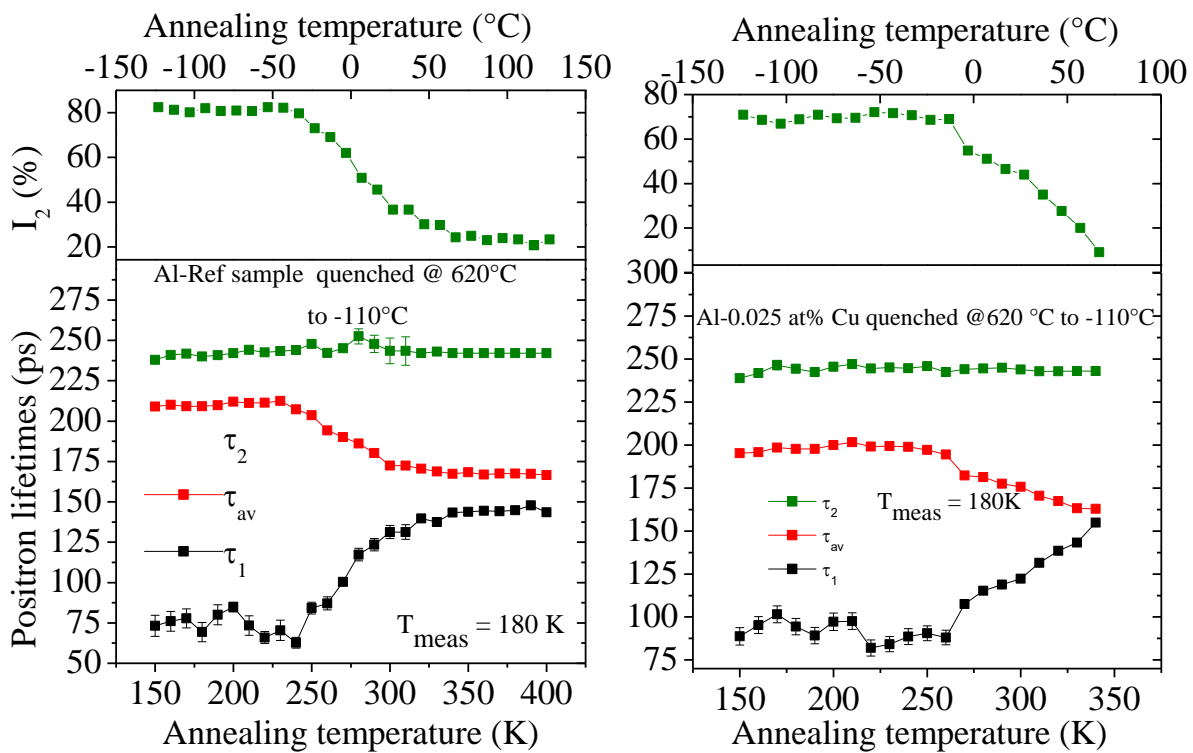


Figure 5.9: Positron lifetimes vs the isochronal annealing temperatures of the aluminum reference sample and Al-0.025 at.% Cu quenched from 620 °C to -110 °C, measuring temperature is 180K.

A well annealed high purity aluminum (99.9995 %, 5N5) has been used for comparison. The aluminum Reference is quenched at 620 °C to -110 °C and directly mounted into the measurement place to be isochronally annealed. After each annealing step, positron lifetime is measured at 180 K (~ -90 °C) to ensure that the quenched-in vacancies are not mobile. It is observed that the concentration of the generated quenched-in vacancies is high compared to the quenching to ice water. Figure (5.9) shows the positron lifetimes as a function of the annealing temperatures. The Average positron lifetime remains at higher values (~ 210 ps)

and the annealing of the vacancies starts at 240 K (~ -25 °C), this is in a good agreement with *linderoth et al.* [226]. At temperatures higher than 320 K (~ 50 °C), the vacancies are trapped by dislocations forming prismatic dislocation loops. This is also clear from defect-related lifetime ( $\tau_2$ ) and its intensity ( $I_2$ ). Comparing to the sample that quenched to ice water (vacancy-clusters 350-400ps with only 15% intensity, figure 5.5), single vacancies with nearly constant lifetime  $\tau_2 = 242$  ps and high intensity ( $I_2 = 80\%$ ) are observed (see figure 5.9).

Similarly, the rest alloys (Al-0.025 at. % Cu, Bi, Pb and Sb) are quenched to -110 °C. In case of Al-0.025 at. % Cu, the alloy behaves typically as the aluminum reference, which confirms that almost no binding between Cu atoms and the vacancies. This agreed well with *Wolverton* calculation ( $E_b$  of Cu = 20meV) [50]. Figure (5.9) shows a defect-related lifetime  $\tau_2 = 244$  ps with high intensity ( $I_2 = 80\%$ ), which is related to single vacancies in aluminum. This value is 10 ps more than that of the positron lifetime of Cu-V complex calculated by *O. Melikhova et al.* [227].

The binding between vacancies and the solute atom is clear in the other alloys, Al-0.025at% Sb, Pb, Bi. The average positron lifetimes stay at higher values (195-210 ps) and the annealing stages start almost at RT (300 K). The defect-related lifetimes for all alloys are higher than that of the characteristic positron lifetime for isolated mono-vacancies (240ps). This was not expected for large solute atoms (larger than Al atom). The solute atoms were expected to decrease the open volume of the neighboring aluminum vacancy [200] and hence, the positron lifetime of the solute-vacancy complex should be slightly lower than that of single vacancies as *Gebauer et al.* showed for Te-doped GaAs [65]. Positron lifetimes of about  $255 \pm 5$  ps are obtained for the three alloys (with 60% intensity). These values probably return to binding of one solute atom with two vacancies instantly after quenching [200] (figure 5.10).

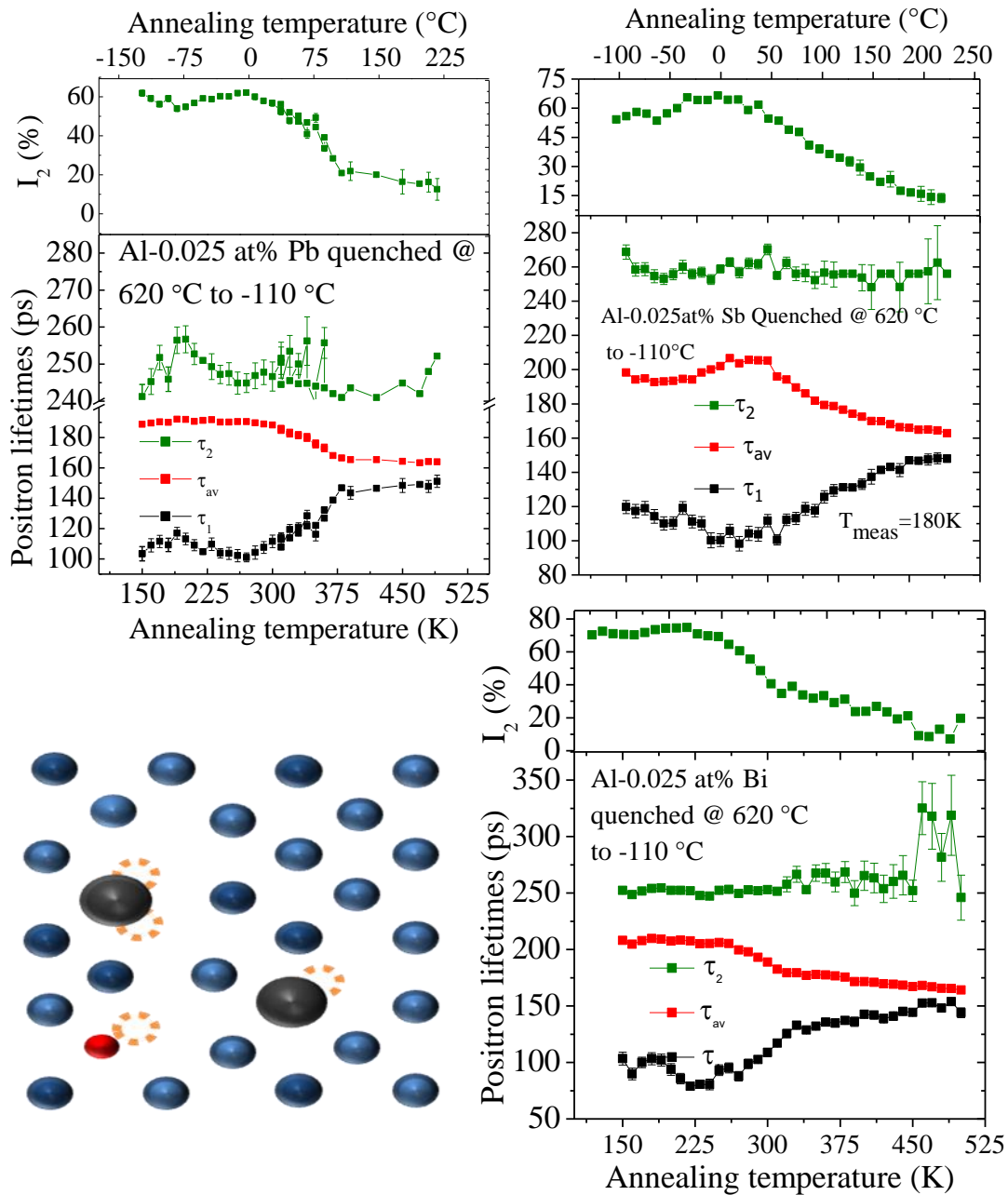


Figure 5.10: Positron lifetimes in Al-0.025 at.% Sb, Pb and Bi alloys quenched from 620 °C to -110 °C. The positron lifetimes were measured as a function of isochronal annealing up to 200 °C. The measurement temperature is 180K after each annealing step. The schematic diagram illustrates the binding between solute atoms with vacancies.

### 5.3.2.3 Al-0.025 at. % In quenched at 520 °C to ice-water (~ 0 °C)

The behavior of tin and indium as trace elements is completely different. Figure (5.11) shows two quenched aluminum-indium alloys with 50 and 250 ppm indium at 520 °C. It is obvious that the two alloys have nearly the same behavior for all positron lifetimes and their intensities. Therefore, Al-0.025at.% In will be only described.

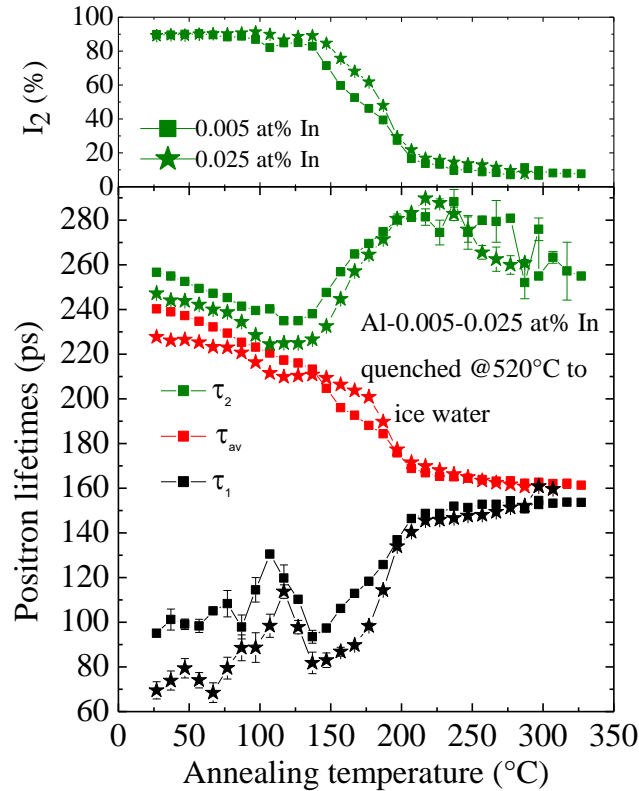


Figure 5.11: Positron lifetimes vs isochronal annealing for Al-0.025at.%In binary alloy quenched at 520 °C to ice water

The average positron lifetime for the as-quenched sample (at 27 °C) is about 228 ps. This value is much higher than that obtained for Al-5N5 (170 ps). After quenching, vacancies do not escape to the nearest sink as in quenched pure Al, but this vacancy loss will be delayed by the solute atoms. Indium atoms bind vacancies temporarily and form V–In complexes (act as positron traps) owing to their attractive interaction [171, 191, 200]. The average positron lifetime begins to decrease in two stages; firstly, it reaches 209 ps at 117 °C and remains constant up to 137 °C. After that,  $\tau_{av}$  decreases exponentially with increasing the annealing temperature. The recovery stage completes at about 300 °C ageing; all vacancies are separated from the solute atoms ( $I_2$  approaches 0) and the average positron lifetime reaches finally the bulk value.

The behavior of the defect-related lifetime  $\tau_2$  is very similar to  $\tau_{av}$  up to annealing at 117 °C, almost complete capture of positrons ( $I_2 = 90\%$ ).  $\tau_2$  for the as-quenched sample is about 247 ps. This value is higher than that of the characterized lifetime of a single vacancy, 240 ps. As it is mentioned above, the lifetime is expected to be lower than 240 ps in case of large solute atomic size [65], therefore most likely corresponds this value to solute-divacancy complex. *Dlubek et al.* found the same behavior in Al-Si alloy [228]. With further annealing, one of the two vacancies (the weaker bound) might be uncoupled leaving behind solute-vacancy complex. This can be observed from the value of  $\tau_2$ , which decreases until reaches 225 ps at 127 °C. On the other hand, this value of  $\tau_2$  (225 ps) may attributed to the precipitation of In atoms close to the In-vacancy pairs, which leading to an increase of the electron density in the vicinity of the complex, and thus decrease the positron lifetime (See figure 5.12 below).

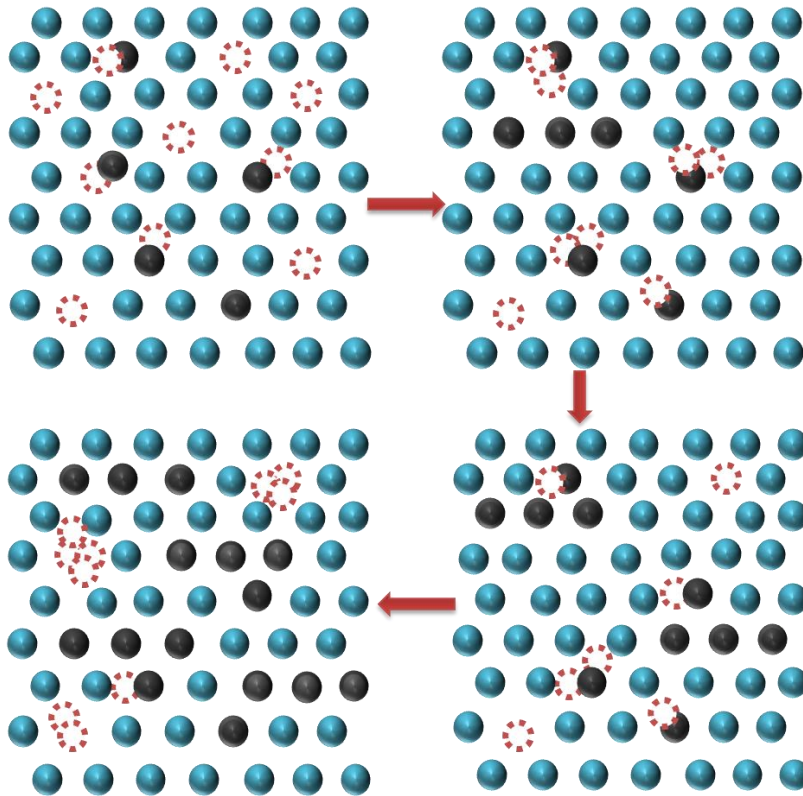


Figure 5.12: Schematic description of the solute-vacancy binding at solutionizing temperature, after quenching, and at artificial ageing. Blue: Al atoms; black:solute atoms; Dashed empty circles: vacancies ( from [223]).

At anneal temperature above 150 °C,  $\tau_2$  increases again up to 289 ps. The reason for that may attributed to the sufficient thermal energy, which allows the vacancies to become mobile. This is clear from scanning transmission electron microscope (STEM) images and the energy-dispersive X-ray (EDX) (figure 5.13). The indium atoms are now free and gather in small

spherical precipitates [200]. STEM images show a homogeneous distribution of In-rich particles with a size between 2 and 5 nm only. The mobile vacancies in turn diffuse with high concentration through the Al-matrix forming either a vacancy cluster or interact with each other forming divacancies. This vacancy cluster finally starts to anneal at 227 °C to sinks (expressed by  $I_2$  reduction ~15%), and finally no more detection of defects at about 300 °C.

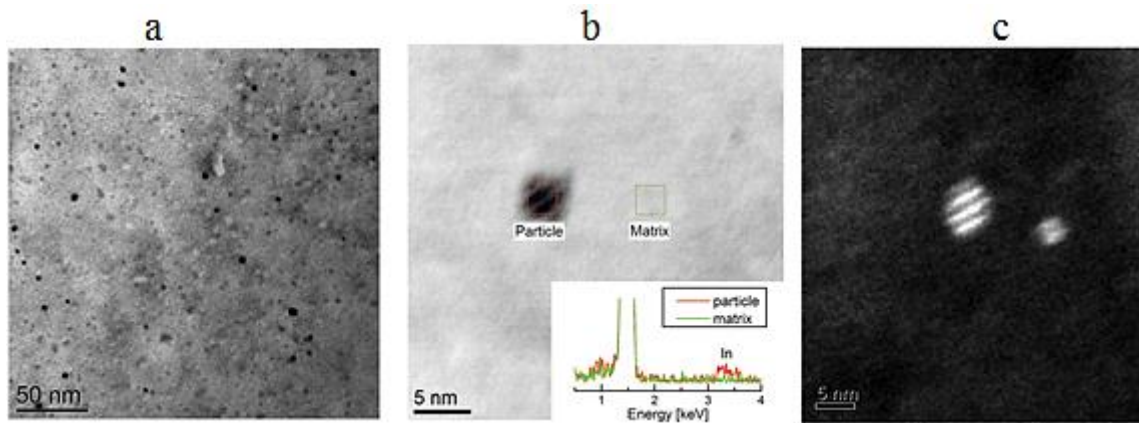


Figure 5.13: STEM and EDX-analysis of Al-0.025at%In alloy quenched at 520 °C to ice water and then aged at 150 °C for 1 h with different magnification and brightness [200].

Nevertheless, coincidence Doppler broadening spectroscopy will give us more information, (figure 5.14 below). The signature of In-atoms ( $5-15 \times 10^{-3} m_0c$ ) indicates that the quenched-in vacancies are localized nearby them. By comparing positron lifetimes values with CDBS, one can notice that for the as-quenched sample at RT, the In signal is not high. This corresponds mainly to two vacancies bind one indium atom (V<sub>2</sub>-In),  $\tau_2 = 247$  ps with intensity about 90%. Thereafter, at 127 °C, In- signal increased due to the detachment of one vacancy (V-In) in addition to the precipitation of In atoms around the vacancies,  $\tau_2 = 225$  ps with nearly the same intensity, 90%. At 227 °C ageing, In- signal decreased, which reflects the outset of the vacancy cluster,  $\tau_2 = 289$  ps (divacancies) with intensity 15%. The signal is very similar to Al-Ref.



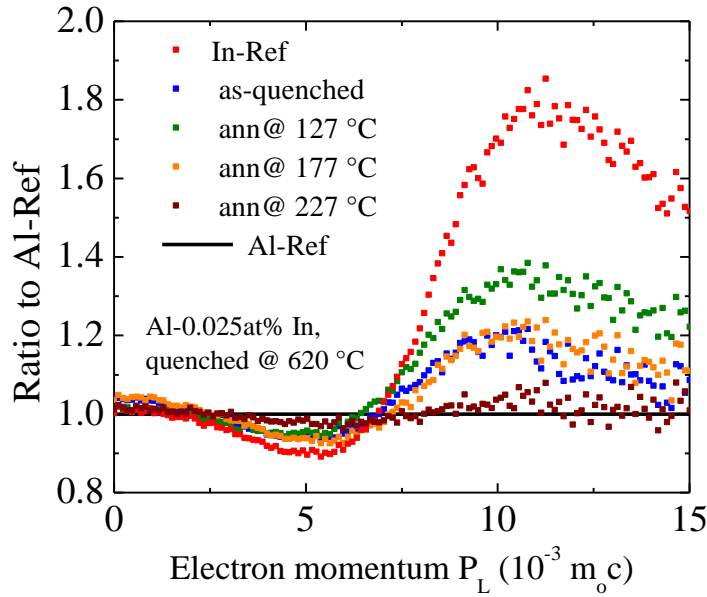


Figure 5.14: Coincidence Doppler broadening spectra of Al-0.025 at.% In. The signature of pure indium is clear.

**Effect of different quenching temperatures on the defect formation**

Solubility of In atoms in Al-matrix reaches its maximum at temperatures close to aluminum melting point, 0.045 at 640 °C [229]. The figure below illustrates the behavior of positron lifetimes in Al- 0.025at.%In at different quenching temperatures. One can observe that the recovery stage is difficult to be recognized with increasing the quenching temperature to 570 °C.

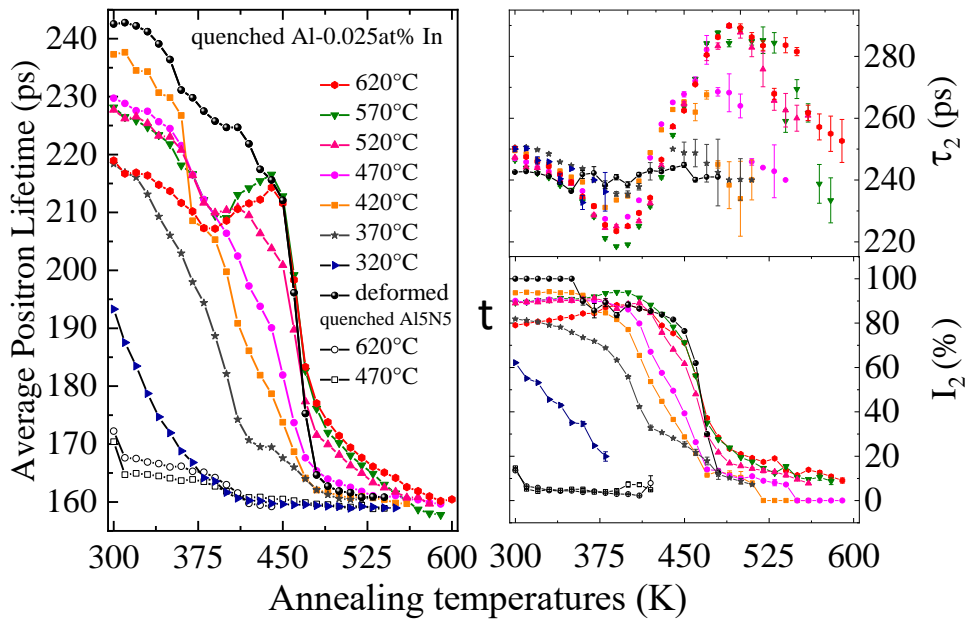


Figure 5.15: Positron lifetimes as a function of annealing temperatures for Al-0.025at.% In quenched from different temperatures. The quenched alloy is compared to a deformed one.



The value of  $\tau_{av}$  starts with 246 ps, then it decreases to 218 ps. It increases again between 390 K (117 °C) and 440 K (167 °C), which reflects vacancy clusters formation. Moreover,  $\tau_2$  is not constant and still increasing, which corresponds to a change in the existing defect structure (since the intensity  $I_2$  remains high). By reaching annealing temperature of about 450 K (177 °C), the clusters begin to anneal out ( $I_2$  start to decrease). There is no clustering during the annealing process at low quenching temperatures. It is noticed that the average positron lifetime of  $T_Q = 420$  °C ( $\tau_{av} \sim 237$  ps) at RT is larger than that of  $T_Q = 520$  and 570 °C (228 ps).

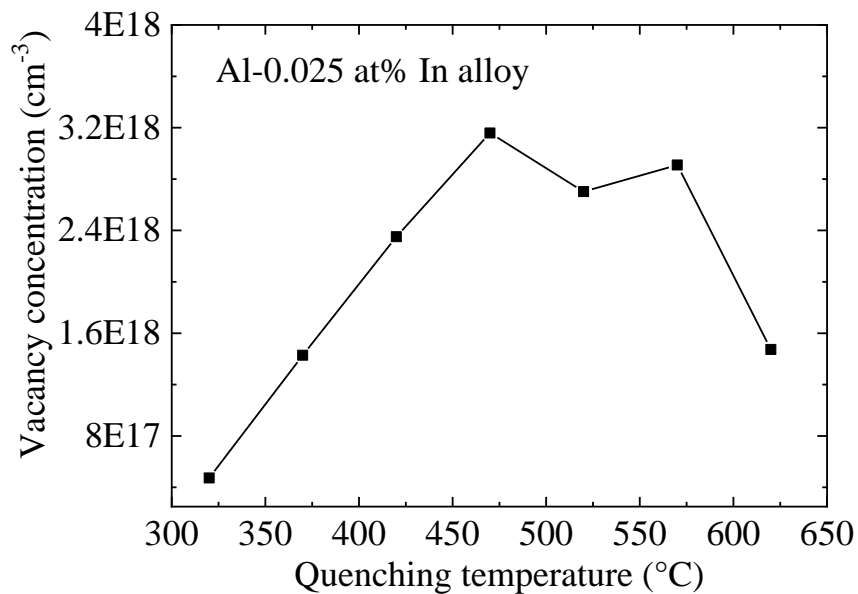


Figure 5.16: Vacancy concentration as a function of quenching temperature in Al-0.025 at.% In .

Furthermore, the defect concentration  $C_V$  in Al-0.025 at% In alloy increases with increasing quenching temperature up to 470 °C (see figure 5.16). However, with further increase of quenching temperature,  $C_V$  is decreased again. This indicates that 500 °C is a critical quenching temperature for the vacancy concentration. This does not agree with the simple trapping model; at higher quenching temperatures may be more than one type of defects. Nevertheless, the average positron lifetime decreased. In order to confirm the presence of the dislocations at higher quenching temperatures, figure (5.15 and 5.17) compare the behavior of the positron lifetimes and the positron trapping rate in the quenched and deformed alloy. At lower annealing temperatures, the deformed sample showed complete trapping and the trapping rate is very large (therefore, not included in the plot). The quenched temperature of about 420 °C shows the highest trapping rate immediately after quenching. The trapping rate

decreases with increasing quenching temperatures during the entire annealing process except between 390 K (117 °C) and 440 K (167 °C), which may return to the formation of a vacancy clusters. The reason for the lower value of the average positron lifetime despite of high quenching temperatures may return either to the dislocations resulted from quenching process [169] or the precipitation of more indium atoms, which act as vacancy sinks.

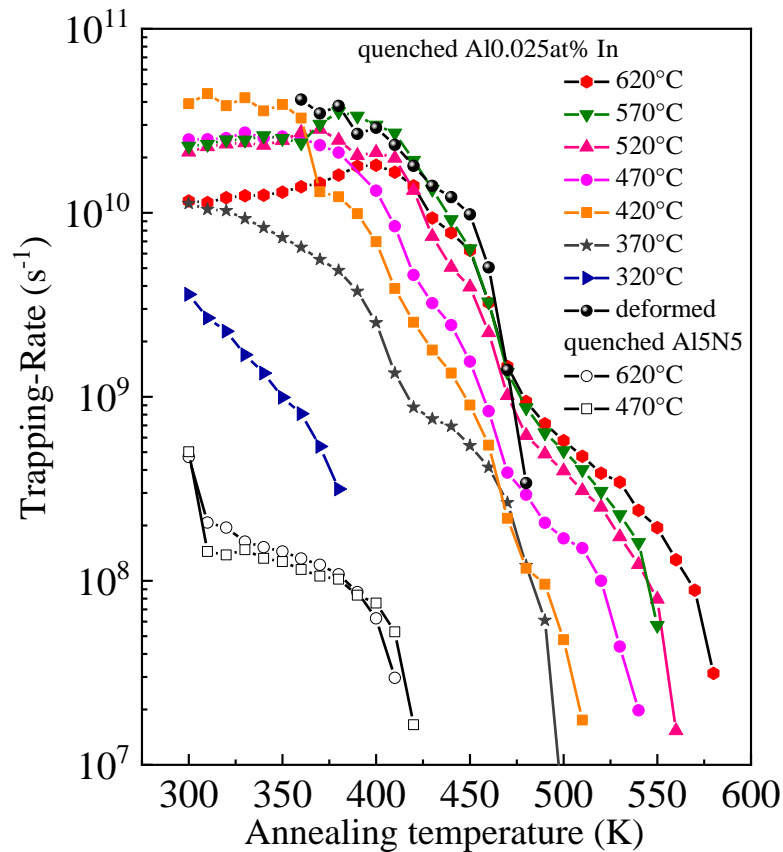


Figure 5.17: Positron trapping rate as a function of annealing temperatures for Al-0.025at.% In quenched from different temperatures. The quenched alloy is compared with a deformed one.

The comparison between the measured and the calculated reduced bulk lifetime  $\tau_1$  (using simple trapping model) is shown in figure 5.18. The calculation agrees well with the measurement for the low quenching temperatures over the entire annealing process (figure 5.18). The reason for this might be the low dislocation density, which causes mainly just one defect type in the material, and thus the simple trapping model coincides with the measurement. At higher dislocation and defect concentrations, the model is only correct with the measurement at the annealing temperatures of about 400 K (127 °C) - 450 K (177 °C). Accordingly, quenching the samples from temperatures higher than 500 °C may generate dislocations, and thus the vacancy concentration decreased.

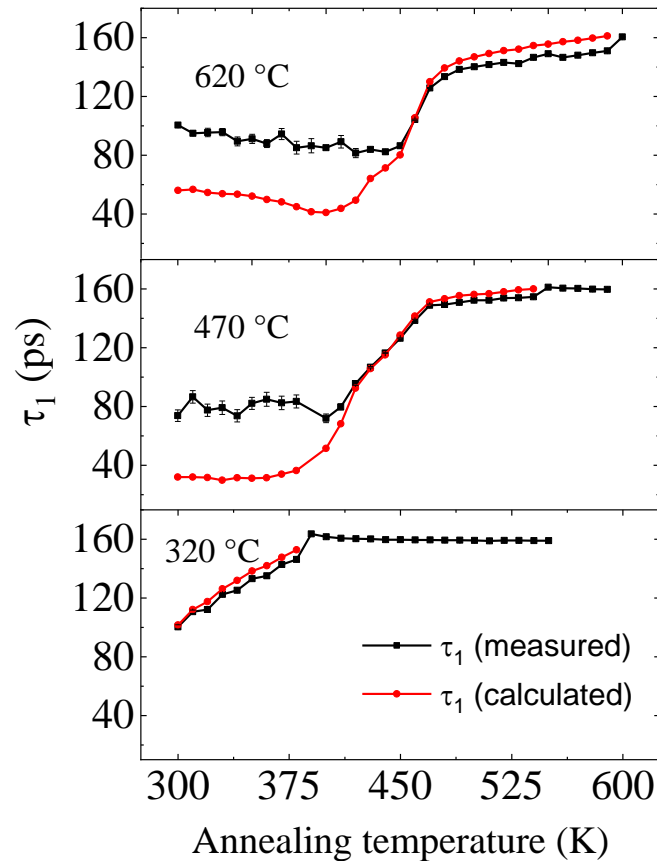


Figure 5.18: Comparison between measured and calculated positron reduced bulk lifetime (using simple trapping model) for different quenching temperatures.

However, this behavior was not observed in the deformed sample or in similar alloys, i.e. Al-0.025at%Sn; it is observed for the sample with indium at only  $T_Q > 500$  °C. Therefore, the generation of dislocations at  $T_Q > 500$  °C is excluded; this behavior might be attributed to the solubility of indium. It is expected that In solubility in Al-matrix reaches a maximum at temperatures lower than 500 °C. This is probably above the solution phase, and thus the concentration of In decreases slightly. This means that the concentration of In-vacancy complexes decreases ( $\tau_{av}$  and  $I_2$  reflect that at  $T_Q > 500$  °C); 500 °C is mostly the boundary of the solid solution phase. At temperatures higher than 500 °C, the boundary of the solution phase is exceeded and some In atoms start to precipitate, and thus the concentration of V-In complexes decreases.

#### 5.3.2.4 Al-0.025 at. % Sn quenched at 520 °C to ice-water

The positron lifetimes behavior of Al-Sn alloy is very similar to that in Al-In alloy. Figure (5.19) shows quenched aluminum-tin alloys with 50 and 250 ppm tin at quenching

temperatures 520 °C to ice water. The average positron lifetime  $\tau_{av}$  of  $235 \pm 5$  ps is recorded in the as-quenched sample and it remains constant up to 70 °C. This value indicates high defect concentration comparing to Al-5Ni (170 ps), which increases with increasing solution temperatures. The defect-related lifetime  $\tau_2$  is  $263 \pm 1$  ps and behaves very similar to  $\tau_{av}$  up to  $\sim 150$  °C, almost complete capture of positrons ( $I_2 \approx 85\%$ ).

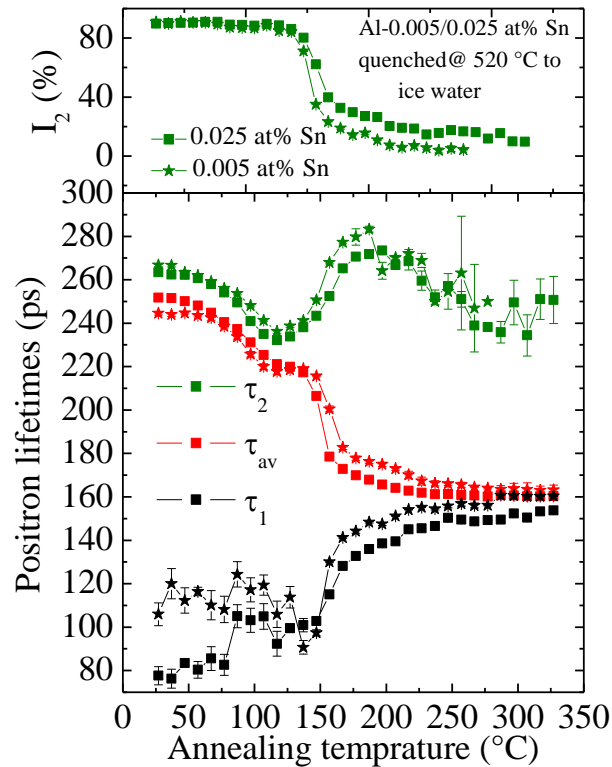


Figure 5.19: Behavior of positron lifetimes as a function of isochronal annealing for Al-0.025at.%Sn binary alloy quenched at 520 to ice water.

The defect-related lifetime values are far from the characteristic positron lifetime of mono-vacancies (240 ps) and di-vacancies (280 ps). It seems that tin atoms can be coupled to quenched-in vacancies forming solute-vacancy complexes with a relatively high binding energy. Binding energy of about 0.25 eV of Sn to the monovacancies was reported [50, 223, 227]. The vacancy-tin interaction was also studied by several authors; there are agreements among the authors that thermal vacancies can be bound to dissolve Sn atoms during the solution treatment. As a consequence, a significant amount of tin atoms can be coupled to vacancies after quenching at room temperature [230-234]. However, the values of  $\tau_2$  are expected to be lower than the characteristic positron lifetime of mono-vacancies. Probably, the high concentration of quenched-in vacancies leads to a mixture of defects, i.e. non-decorated vacancies (without solute atoms), solute-vacancy complexes, and/or solute-

divacancies complexes. Čížek *et.al.* calculated the positron lifetimes in different complexes; only Sn-divacancy has a positron lifetime bigger than that of monovacancies (240 ps) [73]. The alloy is then isochronally annealed; the average and defect-related positron lifetimes begin to decrease started from 70 °C. They recorded  $215\pm 3$ ,  $235\pm 3$  ps at 117 °C, respectively.

Let's assume the presence of Sn-divacancy complexes; with annealing the sample, one of the divacancy (the weaker bound) might be detached leaving behind solute-vacancy complex (similar to Al-In) [200]. Moreover, increase of the electron density nearby the complex due to precipitate of tin atoms leading to decrease the positron lifetime. After this local minimum,  $\tau_{av}$  increases slightly to 220 ps at anneal temperature of about 147 °C. After that,  $\tau_{av}$  decreases exponentially with increasing the annealing temperature. On the other hand,  $\tau_2$  starts to rise again until reach 275 and 300 ps at 520 °C and 620 °C, respectively. At higher temperatures, vacancies begin to couple together forming divacancies, since the number of jumps is much less than that needed to reach dislocations [221]. If the divacancies have a sufficient binding, they can live enough to form trivacancies and clusters. In order to decrease the total Gibbs energy of a system, this vacancy cluster finally succeed in reaching dislocations by increasing the number of jumps (and hence, decreasing the clustering). However, at lower temperatures more rapid dissociation occurs and thus, the energy is enough to form only divacancies; no cluster formation [221].

Comparing the measured and the theoretical calculation of coincidence Doppler broadening of solute-vacancies complexes will be helpful for recognizing the two stages [73]. Figure (5.20) illustrates the coincidence Doppler broadening measurement of 620 °C quenching temperature. The ratio profile of Sn deviates significantly from the straight line (that represents Al), indicating that the quenched-in vacancies are localized nearby tin atoms. By comparing positron lifetime values with CDBS, one can notice that, for the as-quenched sample at RT, the deviation of Sn from Al is not high and this corresponds to the binding between two vacancies with one tin atom (V<sub>2</sub>-Sn),  $\tau_2 = 264$  ps with intensity about 85%. Thereafter, at 117 °C, the Sn signal increased. The reason of that is the detachment of one vacancy (V-In) or the precipitation of Sn atoms around the vacancies,  $\tau_2 = 238$  ps with nearly the same intensity 85%. At 147 °C, the vacancies start to cluster around Sn atoms, which is clear from the reduction of the Sn signal. Finally, all vacancies are released from the solutes

and the cluster anneals at sinks,  $\tau_2 = 300$  ps (trivacancies) with intensity 10%. The signal is very similar to Al-Ref.

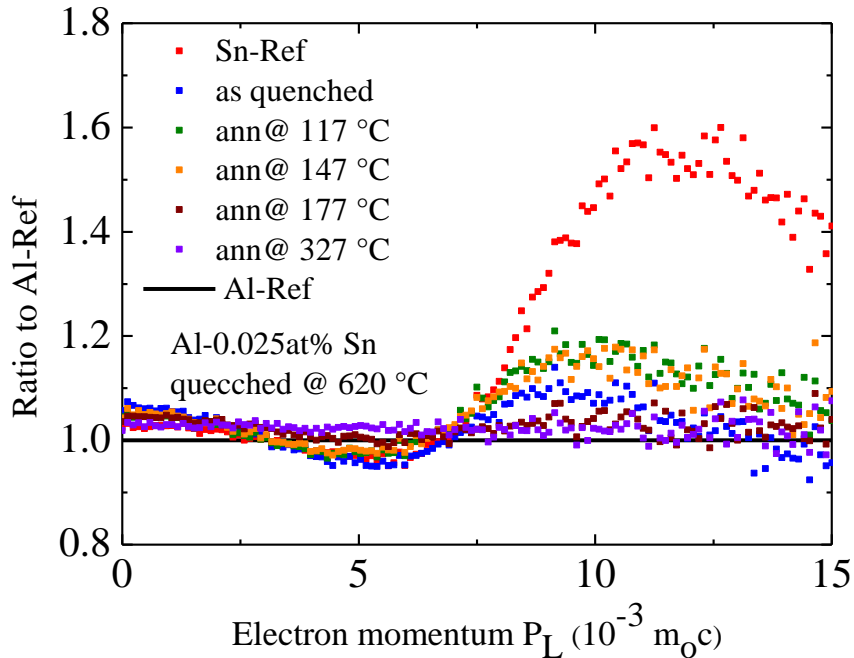


Figure 5.20: Coincidence Doppler broadening spectra of Al-0.025 at.% Sn in comparison to pure Al and pure Sn. The imprint of pure Sn in the alloy is clear.

### 5.3.3 Quenched-in vacancies in Al-1.7 at% Cu based alloys

The effect of adding some trace elements on the Al-1.7at%Cu alloy is studied. Quenched Al-1.7at%Cu binary alloy without trace elements is investigated firstly, and then compared to the alloy with some traces.

#### 5.3.3.1 Al-1.7 at% Cu binary alloy

Al-1.7 at% Cu binary alloy shows typical precipitations corresponding to GP zones [155] [156] and  $\theta'$  phase [191, 199]. This is evident from the positron lifetime measurement (figure 5.21).

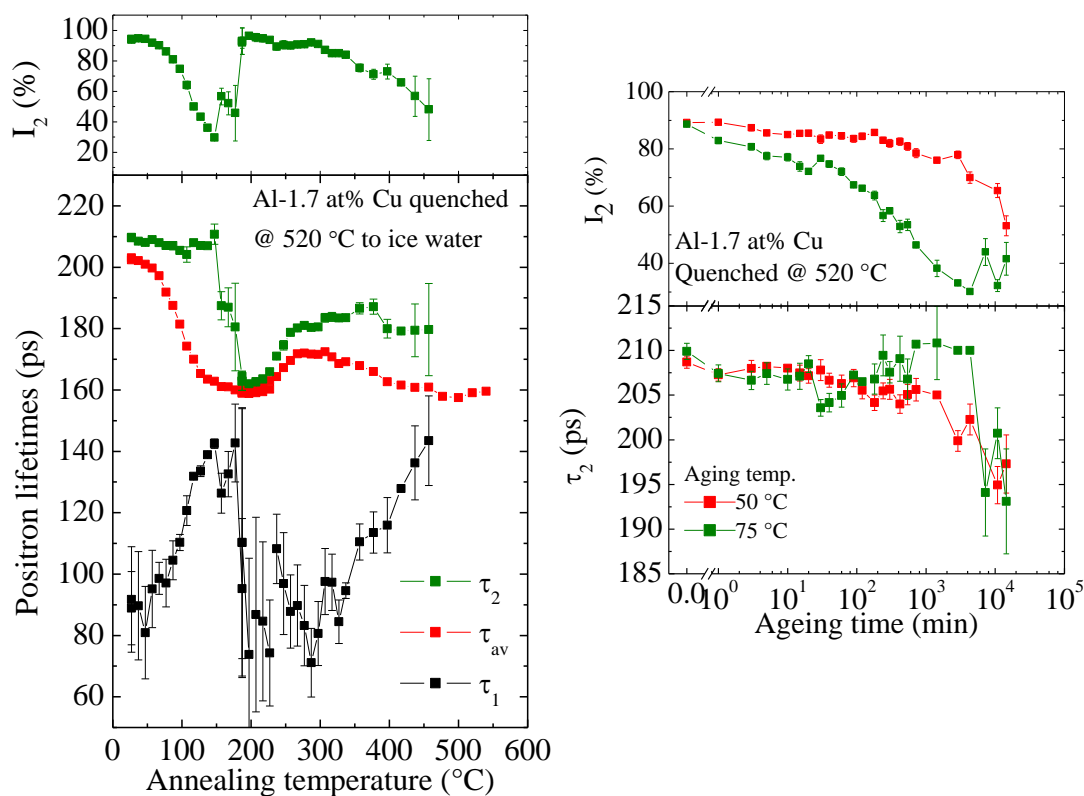


Figure 5.21: (Left) PALS measurement of quenched Al-1.7 at.% Cu at 520  $^{\circ}$ C to ice water. Sample has been isochronally annealed to 500  $^{\circ}$ C. (Right) PALS measurement of quenched Al-1.7 at.% Cu at 520  $^{\circ}$ C to ice water. Sample has been isothermally annealed at 50 and 75  $^{\circ}$ C.

The as-quenched sample shows a defect-related lifetime of about 209 ps with very high intensity. This value is too far from the bulk lifetime (158 ps), which means that positrons are trapped by a deep trap. *Dlubek* [235] found that even a few amounts of vacancies capable to trap positrons with almost 100 % probability. *Gläser et al.* [236] attributed that to positron annihilation in vacancies having considerable amount of copper atoms in their surroundings. *Gauster and Wampler* [237] ascribed that to a GP zone contains vacancies. Moreover, *Silcock* [210] showed that GP zones are formed in quenched Al-Cu alloy after 3 minutes at 30  $^{\circ}$ C [238]. Comparing this result to the ab-initio calculations of the positron annihilation parameters in the different precipitates [239, 240], one can observe a good correlation between the measured positron lifetime and the annihilation of positrons inside GP I zone containing a copper vacancy (see figure 5.22). It is apparent from the calculations that the positron lifetime is influenced significantly only if the vacancy is inside the Cu disk. When the precipitations have an open volume in their interior, positrons are trapped firstly by the surface potential, then by the deep one.

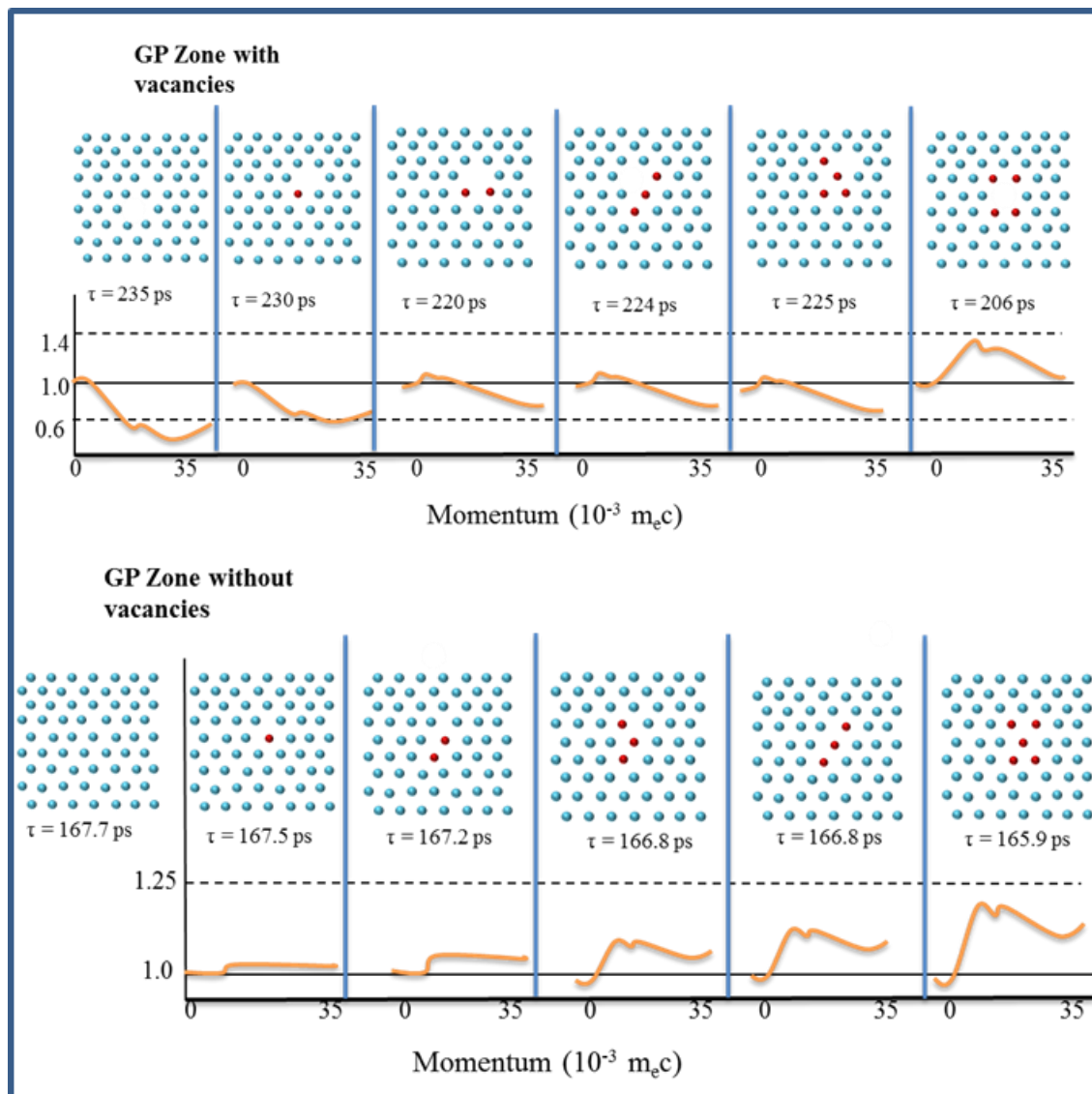


Figure 5.22: Calculated positron lifetimes and Doppler spectra of some atomic configurations representing early stages of GP zones with/without vacancies in Al lattice (from [239]).

The alloy is then isochronally annealed; the defect-related positron lifetime begin to decrease starting from ageing at 150 °C until it reaches 165 ps at about 187 °C. Copper atoms start to diffuse more and more towards the GP zone forming a multilayer of Cu (GP II/  $\theta''$ ), and thus the positron lifetime begins to go down [236]. This positron lifetime value matches very well with the calculated positron lifetime in the GP zone without any vacancies. Positrons can be trapped in pure GP zones, and they annihilate there from Bloch-like states spread out over the whole zone; positron sees GP zones as a bulk [235]. Further increase in the ageing temperature (higher than 200 °C) leads to nucleate of a new phase with characteristic positron lifetimes of about 181 ps, 190 ps at 277 °C, 350 °C, respectively. These values are in a good



agreement with calculated positron lifetime in  $\theta'$  precipitates without and with a vacancy on a Cu-sublattice (see figure 5.23).

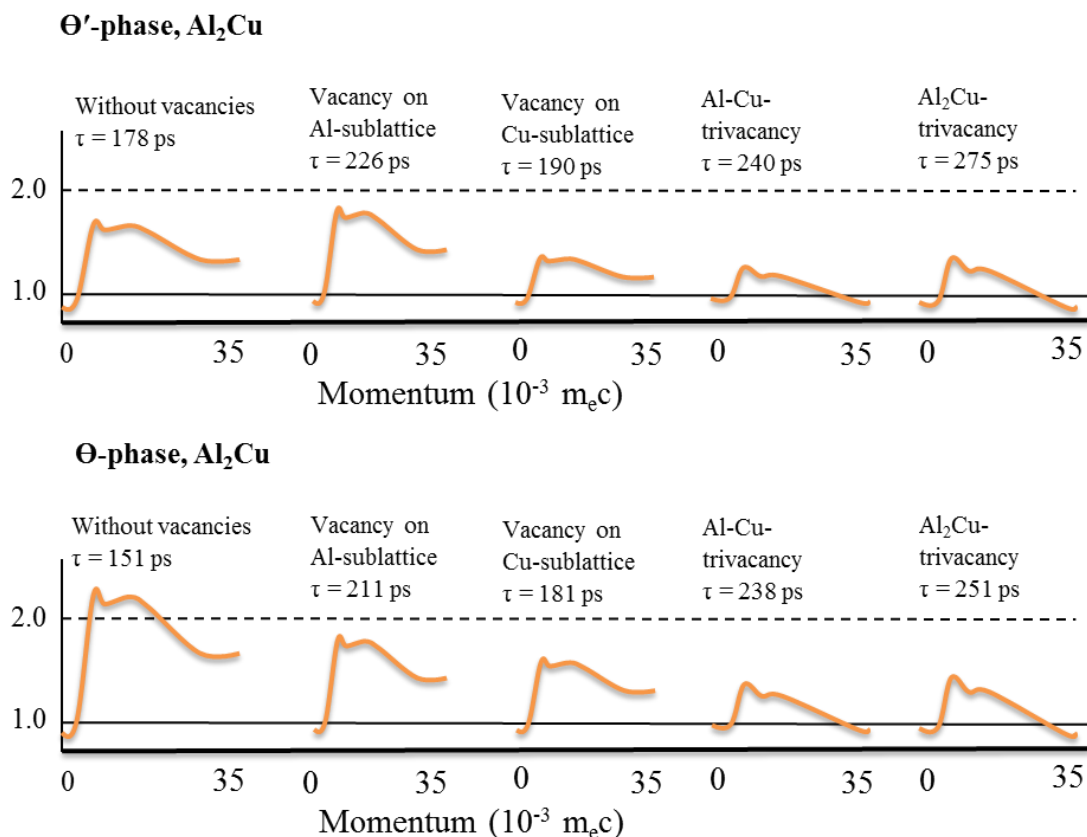


Figure 5.23: Doppler spectra of some atomic configurations representing  $\theta'$  and  $\theta$  with/without vacancies in Al lattice (from [239]).

$\theta'$  nucleation depends often on dislocations, i.e. they conjugate with Al-matrix via formation of a misfit dislocations [210]. Positrons are localized at the misfit dislocations of the  $\theta'$  phase. Finally, at annealing temperatures higher than 400 °C,  $\theta'$  precipitates are coarsen and  $\theta$  phase starts to appear; this lead to the decrease of  $I_2$  [236]. Positron lifetime records 180 ps, which correspond to annihilation in  $\theta$  phase with a Cu vacancy (according to the calculations [239]). By reaching 500 °C,  $\theta$  precipitates become fully incoherent with the host;  $\tau_2$  reaches the bulk value.

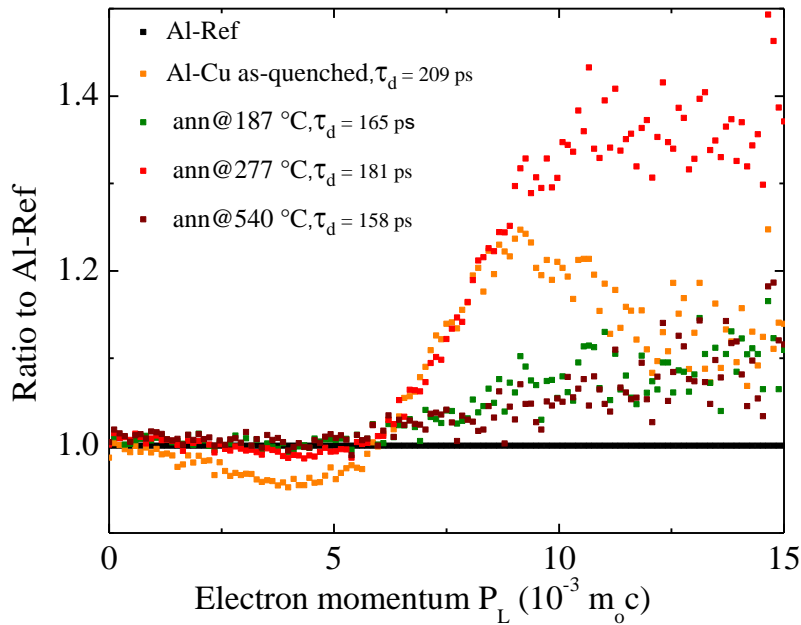


Figure 5.24: Coincidence Doppler broadening of Al-1.7 at.% Cu in comparison to pure Al.

CDBS gives us more evidence about the positron localization prior the annihilation (chemical information). The electron momentum distributions in Al-1.7at.% Cu alloy is measured. The spectra confirm the results obtained by positron lifetimes. The ratio profile of Al-Cu alloy deviates significantly from pure Al as it is shown in figure 5.24, which indicates the presence of Cu atoms in the environment of the vacancies at RT and after ageing. The momentum distribution is changing toward more Cu-rich environment. The orange curve represents the measured momentum of the as-quenched sample at RT. Comparing to the calculation (figure 5.23), the ratio to Al-Ref reveals the signature of the GP zone with a copper vacancy (ratio close to 1.4). At ageing temperature of about 187 °C, Cu atoms diffuse to the GP zone; this appears from the momentum distribution of the GP zone without any vacancies. With increasing the ageing temperature, more and more Cu atoms diffuse to the GP zone forming  $\theta'$  precipitates at 277 °C. The red curve represents the Doppler spectrum of  $\theta'$  precipitates.

On the other hand, the isothermal annealing of the alloy up to 1000h at 50 and 75 °C shows stability in  $\tau_2 = 205\text{-}210$  ps, which corresponds to annihilation in the GP zone with a copper vacancy (see figure 5.21, right). This result also confirmed by the high resolution TEM images. A high volume density GP I zone with a size between 3 and 6 nm is clear for naturally aged alloy ( $> 1000$  h at room temperature, see figure 5.25). By annealing the alloy at higher temperatures (150 °C), a mixture of  $\theta''$  and large  $\theta'$  precipitates present, having a size of 20-40 nm and 100-150 nm, respectively. Cu atoms start to diffuse out from  $\theta''$  leaving an

empty region of  $\theta''$  around  $\theta'$  phase.

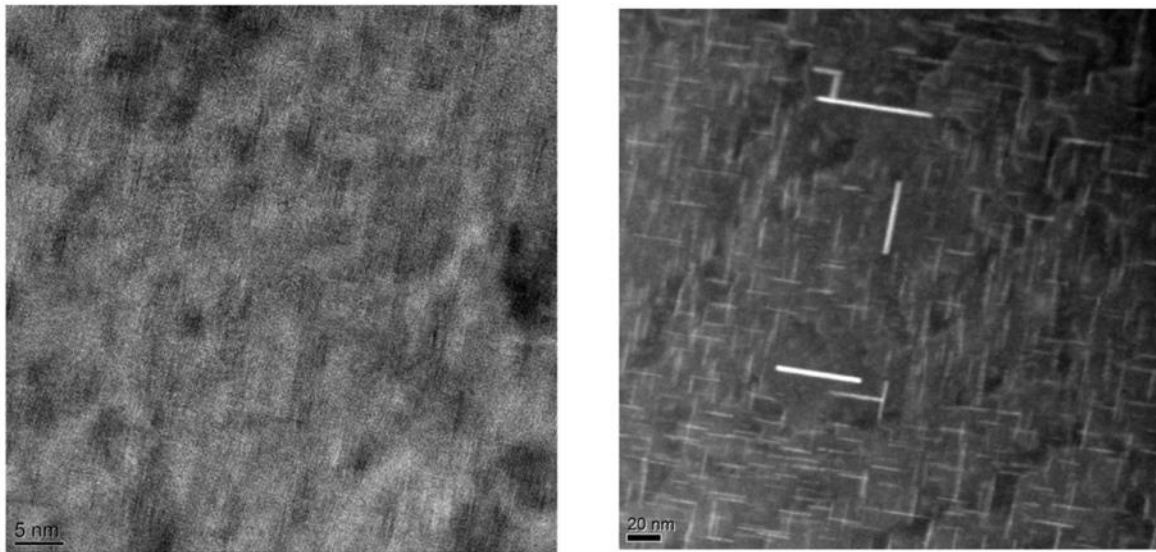


Figure 5.25: Left: High resolution TEM image of Al- 1.7 at% Cu naturally aged ( $> 1000$  h at room temperature). Right: STEM image of aged alloy at  $150\text{ }^{\circ}\text{C}$  for 48 h\*.

### 5.3.3.2 Al-1.7 at% Cu ternary alloys

#### Al-1.7 at% Cu-0.01 at% Pb, Sb

Figure (5.26) shows the influence of adding lead and antimony to Al-1.7 at.% Cu alloy on the positron lifetimes. It seems that there is no significant effect of Pb or Sb on the alloy. Three stages are appeared during the annealing; first one corresponding to the positron trapping from copper precipitates (GP zone with copper vacancies); the positron lifetime is about 210 ps. The second stage reveals the presence of  $\theta'$  precipitate starting from ageing temperature of  $170\text{ }^{\circ}\text{C}$ ; positron lifetime is 177 ps (correspond to annihilation in  $\theta'$  phase). With increasing the annealing temperature, the defect-related lifetime increases again until reaches 187 ps at temperature higher than  $230\text{ }^{\circ}\text{C}$ . This gives indication that positrons annihilate in  $\theta'$  phase containing a copper vacancy, since copper atoms start to diffuse out from  $\theta'$  phase.

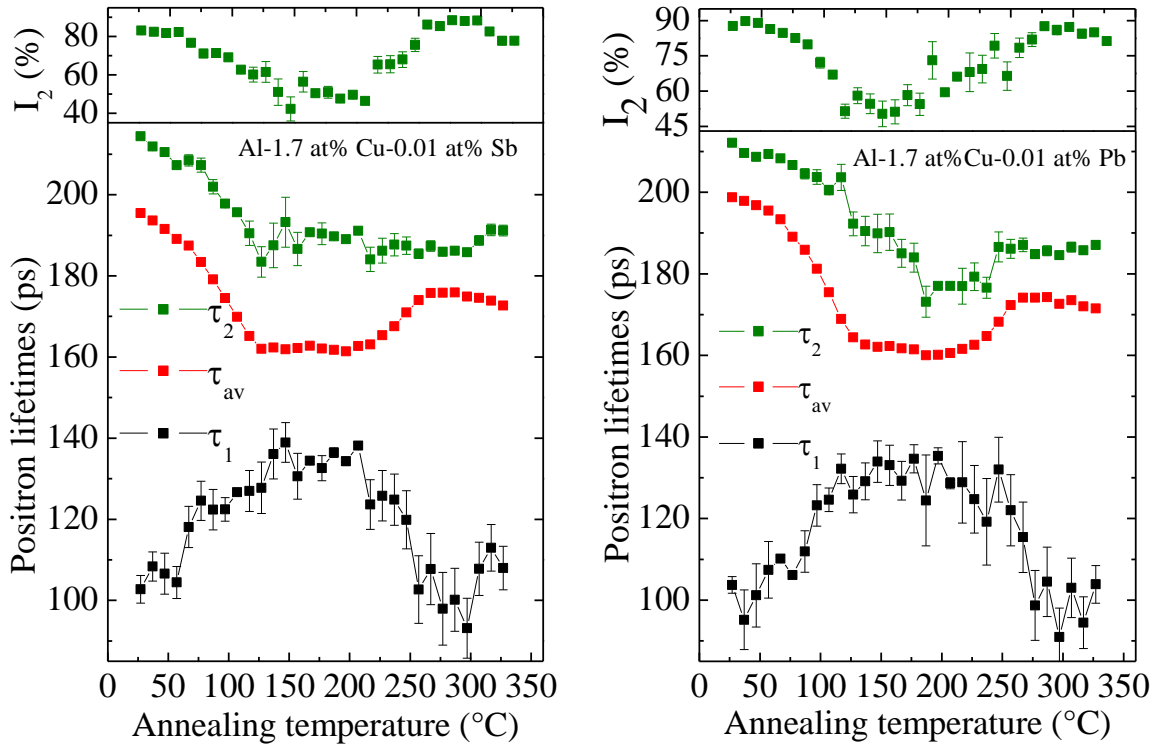


Figure 5.26: Positron annihilation lifetime measurement of quenched Al-1.7 at.% Cu with 100 ppm Pb and Sb as a function of isochronal annealing up to 350 °C temperature.

Figure (5.27) shows the differential scanning calorimetry thermograms\* of the as-quenched Al-Cu binary and ternary alloys. The thermograms show several exo- and endothermic peaks, referring to the formation and the dissolution of precipitates containing Cu. There is no big difference between the alloys with and without lead (Pb) can be noticed. This is also another evidence that Pb atoms have a weak interaction with the quenched-in vacancies [222, 223].

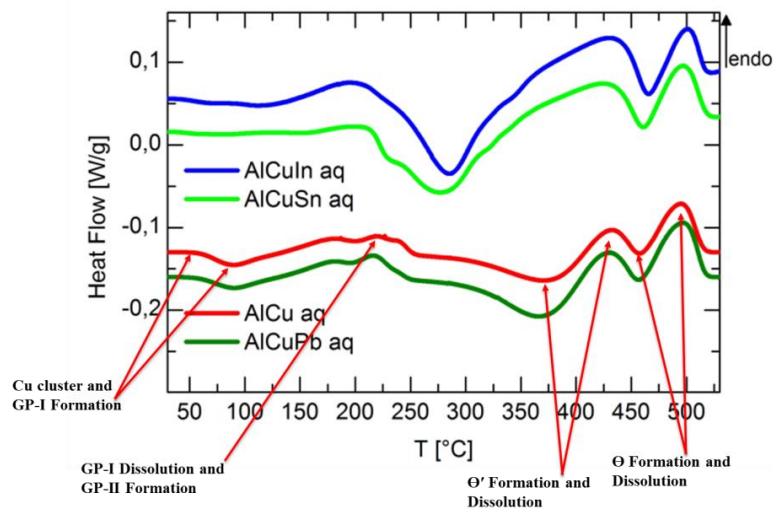


Figure 5.27: DSC curves for as quenched Al-1.7 at.% Cu alloy with 100 ppm Sn, In, Pb measured directly after quenching to ice water from 520 °C.

\*Done by Dr. Staab, Torsten Würzburg University.

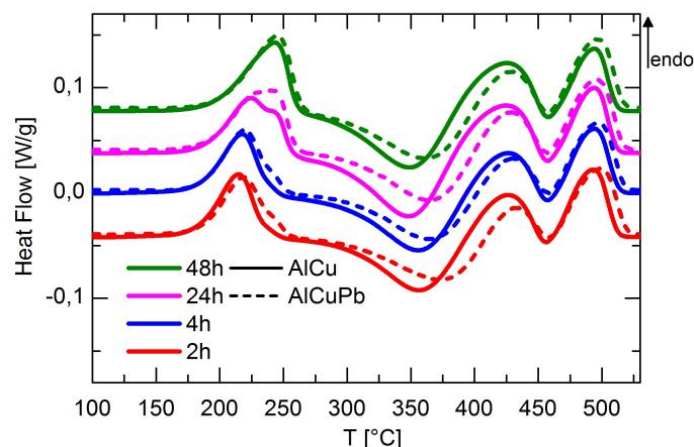


Figure 5.28: DSC curves for the aged Al-1.7 at.% Cu alloy without and with 100 ppm Pb. The two alloys have been quenched to ice water from 520°C.

DSC curves of the aged Al-Cu and the Al-Cu-Pb alloys show also only a minor difference (figure 5.28). Ageing at 150 °C resulted in many exo- and endothermic peaks indicating the formation and the dissolution of Cu-precipitates. Major dissolution peaks are clear in both alloys. The first dissolution peaks represent GP-I and GP-II zones, which have formed during ageing. This confirms clearly the minor or the negligible influence of lead on the diffusion of quenched-in vacancies in Al-Cu alloy.

### Al-1.7 at% Cu-0.01 at% In, Sn

Positron lifetimes of the Al-1.7 at% Cu alloy with a small amount of indium and Tin as trace elements (100 ppm) are shown in Figure (5.29). In and Sn atoms change the whole picture, the behavior is completely different from Al-1.7% Cu binary alloy. Al-1.7 at% Cu-0.01 at% In, Sn samples show nearly the same behavior as the binary alloys Al-In and Al-Sn up to 250°C ageing temperatures. In the temperature range below 100°C, the solute atoms bind divacancies forming solute-divacancy complexes; this has been already explained above. The as-quenched Al-1.7 at% Cu with 100 ppm In or Sn showed a defect-related positron lifetime of about 250 and 240 ps respectively. These values on one hand are very similar to the values of Al-In and Al-Sn binary alloys and on the other hand quite different from the lifetime of Al-Cu and Al-Cu-Pb/-Sb alloys. This implies that In and Sn atoms suppress the formation of GP zones at RT by preventing the diffusion of Cu atoms, i.e. by binding the quenched-in vacancies, which help Cu atoms to diffuse.

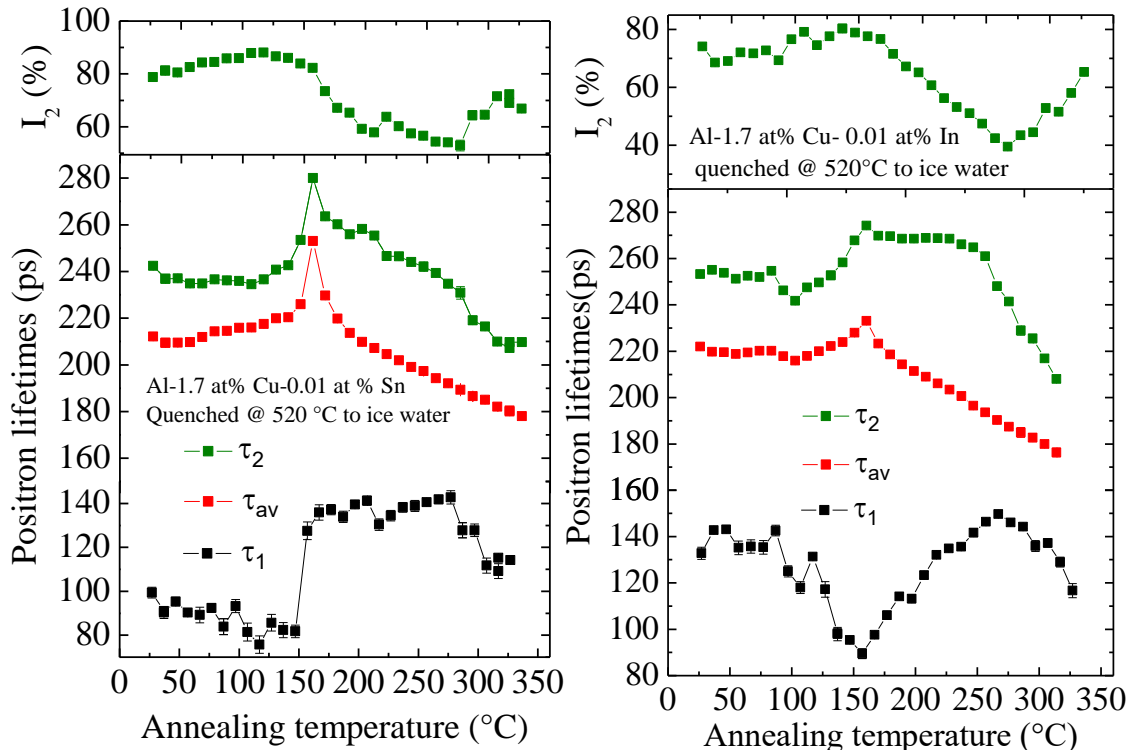


Figure 5.29: Positron lifetimes of as quenched Al-1.7 at.% Cu with 100 ppm Sn and In as a function of isochronal annealing temperature up to 327°C. The quenching temperature is 520°C.

This is also obvious from the DSC curves in figure 5.27 (blue and white green curves), the dissolution peak of Cu clusters and /or GP-I zones is missing since the Cu diffusion is significantly suppressed. However, the diffusion of Cu atoms is not totally blocked at room temperature when the alloys are naturally aged; the dissolution peak becomes more notable after 4 hours natural ageing (figure 5.30).

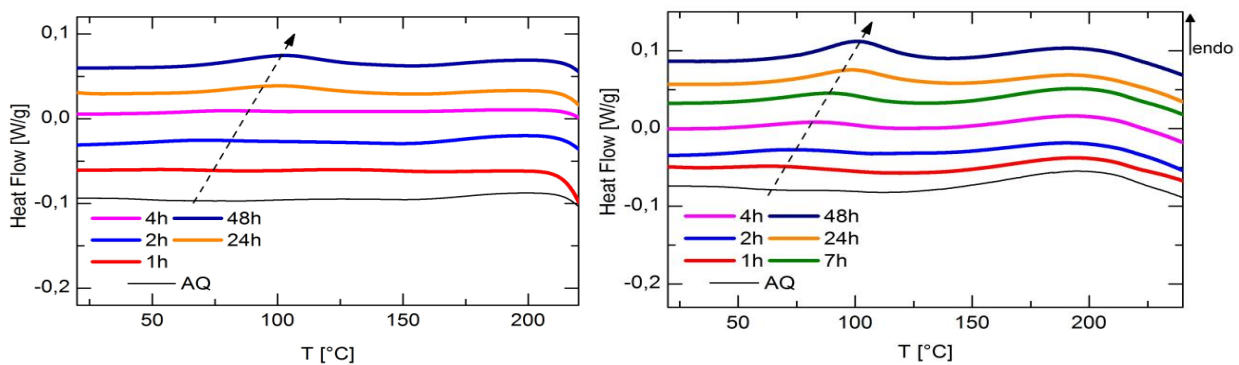


Figure 5.30: DSC curves for naturally aged Al-1.7at.%Cu-0.01at.%Sn (Left) and Al-1.7at.%Cu-0.01at.%In (Right).

Annealing the alloys between 120°C and 150°C lead probably to the separation of the weak bound vacancies, this appears in the value of  $\tau_2$ , which decreases to 240 ps (fig. 5.29). This behavior is noticed only for In containing alloy, however the detachment of the vacancy from Sn-divacancy could happened much earlier at lower temperatures [200]. Thereafter, at about 167°C most of vacancies have enough energy to leave the solute atoms (separation from In or Sn atoms) and they agglomerate, cluster together, and move to sinks. This is evident from increasing  $\tau_2$  and decreasing its intensity. At elevated temperatures above 250°C, the positron lifetime  $\tau_2$  begins to go down (figure 5.29), while the corresponding intensity  $I_2$  rises again. It seems that a new trap of positrons presents with a characteristic positron lifetime; this is most probably due to the formation of  $\theta'$  phase. This is assured by comparing the measured lifetime  $\tau_2$  with the ab-initio calculations of positron annihilation in  $\theta'$  phase (figure 5.23) [240]. The formation temperature of  $\theta'$  precipitates is changed to be at 250°C and this is 100°C more than that of Al-Cu binary alloy. This is also obvious from the DSC curves in figure (5.31). Furthermore, when the samples are artificially aged at 200°C, the  $\theta'$  phase is directly nucleated as a dominant phase; no major GP zones dissolution peaks are found in the DSC curves (figure 5.32).

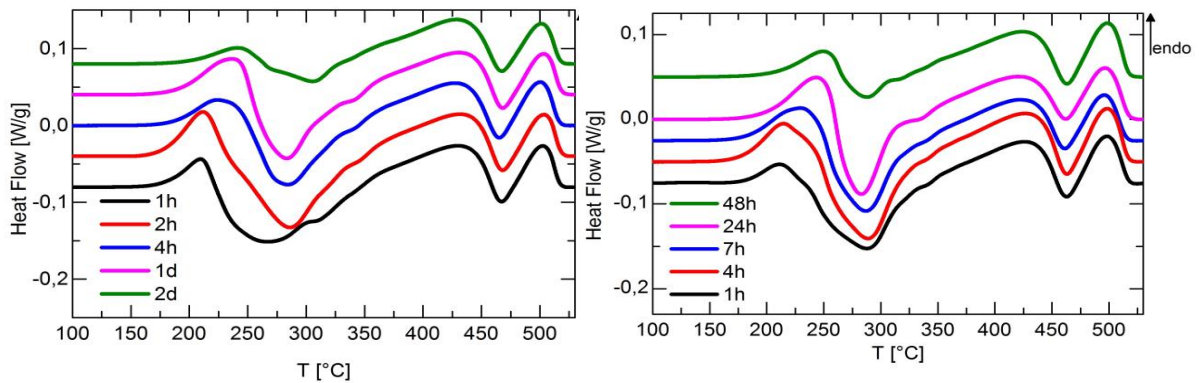


Figure 5.31: DSC curves of aged Al-1.7at.%Cu-0.01at.%Sn (Left) and Al-1.7at.%Cu-0.01at.%In (Right) at 150 °C. After 1h, GP-I and GP-II zone dissolution are observed between 200 and 270 °C. The formation of  $\theta'$  precipitates is shifted to be at about 270 °C, which is 100 degree more than that of Al-Cu binary alloy.



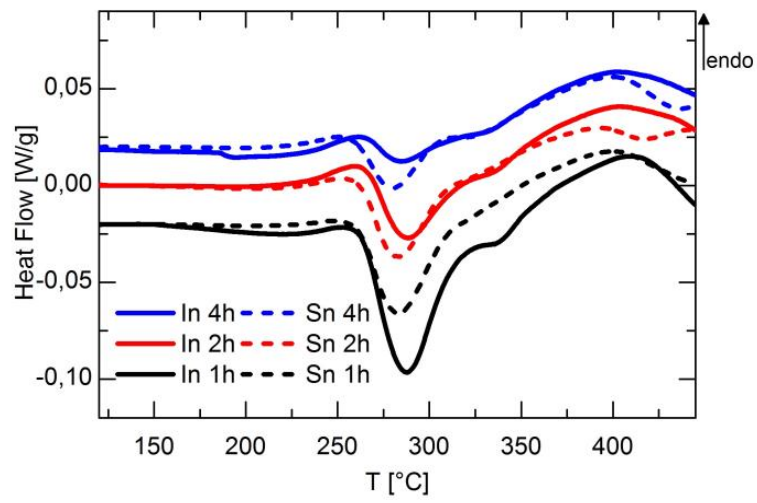


Figure 5.32: DSC curves for aged Al-1.7at.%Cu with 100 ppm Sn and In at 200 °C.  $\theta'$  phase is directly forming as the dominating phase.



## Chapter 6 : Summary

This work has presented an experimental investigation of the interaction between the quenched-in vacancies and the solute atoms in the highly diluted binary Al alloys (Al-Cu, Al-In, Al-Sn, Al-Sb, Al-Pb, and Al-Bi) and their influence on the precipitation formation in Al-1.7 at.% Cu based alloy by using positron annihilation spectroscopy.

### Hardness measurement

- There is no significant difference in hardness between Al-Cu-Pb and pure Al-Cu alloy at RT and even at elevated temperatures (figure 5.2).
- At RT, Al-Cu alloy is harder than Al-Cu-In and Al-Cu-Sn due to the formation of GP-I zone. However, Al-Cu-In and Al-Cu-Sn showed a very rapid hardening response at elevated temperatures with higher values of 130 Hv after different ageing times: 48 h for In and 4 h for Sn.

### Positron measurements

#### Pure Al

- Quenching the sample at 620 °C to ice water (0 °C) results in a slightly lower amount of vacancies, which are agglomerating very fast together (< 15 % of positrons are trapped by vacancy cluster ). Single vacancies become mobile at RT, they diffuse quickly to sinks, and finally cannot be detected by positrons at about 150 °C ageing (almost 100% of positron annihilate freely in the bulk), see figure (5.5).
- In order to avoid the clustering of the quenched-in vacancies, pure Al is quenched to a very low temperature (cooled alcohol, -110 °C).
- Quenching the sample to lower temperatures results in higher concentration of quenched-in vacancies. Positrons could detect single vacancies and no clustering is observed (80 % of positrons are trapped by single vacancies), see figure (5.9).
- Alloying elements can be also added to pure Al to prevent the vacancy clustering.

#### Al- Cu, Pb, Bi and Sb with 250 ppm trace elements

- **Al-Cu** showed the same behavior as pure Al; the concentration of quenched-in vacancies generated by quenching to ice water is quite low (see figure 5.6). Also the alloy behaves typically as the aluminum reference even when quenched to lower temperatures (see figure 5.9); indicating that almost there is no binding between Cu

atoms and the vacancies. This agrees well with the theoretical calculation of the binding energy, which predicted a value of only 20 meV.

- In **Al-Sb** alloy, a small amount of vacancies bind the solute atoms immediately after quenching (60 % of positrons are trapped by V-Sb complex, figure 5.6). However, weak interaction between the vacancies and the antimony atoms are noticed; the vacancies release very fast from antimony atoms (contrary to the calculations, Sb-vacancy binding energy  $\sim 0.3\text{eV}$ ). Most of positrons annihilate in the bulk after annealing temperature of about 50 °C. This may be attributed either to the low solubility of Sb in Al ( $< 0.01\%$ ), thus only low vacancy concentration binds the antimony atoms, or there are insufficiency in the solute-vacancy binding calculation. Quenching the sample to cooled ethanol (-110 °C) results in a considerable amount of vacancies bind the solute atoms (figure 5.10). According to PALS measurement, one solute atom binds mostly two vacancies instantly after quenching. The vacancies release from antimony atoms starts at room temperature.
- In **Al-Pb** and **Al-Bi** alloys, no interaction between solute atoms and vacancies is observed for the alloys quenched to ice water, figure 5.6 (contrary to the calculations, binding energy is about 0.4eV). While quenching the alloys to the cooled alcohol results in a quite larger amount of vacancies bind the solute atoms, two vacancies bind a solute atom immediately after quenching, figure 5.10. The vacancies release starts at room temperature. This is also can be ascribed to the extremely low solubility of Pb and Bi in Al (below 50 ppm) or the deficiency in the ab-initio calculations of the solute –vacancy binding energy.

#### **Al- In, Al-Sn with 250 ppm trace elements**

- The influence of In and Sn on the diffusion of vacancies in high purity aluminum after quenching is completely different. Quenched-in vacancies are bound to the solute atoms at room temperature forming divacancy-solute complexes immediately after quenching, figures (5.11 and 5.19).
- Vacancies still bind the solute atoms even with annealing the alloys up to 127 °C, but one vacancy has been detached from the solute during the annealing.
- The release of vacancies from solute atoms (and thus vacancy clustering) starts at 150 °C.

### **Al-1.7 at.% Cu**

Typical precipitations sequence during ageing the alloy (GP zones -  $\theta'$  phase -  $\theta$  phase) is detected by PAS and in a good agreement with the ab-initio calculation, see figures (5.21-5.25).

### **Al-1.7 at.% Cu with 100 ppm trace elements**

- Neither Pb nor Sb atoms affect the precipitations sequence in pure Al-Cu alloy (figures 5.26-5.28). The low solubility and/or weaker vacancy-solute binding are the reasons as it is shown in the binary alloys.
- The two alloys Al-cu-In and Al-Cu-Sn show nearly the same behavior as the binary alloys Al-In and Al-Sn up to 250 °C ageing temperatures; the precipitations sequence in pure Al-Cu alloy is changed, figure 5.29.
- In and Sn atoms bind the vacancies, and thus preventing (not totally) most of Cu atoms to diffuse at RT and up to 150 °C, which in turn suppress the formation of GP zones. Artificial ageing of Al-Cu-Sn alloy shows a slightly faster ageing response compared to Al-Cu-In due to the slightly stronger binding of vacancies to In atoms compared to Sn, figure 5.29.
- At elevated temperatures about 200 °C, most of vacancies have enough energy to leave the solute atoms, and hence support Cu atoms diffusion. At about 250 °C, not only the highly mobile Cu atoms, but also the trace elements participating in the nucleation of  $\theta'$  phase, which act as a new trap of positrons.
- The formation of  $\theta'$  precipitates is shifted to be at 250 °C, which is 100 °C higher than that of Al-Cu binary alloy, figure (5.29).
- When the samples are artificially aged at 200 °C,  $\theta'$  phase is directly nucleating as the dominating phase (figure 5.32).

To conclude, the solubility of the trace elements and the vacancy-solute binding energies are two main factors that affect the precipitation sequence during natural or artificial ageing. With vacancy-solute binding energy of about 0.2-0.3 eV, the formation of GP zones at RT can be suppressed. Also with this strong binding, vacancies will become free only at elevated temperatures, which promote the formation of  $\theta'$  phase, and thus strengthening the material.

## References

- [1] Charlton, Michael, and John W. Humberston, *Positron physics*, vol. 11, Cambridge University Press, 2001.
- [2] P. Dirac, "The quantum theory of the electron," *Proceedings of the Royal Society of London. Series A, Containing Papers of a Mathematical and Physical Character*, vol. 117, no. 778, pp. 610-624, 1928.
- [3] P. Dirac, "On the annihilation of electrons and protons," *Mathematical Proceedings of the Cambridge Philosophical Society*, vol. 26, no. 3, 1930.
- [4] P. Dirac, "Quantised singularities in the electromagnetic field," *Proceedings of the Royal Society of London. Series A, Containing Papers of a Mathematical and Physical Character*, vol. 133, no. 821, pp. 60-72, 1931.
- [5] C. Anderson, "The positive electron," *Physical Review*, vol. 43, no. 6, p. 491, 1933.
- [6] G. S. Kanda, "Positron Annihilation Lifetime Spectroscopy," Diss. Dundee University, Dundee, 2015.
- [7] Van Dyck Jr, Robert S., Paul B. Schwinberg, and Hans G. Dehmelt, "New high-precision comparison of electron and positron  $g$  factors," *Physical Review Letters* 59.1, vol. 59, no. 1, p. 26, 1987.
- [8] [Glossary.ametsoc.org/wiki/Gyro-frequency](http://Glossary.ametsoc.org/wiki/Gyro-frequency), 2012.
- [9] Hughes, R. J., and B. I. Deutch, "Electric charges of positrons and antiprotons," *Physical review letters*, vol. 69, no. 4, p. 578, 1992.
- [10] Müller, Berndt, and Markus H. Thoma, "Vacuum polarization and the electric charge of the positron," *Physical review letters*, vol. 69, no. 24, p. 3432, 1992.
- [11] Sulejmanpasic, Tin, and Yuya Tanizaki, "C– P– T anomaly matching in bosonic quantum field theory and spin chains.," *Physical Review B*, vol. 97, no. 14, p. 144201, 2018.
- [12] Saarinen, Kimmo, Pekka Hautojärvi, and Catherine Corbel, "Positron annihilation spectroscopy of defects in semiconductors.," *Semiconductors and Semimetals*, vol. 51, pp. 209-285, 1998.
- [13] Edwardson, Charlene Joanne, "Positron Studies of Defects in Thin Films and Semiconductors," Diss.University of Bath, 2013.
- [14] [Http://cph-theory.persianganig.com/english.htm](http://cph-theory.persianganig.com/english.htm), 2004.

- [15] Krause-Rehberg, Reinhard, and Hartmut S. Leipner, Positron annihilation in semiconductors: defect studies, vol. 127, Halle (Saale): Springer Science & Business Media, 1999.
- [16] Schödlbauer, D., et al., "A pulsing system for low energy positrons in Physics," *Nuclear Instruments and Methods in Physics Research Section B: Beam Interactions with Materials and Atom*, vol. 34, no. 2, pp. 258-268, 1988.
- [17] A. Laakso, Construction of a pulsing system for low-energy positrons, Helsinki : Helsinki University of Technology, 2005.
- [18] P. Li, "Aspects of the mcmaster intense positron beam facility (MIPBF)," Diss.McMaster University, Hamilton, Ontario, Canada, 2015.
- [19] D. R. e. Lide, CRC handbook of chemistry and physics, vol. 85, CRC press, 2004.
- [20] Aad, Georges, et al., "Combined Measurement of the Higgs Boson Mass in p p Collisions at  $\sqrt{s}=7$  and 8 TeV with the ATLAS and CMS Experiments," *Physical review letters*, vol. 114, no. 19, p. 191803, 2015.
- [21] Verel, Iris, et al., "Long-lived positron emitters zirconium-89 and iodine-124 for scouting of therapeutic radioimmunoconjugates with PET," *Cancer Biotherapy and Radiopharmaceuticals*, vol. 18, no. 4, pp. 655-661, 2003.
- [22] Kettern, K., et al., "Formation of short-lived positron emitters in reactions of protons of energies up to 200 MeV with the target elements carbon, nitrogen and oxygen," *Applied radiation and isotopes*, vol. 60, no. 6, pp. 939-945, 2004.
- [23] Cottingham, W. Noel, Derek A. Greenwood, and Derek A. Greenwood, An introduction to nuclear physics, Cambridge : Cambridge university press, 2001.
- [24] Christensen, Carl Jørgen, et al., "Free-neutron beta-decay half-life," *Physical Review D*, vol. 5, no. 7, p. 1628, 1972.
- [25] <https://www.physics.uoguelph.ca/Nucweb/superallowed.html>, 2015.
- [26] [www.sciencegateway.org/isotope/sodium.html](http://www.sciencegateway.org/isotope/sodium.html), May 2002.
- [27] <http://physicsopenlab.org/2016/12/25/antimatter/>. [Accessed 2019].
- [28] Coleman, P. G., et al., "Positron backscattering from elemental solids," *Journal of Physics: Condensed Matter*, vol. 4, no. 50, p. 10311, 1992.
- [29] Makinen, J., et al., "Positron backscattering probabilities from solid surfaces at 2-30 keV," *Journal of Physics: Condensed Matter*, vol. 4, no. 36, p. 503, 1992.

- [30] J. Major, "Spin-Polarized Positron Beams in Condensed-Matter Studies," in *Positron Beams and their applications*, World Scientific, 2000, p. 259.
- [31] Puska, Martti J., and Risto M. Nieminen, "Theory of positrons in solids and on solid surfaces," *Reviews of modern Physics*, vol. 66, no. 3, p. 841, 1994.
- [32] Jensen, K. O., and A. B. Walker, "Positron thermalization and non-thermal trapping in metals," *Journal of Physics: Condensed Matter*, vol. 2, no. 49, p. 9757, 1990.
- [33] Nieminen, R. M., and J. Oliva, "Theory of positronium formation and positron emission at metal surfaces," *Physical Review B*, vol. 22, no. 5, p. 2226, 1980.
- [34] Schultz, Peter J., and Kelvin G. Lynn, "Interaction of positron beams with surfaces, thin films, and interfaces," *Reviews of Modern Physics*, vol. 60, no. 3, p. 701, 1988.
- [35] P. D. M. Haaks, "Materialforschung mit Positronen: Von der Doppler-Spektroskopie zur Vorhersage des Ermüdungsbruchs," *Helmholtz-Institut für Strahlen-und Kernphysik, Universität Bonn*, 2010.
- [36] Ivanova, A. V., and E. P. Prokop'ev, "Annihilation of Slow Positrons in Hydrides of Alkali Metals . II," *Soviet physics JETP*, vol. 21, no. 4, 1965.
- [37] A. Dalla, "Positronen-Annihilations-Spektroskopie an photovoltaischen Cu (In<sub>x</sub>, Ga<sub>1-x</sub>) Se<sub>2</sub>-Schichten," Diss.Martin-Luther-Universität Halle-Wittenberg, Halle (Saale), 2016.
- [38] M. Elsayed, "The appearance of vacancies during Cu and Zn diffusion in III-V compound semiconductors," Diss.Martin-Luther-Universität Halle-Wittenberg, Halle (Saale), 2011.
- [39] R. N. West, "Positron studies of condensed matter," *Advances in Physics*, vol. 22, no. 3, pp. 163-183, 1973.
- [40] J. Čížek, "Characterization of lattice defects in metallic materials by positron annihilation spectroscopy: A review," *Journal of Materials Science & Technology*, vol. 34, no. 4, pp. 577-598, 2018.
- [41] Saarinen, K., et al., "Shallow positron traps in GaAs," *Physical Review B*, vol. 39, no. 8, p. 5287, 1989.
- [42] Staab, T. E. M., E. Zschech, and R. Krause-Rehberg, "Positron lifetime measurements for characterization of nano-structural changes in the age hardenable AlCuMg 2024 alloy," *Journal of materials science*, vol. 35, no. 18, pp. 4667-4672, 2000.
- [43] Häkkinen, H., S. Mäkinen, and M. Manninen., "Positron states in dislocations:

- shallow and deep traps," *EPL (Europhysics Letters)*, vol. 9, no. 8, p. 809, 1989.
- [44] Manninen, Matti, and R. M. Nieminen, "Positron detrapping from defects: A thermodynamic approach," *Applied Physics A*, vol. 26, no. 2, pp. 93-100, 1981.
- [45] Chen, Y. Z., et al., "Defect Recovery in Severely Deformed Ferrite Lamellae During Annealing and Its Impact on the Softening of Cold-Drawn Pearlitic Steel Wires," *Metallurgical and Materials Transactions A*, vol. 47, no. 2, pp. 726-738, 2016.
- [46] Sato, Koichi, et al., "Behavior of vacancies near edge dislocations in Ni and  $\alpha$ -Fe: Positron annihilation experiments and rate theory calculations," *Physical Review B*, vol. 75, no. 9, p. 094109, 2007.
- [47] Smedskjaer, Lars C., Matti Manninen, and Michael J. Fluss, "An alternative interpretation of positron annihilation in dislocations," *Journal of Physics F: Metal Physics*, vol. 10, no. 10, p. 2237, 1980.
- [48] Nieminen, R. M., and J. Laakkonen., "Positron trapping rate into vacancy clusters," *Applied physics*, vol. 20, no. 2, pp. 181-184, 1979.
- [49] Čížek, J., et al., "Vacancy clusters in ultra fine grained metals prepared by severe plastic deformation," *Journal of Physics: Conference Series*, vol. 443, p. 012008, 2013.
- [50] C. Wolverton, "Solute-vacancy binding in aluminum," *Acta Materialia*, vol. 55, no. 17, pp. 5867-5872, 2007.
- [51] Hirsch, Jürgen, Birgit Skrotzki, and Günter Gottstein, eds. , *Aluminium Alloys*, John Wiley & Sons, 2008.
- [52] M J Puska, P Lanki and R M Nieminen, "Positron affinities for elemental metals," *Journal of Physics: Condensed Matter*, vol. 1, no. 35, p. 6081, 1989.
- [53] Panda, B. K., and G. Brauer., "Positron affinities and deformation potentials in cubic semiconductors," *Acta Physica Polonica-Series A General Physics*, vol. 95, no. 4, pp. 641-646, 1999.
- [54] Lang, N. D., and W. Kohn, "Theory of metal surfaces: work function," *Physical Review B*, vol. 3, no. 4, p. 1215, 1971.
- [55] Jibaly, Mohammed, et al., "Measurement of the positron work functions of polycrystalline Fe, Mo, Ni, Pt, Ti, and V," *Physical Review B*, vol. 44, no. 22, p. 12166, 1991.
- [56] Zhang, S., et al., "Positron annihilation study on deformation-induced Au

- precipitation in Fe–Au and Fe–Au–B–N alloys," *Journal of materials science*, vol. 49, no. 6, pp. 2509-2518, 2014.
- [57] Vlach, Martin, et al., "Early stages of precipitation process in Al-(Mn-) Sc-Zr alloy characterized by positron annihilation," *Metallurgical and Materials Transactions A*, vol. 46, no. 4, pp. 1556-1564, 2015.
- [58] A. G. Elsherif, "Study of the pore systems of metal-organic frameworks, mesoporous silica, and low-k dielectric layers by means of positron annihilation spectroscopy," Diss. Martin-Luther University Halle-Wittenberg, Halle (Saale), 2018.
- [59] A. I. Kul'ment'ev, "Interpretation of positron lifetime spectra via least squares prony method," *Вопросы атомной науки и техники*, 2013.
- [60] Asoka-Kumar, P., et al., "Increased Elemental Specificity of Positron Annihilation Spectra," *Physical Review Letters*, vol. 77, no. 10, p. 2097, 1996.
- [61] B. Ballot, "Akustische versuche auf der niederländischen eisenbahn, nebst gelegentlichen bemerkungen zur theorie des hrn. prof. doppler.," *Annalen der Physik*, vol. 142, no. 11, pp. 321-351, 1845.
- [62] Grafutin, Viktor I., and Evgenii P. Prokop'ev, "Positron annihilation spectroscopy in materials structure studies.," *Physics-Uspekhi*, vol. 45, no. 1, p. 59, 2002.
- [63] Hautojärvi, P., and A. Vehanen, "Introduction to positron annihilation," in *Positrons in solids.*, Springer, Berlin, Heidelberg, 1979, pp. 1-23.
- [64] J. L. Campbell, "Annihilation gamma-ray lineshape parameters," *Applied physics*, vol. 13, no. 4, pp. 365-369, 1977.
- [65] Gebauer, J., et al., "Microscopic identification of native donor Ga-vacancy complexes in Te-doped GaAs," *Physical review B*, vol. 60, no. 3, p. 1464, 1999.
- [66] Mantl, S., and W. Triftshäuser, "Defect annealing studies on metals by positron annihilation and electrical resistivity measurements," *Physical Review B*, vol. 17, no. 4, p. 1645, 1978.
- [67] Liskay, L., et al., "Positron trapping at divacancies in thin polycrystalline CdTe films deposited on glass," *Applied physics letters*, vol. 64, no. 11, pp. 1380-1382, 1994.
- [68] Saarinen, K., et al., "Identification of the Native Vacancy Defects in Both Sublattices of ZnS<sub>x</sub>Se<sub>1-x</sub> by Positron Annihilation," *Physical review letters*, vol. 77, no. 16, p. 3407, 1996.
- [69] Lynn, K. G., et al. , "Positron-Annihilation Momentum Profiles in Aluminum: Core



- Contribution and the Independent-Particle Mode," *Physical Review Letters* , vol. 38, no. 5, p. 241, 1977.
- [70] Hübner, C. G., H. S. Leipner, and Reinhard Krause-Rehberg, "Deformation Induced Defects in GaAs-The Role of Dislocations," *Materials Science Forum*, vol. 255, pp. 497-499, 1997.
- [71] Van Veen, A., H. Schut, and P. E. Mijnders, "Depth-profiling of subsurface regions, interfaces and thin films," in *Positron Beams and Their Applications*, World Scientific, 2000, pp. 191-225.
- [72] Alatalo, M., et al., "Identification of vacancy defects in compound semiconductors by core-electron annihilation," *Application to InP. Physical Review B*, vol. 51, no. 7, p. 4176, 1995.
- [73] Čížek, Jakub, et al., "Annealing process in quenched Al-Sn alloys: A positron annihilation study," *Physical Review B*, vol. 7, no. 6, p. 064106, 2005.
- [74] J. Cizek , M. Vlcek, I. Prochazka, "Digital spectrometer for coincidence measurement of Doppler broadening of positron annihilation radiation," *Nuclear Instruments and Methods in Physics Research A: Accelerators, Spectrometers, Detectors and Associated Equipment* , vol. 623, no. 3, p. 982–994, 2010.
- [75] Kuang, Peng, et al., "Tunable monoenergy positron annihilation spectroscopy of polyethylene glycol thin films," *Chinese Physics B*, vol. 26, no. 5, p. 057802, 2017.
- [76] Prochazka, Ivan, et al., "Slow-positron implantation spectroscopy in nanoscience," in *Nanostructured Materials for Functional, Structural and Bio-Applications (NANO'07)*, Brno, Czech Republic, 2009.
- [77] Brandt, Werner, and Robert Paulin, "Positron implantation-profile effects in solids," *Physical review B*, vol. 15, no. 5, p. 2511, 1977.
- [78] Schrader, D. M., et al., *Positron Annihilation* ed PC Jean et al, Singapore: World scientific, 1985.
- [79] A. Saoucha, "Positron transmission into Kapton: The effective mass absorption coefficient of relevance to positron lifetime experiments," *Journal of applied physics*, vol. 85, no. 3, pp. 1802-1810, 1984.
- [80] Valkealahti, S., and R. M. Nieminen, "Monte Carlo calculations of keV electron and positron slowing down in solids. II," *Applied Physics A*, vol. 35, no. 1, pp. 51-59, 1984.

- [81] A. F. Makhov, "The Penetration of Electrons into Solids. 2. The Distribution of Electrons in Depth," *soviet physics-solid state*, vol. 2, no. 9, pp. 1942-1944, 1961.
- [82] Vehanen, A., et al., "Profiling multilayer structures with monoenergetic positrons," *Physical Review B*, vol. 35, no. 10, p. 4606, 1987.
- [83] C. Hugenschmidt, "Positrons in surface physics," *Surface Science Reports*, vol. 71, no. 4, pp. 547-594, 2016.
- [84] M. Jungmann, "Konzeption und Aufbau des Positronenstrahlsystems MePS, PAS-Messungen an porösen low-k-Schichten," Diss. Universitäts-und Landesbibliothek Sachsen-Anhalt, Halle (Saale), 2015.
- [85] P. e. Coleman, Positron beams and their applications, World Scientific, 2000.
- [86] Liskay, L., et al. , "Compact, Magnetically Guided Slow Positron Beam for Defect Studies," *Materials Science Forum*, vol. 105, pp. 1931-1934, 1992.
- [87] K. Mostafa Mohamed Mohamed Mohamed, " A study of iron based alloys by positron annihilation spectroscopy," Diss. Ghent University, Ghent , 2009.
- [88] Howell, Richard H., et al. , "Positron beam lifetime spectroscopy of atomic scale defect distributions in bulk and microscopic volumes," *Applied surface science*, vol. 116, pp. 7-12, 1997.
- [89] C. Zamponi, "Positronenspektroskopie an plastischen Zonen in Al-Legierungen und GaAs-Wafern," Diss.Universität Bonn, Bonn, 2002.
- [90] Hull, Derek, and David J. Bacon, Introduction to dislocations, Butterworth-Heinemann, 2001.
- [91] [https://en.wikipedia.org/wiki/Crystallographic\\_defect](https://en.wikipedia.org/wiki/Crystallographic_defect), 2019.
- [92] P. Haasen, Physikalische metallkunde, Springer, 2013.
- [93] [https://www.tf.uni-kiel.de/matwis/amat/def\\_en/kap\\_2/backbone/r2\\_1\\_1.html](https://www.tf.uni-kiel.de/matwis/amat/def_en/kap_2/backbone/r2_1_1.html)
- [94] [www.tf.uni-kiel.de/matwis/amat/def\\_en/kap\\_2/basics/b2\\_1\\_3.html](http://www.tf.uni-kiel.de/matwis/amat/def_en/kap_2/basics/b2_1_3.html)
- [95] [www.difference.minaprem.com/materials-science/difference-between-schottky-defect-and-frenkel-defect/](http://www.difference.minaprem.com/materials-science/difference-between-schottky-defect-and-frenkel-defect/), 2019.
- [96] [https://www.doitpoms.ac.uk/tlplib/dislocations/dislocation\\_glide.php](https://www.doitpoms.ac.uk/tlplib/dislocations/dislocation_glide.php), 2004-2019
- [97] J. Frenkel, "On the theory of elasticity and yield stress in crystalline bodies," *Z.Phys*, vol. 37, p. 572, 1926.
- [98] Smallman, Raymond Edward, and Ray J. Bishop, Metals and materials: science,

- processes, applications, Elsevier, 2013.
- [99] [https://www.doitpoms.ac.uk/tlplib/dislocations/slip\\_via\\_dislocation.php](https://www.doitpoms.ac.uk/tlplib/dislocations/slip_via_dislocation.php), 2004-2019
- [100] Cao, Q. P., et al., "Tensile elastic behavior of a Zr–Cu–Ag–Al bulk metallic glass," *Journal of Materials Science & Technology*, vol. 30, no. 6, pp. 595-598, 2014.
- [101] M. Polanyi, "On a Type of Dislocation that Makes Metals Plastic," *Zeitschrift für Physik*, vol. 89, pp. 660-666, 1934.
- [102] G. I. Taylor, "The mechanism of plastic deformation of crystals. Part I. Theoretical.," *Proceedings of the Royal Society of London. Series A*, vol. 145, no. 855, pp. 362-387, 1934.
- [103] E. Orowan, " Zur kristallplastizität. i," *Zeitschrift für Physik*, vol. 89, no. 9-10, pp. 605-613., 1934 .
- [104] [www.nde-ed.org/EducationResources/CommunityCollege/Materials/Structure/linear\\_defects.htm](http://www.nde-ed.org/EducationResources/CommunityCollege/Materials/Structure/linear_defects.htm), 2001-2014
- [105] <https://nptel.ac.in/courses/113102080/>, 2003-2017
- [106] [Http://site.iugaza.edu.ps/jelzebda/files/2010/02/Chapter07Call.pdf](http://site.iugaza.edu.ps/jelzebda/files/2010/02/Chapter07Call.pdf)
- [107] Hayden, H. W., William G. Moffatt, and John Wulff., "The structure and properties of materials. V. 3. Mechanical behavior," *John wiley and sons, New york*, vol. 3, p. 248, 1965.
- [108] A. G. Guy, "Essentials of Materials Science," *McGraw-Hill book company, New York*, p. 153, 1976.
- [109] B. D. Wirth, "How does radiation damage materials?," *Science* 318.5852, vol. 318, no. 5852, pp. 923-924, 2007.
- [110] L. E. Murr, *Handbook of materials structures, properties, processing and performance*, Switzerland: Springer, 2015.
- [111] [https://www.nde-ed.org/EducationResources/CommunityCollege/Materials/Structure/bulk\\_defects.htm](https://www.nde-ed.org/EducationResources/CommunityCollege/Materials/Structure/bulk_defects.htm), 2001-2014.
- [112] S. V.Kailas, "Imperfections in Solids," Dept. of Mechanical Engineering, Indian Institute of Science, Bangalore.
- [113] Khanna, Rita, and Veena Sahajwalla., "Atomistic Simulations of Properties and Phenomena at High Temperatures," *Treatise on Process Metallurgy: Process Fundamentals*, pp. 287-393, 2014.

- [114] Borg, Richard J., and George Julian Dienes, *An introduction to solid state diffusion*, Elsevier, 2012.
- [115] [Www.uio.no/studier/emner/matnat/kjemi/KJM5120/v05/undervisningsmateriale/KJM5120-Ch5-Diffusion.pdf](http://www.uio.no/studier/emner/matnat/kjemi/KJM5120/v05/undervisningsmateriale/KJM5120-Ch5-Diffusion.pdf), 2005
- [116] A. Fick, "V. On liquid diffusion," *The London, Edinburgh, and Dublin Philosophical Magazine and Journal of Science*, vol. 10, no. 63, pp. 30-39, 1855.
- [117] Heitjans, Paul, and Jörg Kärger, eds., *Diffusion in condensed matter: methods, materials, models*, Springer Science & Business Media, 2006.
- [118] [Link.springer.com/content/pdf/bbm%3A978-1-4020-7860-6%2F1.pdf](http://link.springer.com/content/pdf/bbm%3A978-1-4020-7860-6%2F1.pdf)
- [119] <https://www.imetllc.com/phase-transformations-in-alloys/>.
- [120] L. Avala, *Concepts in physical metallurgy*, Morgan & Claypool Publishers, 2017.
- [121] [Www.southampton.ac.uk/~pasr1/build.htm](http://www.southampton.ac.uk/~pasr1/build.htm).
- [122] <https://www.sciencedirect.com/topics/engineering/melting-temperature>
- [123] J. W. Gibbs, "Scientific Papers: Thermodynamics," *Dover Publications*, vol. 1, 1961.
- [124] F. C. e. Campbell, *Elements of metallurgy and engineering alloys*, ASM International, 2008.
- [125] M. Feinberg, "On Gibbs' phase rule," *Archive for Rational Mechanics and Analysis*, vol. 70, no. 3, pp. 219-234, 1979.
- [126] [Www.tf.uni-kiel.de/matwis/amat/iss/kap\\_6/illustr/s6\\_1\\_1.html](http://www.tf.uni-kiel.de/matwis/amat/iss/kap_6/illustr/s6_1_1.html)
- [127] [Www.southampton.ac.uk/~pasr1/tielines.htm](http://www.southampton.ac.uk/~pasr1/tielines.htm)
- [128] Witt, Jessica A., Daniel R. Mumm, and Ali Mohraz, "Bijel reinforcement by droplet bridging: a route to bicontinuous materials with large domains," *Soft Matter*, vol. 9, no. 29, pp. 6773-6780, 2013.
- [129] Cubillas, Pablo, and Michael W. Anderson, "Synthesis mechanism: crystal growth and nucleation," *Zeolites and Catalysis: Synthesis, Reactions and Applications*, pp. 1-55, 2010.
- [130] Laaksonen, Ari, Robert McGraw, and Hanna Vehkamäki, "Liquid-drop formalism and free-energy surfaces in binary homogeneous nucleation theory," *The Journal of chemical physics*, vol. 111, no. 5, pp. 2019-2027, 1999.
- [131] F. Abraham, *Homogeneous nucleation theory: the pretransition theory of vapor condensation*, vol. 1, Elsevier, 2012.

- [132] G. Gottstein, *Physikalische Grundlagen der Materialkunde.*, Springer, 2007.
- [133] Lazaridis, Mihalis, Markku Kulmala, and Boris Z. Gorbunov, "Binary heterogeneous nucleation at a non-uniform surface," *Journal of aerosol science*, vol. 23, no. 5, pp. 457-466, 1992.
- [134] Yuan, Yuehua, and T. Randall Lee, "Contact angle and wetting properties.," *Surface science techniques*, pp. 3-34, 2013.
- [135] [www.tf.uni-kiel.de/matwis/amat/semitech\\_en/kap\\_3/advanced/t3\\_3\\_2.html](http://www.tf.uni-kiel.de/matwis/amat/semitech_en/kap_3/advanced/t3_3_2.html)
- [136] <http://2011.igem.org/Team:KULeuven/Thermodynamics>
- [137] D. tauffer, "Kinetic theory of two-component ("hetero-molecular") nucleation and condensation," *Journal of Aerosol Science*, vol. 7, no. 4, pp. 319-333, 1976.
- [138] A. Hienola, "On the homogeneous and heterogeneous nucleation of some organic compounds," Diss. Helsinki university, Helsinki, 2008.
- [139] Porter, David A., Kenneth E. Easterling, and Mohamed Sherif, *Phase Transformations in Metals and Alloys*, (Revised Reprint), vol. 44, CRC press, 2009, p. 314.
- [140] [en.wikipedia.org/wiki/Spinodal\\_decomposition](https://en.wikipedia.org/wiki/Spinodal_decomposition), 2019
- [141] <https://www.aluminum.org/strength-aluminum>, 2019
- [142] R. Davidge, "Mechanical Behavior of Ceramics, Chapter: Elastic Behavior," *Cambridge Solid State Science Series, RAN Publishers, Marietta, OH*, vol. 45750, pp. 22-27, 1979.
- [143] Lawn, Brian, and T. Rodney Wilshaw, *Fracture of brittle solids*, Cambridge university press, 1993.
- [144] D. J. Green, *An introduction to the mechanical properties of ceramics*, Cambridge University Press, 1998.
- [145] Callister, William D., and David G. Rethwisch, *Materials science and engineering: an introduction*, vol. 7, New York: John Wiley & Sons, 2007.
- [146] D. Kuhlmann-Wilsdorf, "Theory of plastic deformation:-properties of low energy dislocation structures," *Materials Science and Engineering: A*, vol. 113, pp. 1-41, 1989.
- [147] <https://sciencing.com/info-10009615-aluminum-hardness-classification.html>, 2018
- [148] [www.totalmateria.com/page.aspx?ID=CheckArticle&site=ktn&NM=235](http://www.totalmateria.com/page.aspx?ID=CheckArticle&site=ktn&NM=235), 2010

- [149] <https://prabook.com/web/alfred.wilm/2568579>.
- [150] A. Wilm, "Physical metallurgical experiments on aluminum alloys containing magnesium," *Metallurgie*, vol. 8, p. 223, 1911.
- [151] P.D. Merica, R. G. Waltenberg, and H. Scott, "US Bureau of Standards Scientific Paper 347, 1919," *AIME Trans*, vol. 64, p. 41, 1921.
- [152] [Core.materials.ac.uk/repository/eaa/talat/1204.pdf](http://core.materials.ac.uk/repository/eaa/talat/1204.pdf), 2010
- [153] P. D. Merica, "The Age-Hardening of Metals," *Trans. Aime*, vol. 99, no. 13, p. 106, 1932.
- [154] [Nvlpubs.nist.gov/nistpubs/sp958-lide/014-015.pdf](http://nvlpubs.nist.gov/nistpubs/sp958-lide/014-015.pdf)
- [155] A. Guinier, "Structure of age-hardened aluminium-copper alloys," *Nature*, vol. 142, no. 3595, p. 569, 1938.
- [156] G. D. Preston, "Structure of age-hardened aluminium-copper alloys," *Nature*, vol. 142, no. 3595, p. 570, 1938.
- [157] Lynch, J.P., L.M. Brown, and M.H. Jacobs, "Microanalysis of age-hardening precipitates in aluminium alloys," *Acta Metallurgica*, vol. 30, no. 7, pp. 1389-1395, 1982.
- [158] [www.princeton.edu/~maelabs/mae324/10/10mae\\_41.htm](http://www.princeton.edu/~maelabs/mae324/10/10mae_41.htm), 2002
- [159] [www.engineeringenotes.com/metallurgy/age-hardening-treatment/age-hardening-treatment-of-metals-metallurgy/26376](http://www.engineeringenotes.com/metallurgy/age-hardening-treatment/age-hardening-treatment-of-metals-metallurgy/26376)
- [160] M. e. a. Takeda, "Discontinuity of GP (I) zone and  $\theta$  '-phase in an Al-Cu alloy," *Scripta Materialia*, vol. 41, no. 6, pp. 643-649, 1999.
- [161] W. Ostwald, "Über die vermeintliche Isomerie des roten und gelben Quecksilberoxyds und die Oberflächenspannung fester Körper," *Zeitschrift für physikalische Chemie*, vol. 34, no. 1, pp. 495-503, 1900.
- [162] C. Wagner, "Theorie der alterung von niederschlägen durch umlösen (Ostwald-reifung)," *Zeitschrift für Elektrochemie, Berichte der Bunsengesellschaft für physikalische Chemie*, vol. 65, no. 7-8, pp. 581-591, 1961.
- [163] I. R. Clark, "High-temperature Dislocation Precipitate Interactions in Al Alloys," *J. Mater. Res*, vol. 20, no. 7, pp. 1792-1801, 2005.
- [164] O. Wouters, Plasticity in Aluminum Alloys at Various Length Scales, University Library Groningen][Host], 2006.

- [165] A. J. Ardell, "Precipitation hardening," *Metallurgical Transactions A*, vol. 16, no. 12, pp. 2131-2165, 1985.
- [166] <https://sciencing.com/hardest-metal-known-man-5149739.html>
- [167] C. Bluhm, "Untersuchungen des Ausheilverhaltens von abgeschreckten Al-0.025at% In-Legierungen mit Hilfe der digitalen Positronen-Lebensdauerspektroskopie," Master thesis. Martin-Luther university Halle-Wittenberg, Halle(Saale), 2016.
- [168] P. Ehrhart, "Atomic defects in metals," *Landolt-Bornstein*, vol. New Series III/25, pp. 211-223, 1991.
- [169] Khellaf, Abdallah, Alfred Seeger, and Roy M. Emrick. , "Quenching studies of lattice vacancies in high-purity aluminium," *Materials transactions* , vol. 43, no. 2, pp. 186-198, 2002.
- [170] Hirsch, P. B., et al., "Dislocation loops in quenched aluminium," *Philosophical Magazine*, vol. 3, no. 32, pp. 897-908, 1958.
- [171] Liu, Meng, Benedikt Klobes, and John Banhar, "Positron lifetime study of the formation of vacancy clusters and dislocations in quenched Al, Al-Mg and Al-Si alloys," *Journal of materials science*, vol. 51, no. 16, pp. 7754-7767, 2016.
- [172] Fischer, F. D., et al., "Modeling of excess vacancy annihilation at different types of sinks," *Acta Materialia*, vol. 59, no. 9, pp. 3463-3472, 2011.
- [173] Ascoli, A., et al., "Activation energies for the production and migration of vacancies in platinum," *Journal of Physics and Chemistry of Solids*, vol. 6, no. 1, pp. 59-64, 1958.
- [174] A. Seeger, "Diffusion and Point-Defect Properties," *Defect and Diffusion Forum, Trans Tech Publications.*, vol. 95, pp. 147-170, 1993.
- [175] Kauffman, J. W., and J. S. Koehler., "The quenching-in of lattice vacancies in pure gold," *Physical Review*, vol. 88, no. 1, p. 149, 1952.
- [176] H. E. Schaefer, "Investigation of thermal equilibrium vacancies in metals by positron annihilation," *physica status solidi (a)*, vol. 102, no. 1, pp. 47-65, 1987.
- [177] Eremeev, S. V., et al., "Activation energy for diffusion of point defects at the surfaces of FCC metals," *Russian Physics Journal*, vol. 40, no. 6, pp. 584-589, 1997.
- [178] [www.phase-trans.msm.cam.ac.uk/abstracts/L1-2.pdf](http://www.phase-trans.msm.cam.ac.uk/abstracts/L1-2.pdf)
- [179] D. Altenpohl, Aluminium und aluminiumlegierungen, vol. 19, Springer, 2013.

- [180] Nissilä, J., et al., "Performance analysis of a digital positron lifetime spectrometer," *Nuclear Instruments and Methods in Physics Research Section A: Accelerators, Spectrometers, Detectors and Associated Equipment*, vol. 538, no. 1-3, pp. 778-789, 2005.
- [181] E.Hirschmann, "Optimierung der Positronen-Annihilation-Lebensdauer-Spektroskopie durch die Einführung eines digitalen Messsystems und dessen Anwendung zur Untersuchung der Frühstadien in Aluminiumlegierungen," Master thesis. Martin-Luther university Halle-Wittenberg, 2016.
- [182] J. P. Ralston, "Design and Performance Analysis of an Ultra-Fast Digital Positron Annihilation Lifetime Spectrometer at The Ohio State University," Diss. Ohio State University, Ohio State, 2013.
- [183] J. Kansy, "Microcomputer program for analysis of positron annihilation lifetime spectra," *Nuclear Instruments and Methods in Physics Research Section A: Accelerators, Spectrometers, Detectors and Associated Equipment*, vol. 374, no. 2, pp. 235-244, 1996.
- [184] J. Kansy, "LT for Windows, Version 9.0," *Silesian University, Inst of Phys Chem of Metals, Bankowa*, vol. 12, pp. 40-007, 2002.
- [185] Shukla, Abhay, Martin Peter, and Ludger Hoffmann, "Analysis of positron lifetime spectra using quantified maximum entropy and a general linear filter," *Nuclear Instruments and Methods in Physics Research Section A: Accelerators, Spectrometers, Detectors and Associated Equipment*, vol. 353, no. 1-2, pp. 310-317, 1993.
- [186] F. E., "Differential scanning calorimetry," *Methods Mol Biol.*, vol. 40, pp. 191-218, 1995.
- [187] Hersent, Emmanuel, Julian Haworth Driver, and David Piot., "Modelling differential scanning calorimetry curves of precipitation in Al–Cu–Mg," *Scripta Materialia*, vol. 62, no. 7, pp. 455-457, 2010.
- [188] Skoog, Douglas A., F. James Holler, and Stanley R. Crouch., Principles of instrumental analysis, Cengage learning, 2017.
- [189] Kodre, K. V., et al., "Differential scanning calorimetry: A review." Research and Reviews," *Journal of Pharmaceutical Analysis.*, vol. 3, no. 3, pp. 11-22, 2014.
- [190] Chen, Dun, Andrew Green, and David Dollimore, "DSC: The importance of baseline



- callibration," *Thermochimica Acta*, vol. 284, no. 2, p. 429–433, 1996.
- [191] Lotter, Frank, et al., "The Influence of Trace Elements (In, Sn) on the Hardening Process of Al–Cu Alloys," *physica status solidi (a)*, vol. 215, no. 11, p. 1800038, 2018.
- [192] <https://warwick.ac.uk/fac/sci/physics/current/postgraduate/regs/mpagswarwick/ex5/techniques/structural/tem/>, 2010
- [193] Williams, David B., and C. Barry Carter, "Imaging in the TEM," in *Transmission Electron Microscopy*, Boston, MA, Springer, 1996, pp. 349-366.
- [194] <https://sites.google.com/site/bsatpati/tem?tmpl=%2Fsystem%2Fapp%2Ftemplates%2Fprint%2F&showPrintDialog=1>.
- [195] Tang, C. Y., and Z. Yang., "Transmission electron microscopy (TEM)," in *Membrane Characterization*, Elsevier, 2017, pp. 145-159.
- [196] <https://www.healthtard.com/guide-to-electron-microscopy/>, 2019
- [197] <https://www.encyclopedia.com/people/history/historians-miscellaneous-biographies/friedrich-mohs>
- [198] <https://www.engineeringclicks.com/vickers-hardness-test/>, 2019
- [199] I. J. Polmear, "Aluminium Alloys--A Century of Age Hardening," *Materials forum*, vol. 28, 2004.
- [200] Lotter, Frank, et al., "Precipitation Behavior in High-Purity Aluminium Alloys with Trace Elements–The Role of Quenched-in Vacancies," *physica status solidi (a)*, vol. 215, no. 24, p. 1800375, 2018.
- [201] Pogatscher, S., et al. , "Diffusion on demand to control precipitation aging: application to Al-Mg-Si alloys," *Physical review letters*, vol. 112, no. 22, p. 225701, 2014.
- [202] Werinos, M., et al., "Influence of Sn-solubility on suppression of natural aging in an AA6061 aluminum alloy," *Proceedings of the Materials Science & Technology (MS&T), Pittsburgh, PA, USA*, pp. 12-16, 2014.
- [203] W. J. Plumbridge, "The interaction between indium atoms and vacancies in dilute aluminium-indium alloys," *Philosophical Magazine*, vol. 20, no. 166, pp. 707-718, 1969.
- [204] H. Hardy, "The effect of small quantities of Cd, In, Sn, Sb, Ti, Pb, or Bi on the ageing characteristics of cast and heat-treated aluminum-4-percent copper-0.15-

- percent titanium alloy," *Journal of the Institute of Metals*, vol. 78, no. 2, p. 169, 1950.
- [205] Hardy, HK, R. Chadwick, and A. Vonzeerleder, "Joint discussion on the papers by hardy, HK-The effect of small quantities of Cd, In, Sn, Sb, Ti, Pb, or Bi on the ageing characteristics of cast and heat-treated aluminum-4-percent copper-0.15-percent titanium alloy and the tensile properties," *Journal of the institute of metals*, vol. 79, no. 12, pp. 487-492, 1951.
- [206] Polmear, I. J., and H. K. Hardy. , "Some metallographic observations on aged aluminium-copper alloys," *Journal of the Institute of Metals* , vol. 81, no. 8, pp. 427-431, 1953.
- [207] Silcock, J. M., T. J. Heal, and H. K. Hardy, "Structural ageing characteristics of binary aluminium-copper alloys," *J. Inst. Metals*, vol. 82, 1954.
- [208] J. M. Silcock, "Intermediate precipitates in aged binary alloys of aluminium with cadmium, indium or tin," *J. Inst. Metal* , vol. 84, pp. 19-22, 1955.
- [209] Silcock, J. M., and T. J. Heal. , "The  $\theta$ 'structure in aluminium-copper alloys," *Acta Crystallographica*, vol. 9, no. 8, pp. 680-680, 1956.
- [210] J. M. Silcock, "The effect of quenching on the formation of gp zones and  $\theta'$  in al cu-alloys," *Philosophical Magazine*, vol. 4, no. 46, pp. 1187-1194, 1959.
- [211] Silcock, J. M., and H. M. Flower, "Comments on a comparison of early and recent work on the effect of trace additions of Cd, In, or Sn on nucleation and growth of  $\theta'$  in Al-Cu alloys," *Scripta Materialia*, vol. 46, no. 5, pp. 389-394, 2002.
- [212] L. F. Mondolfo, *Aluminum alloys: structure and properties*, Elsevier, 2013.
- [213] Balluffi, R. W., and P. S. Ho., "Diffusion, Ohio: Am," *Soc. Metals*, p. 83, 1973.
- [214] Hauenstein, Oliver, et al., "Biobased Polycarbonate as a Gas Separation Membrane and "Breathing Glass" for Energy Saving Applications," *Advanced Materials Technologies*, vol. 2, no. 5, p. 1700026, 2017.
- [215] Luna, Carla Romina, et al., "Vacancy clustering in pure metals: some first principle calculations of positron lifetimes and momentum distributions," *In Journal of Physics: Conference Series IOP Publishing*, vol. 443, no. 1, p. 012019, 2013.
- [216] Puska, M. J., and R. M. Nieminen. , "Defect spectroscopy with positrons: a general calculational method," *Journal of Physics F: Metal Physics*, vol. 13, no. 2 , p. 333, 1983.
- [217] A. Seeger, "Investigation of point defects in equilibrium concentrations with

- particular reference to positron annihilation techniques," *Journal of Physics F: Metal Physics*, vol. 3, no. 2, p. 248, 1973.
- [218] Elsayed, M., et al., "Identification of defect properties by positron annihilation in Te-doped GaAs after Cu in-diffusion," *Physical Review B*, vol. 84, no. 19, p. 195208, 2011.
- [219] Staab, T. E. M., R. Krause-Rehberg, and B. Kieback, "Review Positron annihilation in fine-grained materials and fine powders—an application to the sintering of metal powders," *Journal of materials science*, vol. 34, no. 16, pp. 3833-3851, 1999.
- [220] Gavini, Vikram, Kaushik Bhattacharya, and Michael Ortiz., "Vacancy clustering and prismatic dislocation loop formation in aluminum," *Physical Review B*, vol. 76, no. 18, p. 180101, 2007.
- [221] Panseri, C., and T. Federighi, "Isochronal annealing of vacancies in aluminium," *Philosophical Magazine*, vol. 3, no. 35 , pp. 1223-1240, 1958.
- [222] J. R. Davis, Aluminum and aluminum alloys, ASM international, 1993.
- [223] Francis, M. F., and W. A. Curtin, "Microalloying for the controllable delay of precipitate formation in metal alloys," *Acta Materialia* , vol. 106 , pp. 117-128, 2016.
- [224] [https://chem.libretexts.org/Ancillary\\_Materials/Demos%2C\\_Techniques%2C\\_and\\_Experiments/General\\_Lab\\_Techniques/Cooling\\_baths](https://chem.libretexts.org/Ancillary_Materials/Demos%2C_Techniques%2C_and_Experiments/General_Lab_Techniques/Cooling_baths)
- [225] R. E. Rondeau, "Slush Baths," *Journal of Chemical and Engineering Data*, vol. 11, no. 1, pp. 124-124, 1966.
- [226] Linderoth, Søren, H. Rajainmäki, and Ro M. Nieminen, "Defect recovery in aluminum irradiated with protons at 20 K," *Physical Review B* , vol. 35, no. 11, p. 5524, 1987.
- [227] Melikhova, O., et al., "Vacancy–solute complexes in aluminum.," *Applied surface science*, vol. 252, no. 9, pp. 3285-3289, 2006.
- [228] Dlubek, G., et al., "A positron annihilation study of vacancies and their clusters in diluted aluminium alloys quenched or neutron-irradiated," *Kristall und Technik*, vol. 15, no. 12, pp. 1409-1413, 1980.
- [229] J. L. Murray, "The Al-In (aluminum-indium) system," *Bulletin of Alloy Phase Diagrams* , vol. 4, no. 3, pp. 271-278, 1983.
- [230] Kato, M., et al., "Mössbauer spectrum of <sup>57</sup>Fe and <sup>119</sup>Sn associated with lattice defects in aluminium.," *Le Journal de Physique Colloques*, vol. 35, no. C6, p. 309,

1974.

- [231] Ishida, Y., et al., "Mössbauer studies of solute atom associated with lattice defects in metals," *Le Journal de Physique Colloques*, vol. 40, no. C2, pp. C2-571, 1979.
- [232] Kiritani, M., Ji Takamura, and M. Doyama. , "Point defects and defect interactions in metals," *Yamada Science Foundation, Tokyo University* , p. 59, 1982.
- [233] Vértes, A., et al., "A Mössbauer and positron annihilation study of <sup>119</sup>Sn in an Al matrix," *Scripta Metallurgica*, vol. 16, no. 11, pp. 1229-1233, 1982.
- [234] Szeles, Cs, et al., "Positron Lifetime and Mössbauer Spectroscopy Study of Vacancy–Tin Interaction in Dilute Al- Sn Alloys," *physica status solidi (a)*, vol. 103, no. 2, pp. 397-401, 1987.
- [235] G. Dlubek, "Positron studies of decomposition phenomena in Al alloys," *Materials Science Forum, Trans Tech Publications*, vol. 13, 1987.
- [236] Gläser, U. H., G. Dlubek, and R. Krause., "Positron Trapping by the Platelet Precipitations of AlCu," *Materials Science Forum. . Trans Tech Publications*, vol. 105, pp. 1025-1028, 1992.
- [237] Gauster, W. B., and W. R. Wampler. , "A study of precipitate formation in aluminium-copper alloys by positron annihilation and transmission electron microscopy," *Philosophical Magazine A*, vol. 41, no. 2, pp. 145-156, 1980.
- [238] Staab, Torsten, et al., "Stability of Cu-precipitates in Al-Cu alloys," *Applied Sciences*, vol. 8, no. 6, p. 1003, 2018.
- [239] Kohlbach, Iris, Björn Korff, and Torsten EM Staab, "(Meta-) stable phases and pre-Guinier–Preston zones in AlCu alloys constructed from ab initio relaxed atomic positions–Comparison to experimental methods," *physica status solidi (b)*, vol. 247, no. 9, pp. 2168-2178, 2010.
- [240] Staab, Torsten EM, et al., "Atomic structure of pre-Guinier-Preston and Guinier-Preston-Bagaryatsky zones in Al-alloys.," *Journal of Physics: Conference Series*, vol. 265, no. 1, p. 012018, 2011.